The Electron Ion Collider

A high luminosity probe of the partonic substructure of nucleons and nuclei

A white paper summarizing the scientific opportunities and the preliminary detector and accelerator design options

February 2002

DISCLAIMER

This report was prepared as an account of work sponsored by an agency of the United States Government. Neither the United States Government nor any agency thereof, nor any employees, nor any of their contractors, subcontractors or their employees, makes any warranty, express or implied, or assumes any legal liability or responsibility for the accuracy, completeness, or any third party's use or the results of such use of any information, apparatus, product, or process disclosed, or represents that its use would not infringe privately owned rights. Reference herein to any specific commercial product, process, or service by trade name, trademark, manufacturer, or otherwise, does not necessarily constitute or imply its endorsement, recommendation, or favoring by the United States Government or any agency thereof or its contractors or subcontractors. The views and opinions of authors expressed herein do not necessarily state or reflect those of the United States Government or any agency thereof.

Available electronically at
http://www.doe.gov/bridge

Available to U.S. Department of Energy and its contractors in paper from-
U.S. Department of Energy Office of Scientific and Technical Information
P.O. Box 62 Oak Ridge, TN 37831
(423) 576-8401

Available to the public from-
U.S. Department of Commerce National Technical Information Service
5285 Port Royal Road Springfield, VA 22131
(703) 487-4650

PRINTED ON RECYCLED PAPER

BNL-68933

The Electron Ion Collider

A high luminosity probe of the partonic substructure of nucleons and nuclei

A white paper summarizing the scientific opportunities and the preliminary detector and accelerator design options

"*…History of science has shown that even during that phase of her progress in which she devotes herself to improving the accuracy of the numerical measurements of quantities long familiar, she is preparing the materials for the subjection of new regions, which would have remained unknown if she had been contented with the rough methods of her early pioneers…"*

-James Clark Maxwell
On the occasion of the founding of Cavendish Laboratory

Electron Ion Collider Contributing Authors

Argonne National Laboratory
R. Holt, P. Reimer

Brookhaven National Laboratory
I. Ben Zvi, J. Kewisch, T. Ludlam, L. McLerran, J. Murphy, S. Peggs, P. Paul, S. Ozaki, T. Roser, B. Surrow, R. Venugopalan*

Budker Institute of Nuclear Physics, Russia
I.A. Koop, M.S. Korostelev, I.N. Nesterenko, A.V. Otboev, V.V. Parkhomchuk, E.A. Perevedentsev, V.B. Reva, V.G. Shamovsky, D.N. Shatilov, P. Yu. Shatunov, Yu. M. Shatunov, A.N. Skrinsky

CERN, Switzerland
A. De Roeck

University of Colorado at Boulder
E.R. Kinney, U. Stoesslein

Fermi National Laboratory
V.A. Lebedev, S. Nagaitsev

University of Illinois at Urbana-Campaign
N. Makins

Indiana University Cyclotron Facility and Indiana Univserity
J. Cameron, T. Londergan, P. Schwandt

Thomas Jefferson Laboratory
Y. Derbenev, G.A. Drafft, R. Ent, L. Merminga, C. Sinclair

Lawrence Berkeley National Laboratory
X.N. Wang

Los Alamos National Laboratory
G. Garvey

Massachusetts Institute of Technology
A. Bruell, D. Hasell, R. Milner*, K. Takase, C. Tschalaer, F. Wang

Institute of Nuclear Physics, Poland
J. Chwastowski

University of Paris VI, France
E. Barrelet, M.W. Krasny

Pennsylvania State University
M. Strikman

University of Regensburg, Germany
A.Freund, A. Schaefer, M. Stratmann

RIKEN-BNL Research Center
A. Deshpande*, M.G. Perdekamp, N. Saito, W. Vogelsang

Saclay, France
G. Rädel

TRIUMF, Canada
A. Miller

Yale University
V.W. Hughes

***Contact people for the project. See next page for contact information.**

For further information contact:

Abhay Deshpande
RIKEN – BNL Research Center
Brookhaven National Laboratory
Building 510 C
Upton, New York 11973
631-344-8783
abhay@bnl.gov

Richard Milner
Massachusetts Institute Of Technology
Bates Laboratory
26-411
Cambridge, MA 02139
milner@mitlns.mit.edu

Raju Venugopalan
Department of Physics
Building 510 A
Brookhaven National Laboratory
Upton, New York 11973
631-344-2341
raju@bnl.gov

Table of Contents

List of Figures

List of Tables

Executive Summary

By the end of this decade, the advancement of current and planned research into the fundamental structure of matter will require a new facility, the Electron Ion Collider (EIC). The EIC will collide high-energy beams of polarized electrons from polarized protons and neutrons, and unpolarized beams of electrons off atomic nuclei with unprecedented intensity. Research at the EIC will lead to a detailed understanding of the structure of the proton, neutron, and atomic nuclei as described by Quantum Chromo-Dynamics (QCD), the accepted theory of the strong interaction. The EIC will establish quantitative answers to important questions by delivering dramatically increased precision over existing and planned experiments and by providing completely new experimental capabilities. Indeed, the EIC will probe QCD in a manner not possible previously.

This document presents the scientific case for the design, construction and operation of the EIC. While realization of the EIC requires a significant advance in the development of efficient means of producing powerful beams of energetic electrons, an important consideration for choosing the site of the EIC is the planned upgrade to the Relativistic Heavy Ion Collider (RHIC) at Brookhaven National Laboratory. The upgrade planned for RHIC will fully meet the requirements for the ion beam for the EIC, providing a distinct advantage in terms of cost, schedule and the final operation.

The EIC will probe in detail the framework of Quantum Chromo-Dynamics. QCD was developed in the 1970s, primarily from the experimental discovery at Stanford Linear Accelerator Center of hard electron scattering from point like constituents in the proton. Since then, hard scattering experiments carried out at high-energy physics laboratories have provided information to determine, with good precision, the momentum distribution of the quarks in the nucleon and have shown that the energy dependence of hard scattering is described well by QCD. An important discovery that helped establish QCD was the determination of the running of the strong coupling constant and the property of asymptotic freedom of the strong interaction. However, there are still many unanswered questions.

- How do we understand the momentum distribution and spin structure of the proton and neutron in terms of the fundamental quarks and gluons?
- In the hard scattering process quarks or gluons are knocked out but only hadrons are seen in the final state. Can we understand this phenomenon of hadronization in terms of QCD?
- What is the role of quarks and gluons in understanding the microscopic structure of atomic nuclei, the basis of the physical world? In particular, what is the nature of short range internucleon forces?
- Can we observe new phenomena predicted by QCD involving saturation of gluons at high energies, similar to the Bose-Einstein condensation in atoms at low temperatures?

The current status of our understanding of the fundamental structure of matter is summarized in Section 2, while Section 3 explores the opportunities for obtaining quantitative answers to these questions with the capabilities available with the EIC

The EIC will collide high intensity (5-10 GeV) electron beams from high intensity (30-250 GeV) ion beams. The ion beam will be contained in a circular storage ring. The electron beam can be delivered to the interaction region in one of two ways: by a linear accelerator or by using a second storage ring. These different options are explored in detail in Section 4. In particular, the key elements of a Research & Development program are outlined in Section 4.2. In addition to the accelerator, sophisticated detectors will be needed to carry out the planned experiments at the EIC. One example of a detector is briefly described in Section 5.0.

The EIC developed from a series of workshops in the United States in 1999 and 2000 that attracted interested physicists from around the world. It received a strong endorsement from the US nuclear physics community at the 2001 Long Range Planning meeting as an important project that should receive R&D funds over the next several years to develop a single, optimized machine design with matching detectors. A collaboration will be formed in the Spring of 2002 to formulate a detailed construction proposal by 2005.

1.0 Introduction

The tremendous growth of knowledge about the fundamental structure of matter during the 20th century culminated in the 1970s with the emergence of the Standard Model. The Standard Model is an elegant theoretical framework based on experiment, which describes the structure of all matter in terms of point-like particles interacting by the exchange of gauge bosons. The point particles are termed leptons (electrons, neutrinos, etc.) or quarks (up, down, strange, etc.) and three types of gauge bosons; photons, weak bosons (W, Z), and gluons. Leptons can only exchange photons or weak bosons while the quarks may also exchange gluons. In addition, gluons, unlike photons, can interact with each other. The force governing the interaction of quarks and gluons is called the strong force. It is responsible for the structure of nucleons and their composite structures, atomic nuclei, as well as neutron stars.

Nucleons were born in the first minutes after the "Big Bang", and their subsequent synthesis into nuclei goes on in the ever-continuing process of nuclear synthesis in stars. Nuclear matter makes up most of the mass of the visible universe. It is the stuff that makes up our planet and its inhabitants. Nuclear matter was once remote and difficult for humans to access, but in the latter half of the 20th century, understanding nuclear matter and its interactions became central to research in nuclear physics and important to research in energy, astrophysics, and defense.

An essential goal of present day research is to investigate and understand the strong interactions between quarks and gluons that underpin the structure and interactions of nucleons and nuclei. The proposed Electron Ion Collider (EIC) is the essential next step needed to study the fundamental states of matter. We believe that it must be constructed by the end of the present decade to continue progress in this vital field of science.

1.1 Background and Scientific Questions

It is widely accepted that QCD is the exact theory of the strong interaction. QCD has a unique standing among all components of the Standard Model. It is the only theory that is not singular at short distances. The phenomenon of confinement ensures that QCD is well-behaved at large distances. Thus, QCD appears to be the only self-consistent nontrivial quantum field theory.

One of the greatest achievements of particle physics over the last 30 years was a quantitative verification of QCD in very hard collisions; those that occur over short distances at least 10 times smaller than the size of the proton. In hard collisions, the confined quarks and gluons act as if they are free particles exhibiting many properties that can be predicted by perturbative QCD (pQCD). However, when the interaction distance between partons (constituents of the nucleon) becomes comparable to or larger than the typical size of hadrons (pions and other heavier constituents that take part in the strong interaction), the partons are no longer free. They are confined by the strong force

that does not allow observation of any free "colored" object. In this regime where most hadronic matter exists, many of the symmetries of the underlying quark-gluon theory are hidden and simple calculational methods are no longer valid. This is a fascinating many-body problem where very strong forces obscure the relationship with the simple underlying theory. Understanding the relationship between the quark-gluon degrees of freedom and the hadrons that contain them is the most urgent challenge to any future experimental program in the domain of the strong interaction.

The most important difference between the theory of electromagnetic interactions, Quantum Electro-Dynamics (QED), and QCD is that gluons interact with each other while photons do not interact with other photons. This built-in non-linearity (non-Abelian structure) makes QCD calculations and theoretical predictions difficult, except in the high-energy (perturbative) or short space-time limit. The technical difficulties encountered in calculating QCD at the hadronic scale may be overcome by the use of lattice gauge calculations employing specifically designed powerful "tera-flop" computers. Over the next decade we expect that numerical computations of QCD will be extended into the non-perturbative regime. At that time, the properties of nucleons and nuclei will have a quantitative foundation in the fundamental theory. However, even at that time, the properties of hadrons at high energies will be well beyond the reach of the fastest computers. The thrust of this proposal is to provide physicists with an experimental tool that can explore all the partonic manifestations of QCD in nucleons and nuclei as well as explore the space-time structure of confinement.

Experimentally, the quark substructure of the nucleon was first revealed through electron-proton Deep Inelastic Scattering (DIS) experiments that took place at the Stanford Linear Accelerator Center (SLAC) in the early 1970s. These experiments earned a Nobel Prize for Friedman, Kendall, and Taylor. In a DIS collision, the electron transfers a large amount of energy and momentum. This energy and momentum is taken up by one of the quarks present in the proton. The struck quark carries a fraction of the proton's momentum, denoted by x, which is readily determined by the energy and momentum transferred in the collision. By varying the kinematics of the large momentum transfer scattering, on can measure the quark distribution as a function of that momentum.

A great deal has been learned since, at CERN, SLAC, Fermilab and DESY, about the quark and gluon structure of hadronic matter through measurements of quark and gluon distributions. In fact, the modifications of these distributions brought about by nucleons bound in nuclear medium were measured in groundbreaking experiments at SLAC, CERN and Fermilab. However, some of the crucial questions about the structure of hadronic matter remain open:

- What is the *structure* of hadrons in terms of their quark and gluon constituents?
- How do quarks and gluons *evolve* into hadrons through the dynamics of confinement?
- How do the quarks and gluons manifest themselves in the properties of atomic nuclei?

The term *"structure"* refers both to momentum distribution and to the spin carried by the various constituents. The answers to these questions are central to the ultimate characterization of the microscopic structure of strongly interacting matter.

However, a complete understanding of QCD and its full implications goes beyond these questions. The many-body aspects of QCD remain largely unexplored, and may contain a variety of surprises that can only be revealed by new measurements in domains that until now have been inaccessible. Finally, while today precision experiments test QED to its limits, similar explorations of QCD are incomplete because of the limitations in presently available experimental capabilities. Thus, there are a second group of questions:

- Does partonic matter saturate in a universal high-density state?
- Are there any long range correlations between produced partons?
- Can studies of the dependence of the parton densities on the nuclear density help constrain the properties of nuclear matter in the center of a neutron star?
- To what degree can QCD be demonstrated as an exact theory of the strong interaction?

1.2 The Electron Ion Collider (EIC)

The Electron Ion Collider is proposed as a means to obtain experimental answers to all of these questions. The design requirements are shaped by three decades of experimental work carried out with stationary or fixed targets at high-energy physics facilities such as SLAC, CERN, DESY, and Fermilab. In addition, a significant amount of effort was expended at DESY to investigate future polarized electron – proton (e - p) and unpolarized electron - ion (e - A) options. The inherent limitations of these facilities points to the need for a facility with the following characteristics:

- Collider geometry where electron beams collide with beams of protons or light and heavy nuclei,
- Wide range of collision energies (from E_{cm}/nucleon = 15 GeV to 100 GeV),
- High luminosity L = 10^{33} cm^{-2} s^{-1} per nucleon,
- Polarization of electron and proton spins, and
- Preferably, two interaction regions with dedicated, nearly hermetic, detectors.

Collider geometry offers two major advantages over fixed target electron-proton/ion (e - p/A) studies. First, the collider delivers vastly increased energy to the collision, providing a greater range for investigating partons with small momentum fractions (x) and their behavior over a wide range of momentum transfers (Q^2).

In DIS the accessible values of x are limited by the available collision center-of-mass energy. For example, collisions between a 10-GeV electron beam and nuclear beams of 100 GeV/nucleon provide access to values of x as small as $3x10^{-4}$. In a fixed target

configuration a 2.1 TeV electron beam would be required to produce the same collision energy. Figure 1.1 a-c shows the x-Q^2 range possible with the Electron Ion Collider and compares that range to the presently explored kinematic region. The beam energies assumed for the EIC are:

- 100 GeV/nucleon for nuclear beams,
- 50-250 GeV for polarized/unpolarized proton beams, and
- 5-10 GeV/c for polarized electron/positron beam.

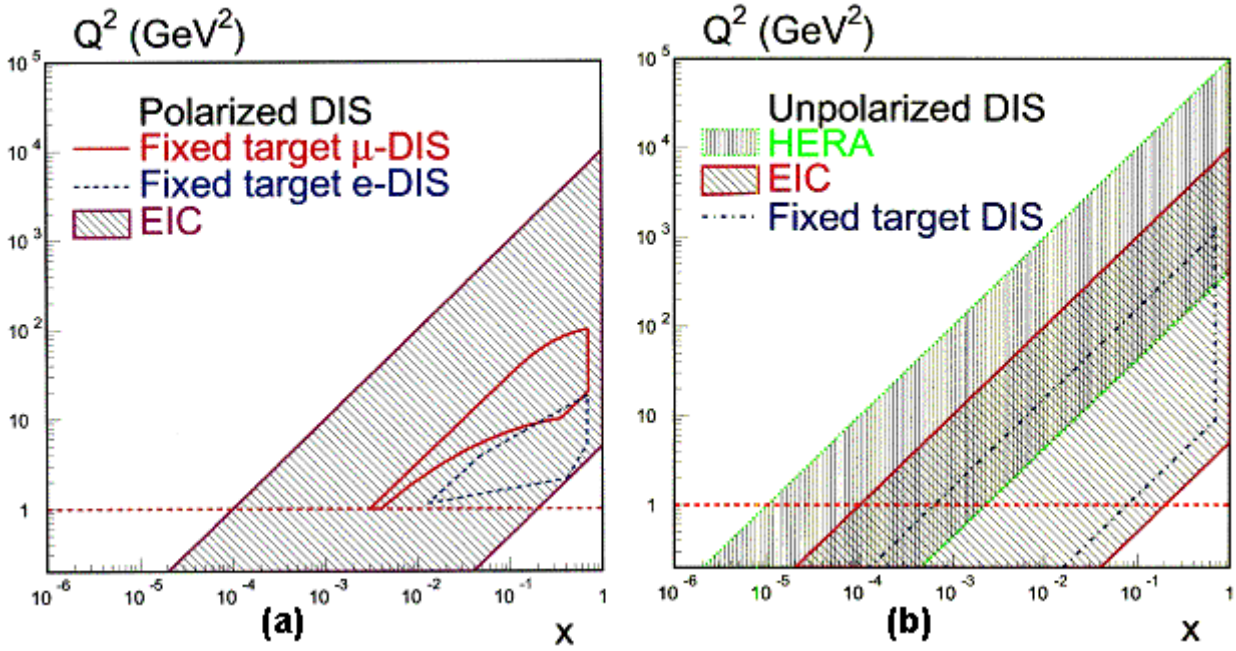

Figure 1.1: The x-Q^2 Range of the Proposed Electron Ion Collider

The x-Q^2 coverage of the EIC is compared with previously measured ranges. Figure (a) is for polarized lepton - nucleon DIS while (b) is for unpolarized lepton-nucleon and lepton - nucleus DIS, where leptons can be electrons or muons. Note that the HERA coverage in (b) is for e – p scattering only while the fixed target and the EIC regions also include DIS off nuclear targets.

The only electron-proton collider in existence is HERA, which is limited to unpolarized electron-proton collisions. Thus, in the case of electron-nucleus and polarized electron-polarized nucleon collisions the EIC is entering entirely new territory.

Secondly, the collider geometry is far superior to fixed-target experiments since it allows examination of final states of the target. If one wishes to examine the final state fragments from the struck nucleon or nucleus in fixed-target geometry, it is necessary to use a thin target so that the fragments can escape the target and be detected. The thin target makes acquisition of adequate statistics a serious problem. This is easily overcome in a high-luminosity collider, where high luminosity provides an adequate collision rate,

and the boost acquired by target fragments in the collider mode makes them readily available for detection when separated from the beam.

High luminosities of the order of $L=10^{33}$ cm^{-2} s^{-1} for electron-nucleon scattering, are a necessary and crucial characteristic of the EIC. It corresponds to observing 86 pb^{-1} per day. Previous studies established that significant results are attained at 200 $(pb)^{-1}$, therefore the statistical precision required for significant physics is easily within the reach of the EIC. This luminosity can be achieved with either of two accelerator scenarios: a ring-ring configuration, and a ring-electron linac configuration. Each has advantages. Achieving the proposed luminosities requires electron cooling of the ion beams (except at the highest proton energies) and intense electron beams of about 200 mA. While challenging, the intense electron beams are already available at the presently operating B-factories (SLAC and KEK B). The electron linacs (one for cooling the ion beam and another providing high-energy electrons in the collider) require full-energy recovery following the model of the full-energy recovery 50 MeV linac-based free electron laser at Thomas Jefferson Laboratory. Figure 1.2 shows the unique parameters of the EIC in the context of existing and planned lepton scattering facilities worldwide. The EIC will have higher energies than any existing fixed target machine and a higher luminosity than any existing collider.

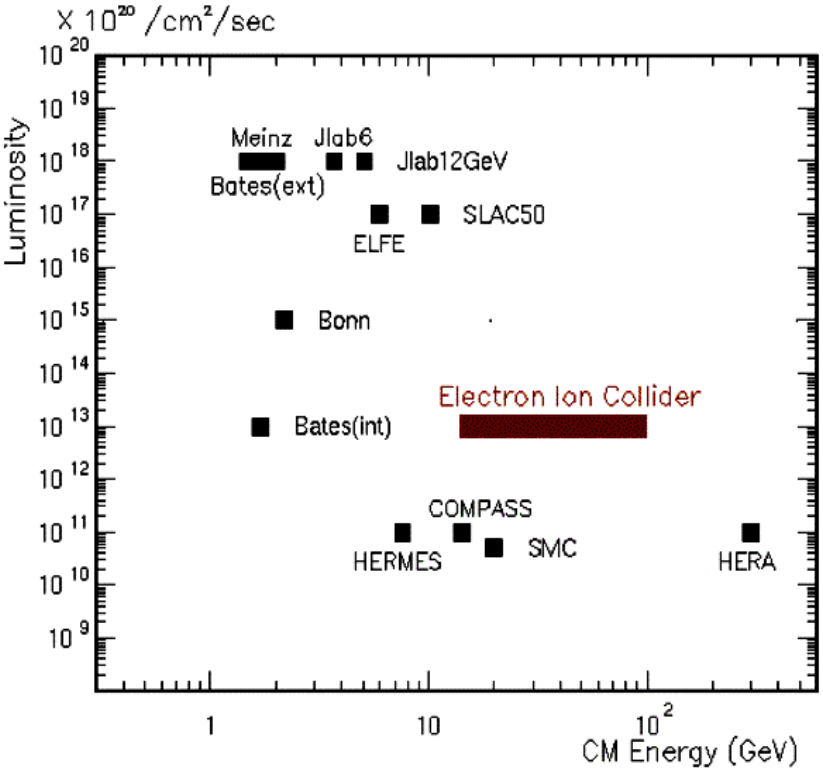

Figure 1.2: The Center-of-Mass Energy vs. Luminosity of EIC Relative to Other Facilities

The center-of-mass vs. energy of various existing facilities compared to that proposed for the Electron Ion Collider.

Two collider configurations have been considered in preliminary but realistic studies; one collides 5 GeV electrons with 50 GeV protons in a ring-ring configuration (the EPIC Study); a second collides 10 GeV electrons with 250 GeV protons or 100 GeV/A ions in the existing Relativistic Heavy Ion Collider storage rings (eRHIC). A "straw-detector"

concept reflecting the extreme asymmetry of the collisions also was developed and more specific designs are under consideration.

1.3 Highlights of Scientific Frontiers Open to the EIC

1.3.1 Quark and Gluon Distributions in the Nucleon

The EIC offers a unique capability for measuring "flavor tagged" structure functions by providing access to a wide range of final states arising from the fragmentation of the virtual photon. The collider geometry makes measurement of semi-inclusive reactions very efficient so that quark and gluon distributions in nucleons, nuclei, and possibly even mesons can be mapped in a flavor-tagged mode. This will provide a decomposition of the parton densities, over a large kinematic range, into the contributions from different parton types: up, down and strange quarks as well as gluons. For example, with clean kaon identification both the momentum and spin distributions of strange quarks can be determined with high precision down to $x \sim 10^{-3}$. The ability to tag the hadronic final state will allow measurements of the neutron structure function at large x, so that a reliable and precise determination of the ratio of the quark distribution in neutrons and protons can be made in a regime where several competing theoretical predictions exist.

1.3.2 Spin Structure of the Nucleon

Fixed target polarized DIS experiments yielded the surprising information that the quark spins account for only ~30% of the total spin of the nucleon. Recent results, with large uncertainty, indicate that gluons may play a significant role in constituting the nucleon's spin. While experiments with polarized protons at the Relativistic Heavy Ion Collider (RHIC) will provide significant information for unraveling the role of gluonic spin, energetic collisions using polarized electrons and protons will provide important complementary, and in some instances, essential new information using well established experimental methods and theoretical techniques presently used by the DIS community at HERA. The EIC, running at its highest energy, will provide crucial data at lower x than has been possible in any previous experiment. The use of tagging in polarized nuclei will allow measurement of the spin structure of the neutron at large x with better precision. At small x it will provide a separation between the polarization effects in the vacuum and nonvacuum channels. Determination of spin structure functions in this yet unmeasured low x region will bring a unique perspective to our understanding of pQCD. Direct measurement of the polarization of quarks in a broad range of x are needed to determine the polarization of quarks and antiquarks in the sea, currently a matter of controversy within sophisticated and successful models of the nucleon.

1.3.3 Correlations between Partons

A complete characterization of the partonic substructure of the nucleon must go beyond a picture of collinear non-interacting partons. It must include a description of the correlations between the partons densities over impact parameters, and a comparison of the parton wave functions of different baryons. Progress in this direction can be realized by measuring hard exclusive processes where, in the final state, a photon, a meson or several mesons are produced along the virtual photon direction, and a baryon is produced in the nucleon fragmentation region. These processes are expressed, as a result of the new QCD factorization theorems, through a new class of parton distributions termed *Generalized Parton Distributions* (GPD). The collider kinematics are optimal for detecting these processes. The presence of polarization provides additional exciting opportunities, for example, comparisons of the spin structure of hyperons and nucleons. If successful, such a program would greatly expand our knowledge about the role of non-perturbative QCD in hadronic structure.

1.3.4 The Role of Quarks and Gluons in Nuclei

Most hadronic matter exists in the form of nuclei. The ability of the EIC to collide electrons with light and heavy nuclei opens horizons fundamental to nuclear physics. For example, the role of quarks and gluons in nuclei may be investigated by comparing the changes in parton distributions per nucleon as a function of the number of nucleons. Seminal DIS experiments off nuclei showed that a) the distribution of quarks is altered by the nuclear medium from that observed in nucleons, b) led to the discovery of the lack of enhancement of sea quarks in the nuclei that was expected based on models of the meson picture of nuclear forces, and c) provided tantalizing indications of significant modifications of the gluon distributions at moderate x. Studies of parton modifications at $x \sim 0.1$ will be most sensitive to the underlying quark-gluon structure of the internucleon interactions that are usually described within effective low energy mesonic theories. It is particularly important to establish the quark distributions at small values of x where the presence of the other nucleons in the nucleus will alter ("shadow") the partonic distributions. A nuclear enhancement of valence quarks, sea quarks, or gluons would indicate the relative importance of meson, quark, and gluon exchange at various distance scales.

1.3.5 Hadronization in Nucleons and Nuclei

How do the colored quarks and gluons knocked out of nucleons in DIS evolve into the colorless hadrons that must eventually appear? This process is one of the clearest manifestations of confinement: the asymptotic physical states must be color-neutral. Hadronization is a complex process that involves both the structure of hadronic matter and the long range nonperturbative dynamics of confinement. A fundamental question related to hadronization is how and to what extent the spin of the quark is transferred to its hadronic daughters. The ability to "tag flavor" and a facility that creates readily

detectable jets are crucial for these experiments. The EIC makes it possible to strike quarks and observe the complete array of decay products from the nucleon or nucleus. The fact that nuclei also may be used is essential to this study. The ability to place varying amounts of nuclear matter in proximity to the system produced forward along the photon direction and the recoiling quark system, allows one to perturb in a controlled way the early stages of its space-time evolution, and to measure the energy imparted to the nuclear matter by the emerging parton.

1.3.6 Partonic Matter Under Extreme Conditions

Very high energy DIS on nuclear targets with electromagnetic probes offers new opportunities for studying partonic matter under extreme conditions. Particularly intriguing is the regime of very low x ($x < 10^{-3}$) where gluons dominate. Measurements of the proton structure function showed that the gluon distribution grows rapidly at small x for Q^2 greater than a few GeV^2. When the density of gluons becomes large, they may saturate and give rise to a new form of partonic matter: a **color glass condensate**. It is a colored glass because the properties of the color-saturated gluons are analogous to that of a spin glass system in condensed matter physics. It is a condensate because the gluons have a large occupation number and are peaked in momentum about a typical scale of the saturation momentum Q_s.

This state of strongly interacting matter would be universal in that it is insensitive to the hadronic matter in which it resides. The gluonic density/cm^2 is enhanced in nuclei relative to that in individual nucleons by a factor $A^{1/3}$. Therefore, high parton density effects will appear at much lower energies in nuclei than in protons. The Electron Ion Collider, with its nuclear beams and e - A center-of-mass energies of at least 60 GeV, and ability to study inclusive and semi-inclusive observables, will probe this novel regime of Quantum Chromo Dynamics.

2.0 Current Status of the Partonic Structure of Hadrons and Nuclei

In this section, we present an overview of the current status of hadron structure. Section 2.1 summarizes our present knowledge of parton distributions in the nucleon. These have been determined using hard scattering processes at high-energy facilities. In Section 2.2 we describe the current understanding of the spin and flavor structure of the nucleon as probed by hard scattering processes, and Section 2.3 summarizes the modification of these parton distributions in nuclei. Section 2.4 discusses space-time correlations in QCD.

2.1 Parton Distributions in the Nucleon

In the decades since the discovery of Deep Inelastic Scattering (DIS), research focused on measuring inclusive DIS over a large kinematic range (Figure 2.1).

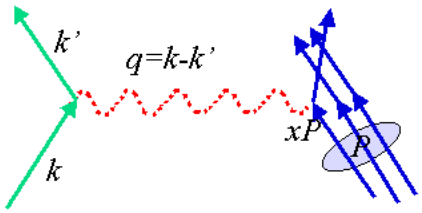

Figure 2.1: Deep Inelastic Scattering
This figure illustrates the kinematics of DIS.

This emphasis is a direct consequence of the dependence of the double differential cross-section on the nucleon structure function F_2. In the single photon exchange approximation, the expression for the double differential cross-section is:

$$\frac{d\sigma}{dxdQ^2} = \frac{2\pi\alpha^2{}_{em}}{Q^4 x}[F_2 Y_+ - y^2 F_L] .$$

In this expression (See Figure 2.1):

$Q^2 = -q^2$ is the four momentum squared carried by the virtual photon.

$y = q \bullet p / p \bullet k$ is the inelasticity.

$x = Q^2 / 2p \bullet q$ is the Bjorken variable.

s = $(p + k)^2$ is the center-of- mass energy squared.

Y_+ is defined as $1 + (1-y)^2$.

α_{em} is the Quantum Electro Dynamic coupling constant.

F_L is the longitudinal structure function of the proton, which is discussed below.

The measured structure function, $F_2(x,Q^2)$, is related to the quark and anti-quark distribution in the leading logarithmic approximation by the following expression:

$$F_2(x,Q^2) = \sum_{i=u,d,c,s,t,b} e_i^2 (xf_i(x,Q^2) + x\bar{f}_i(x,Q^2)).$$

In this approximation, $f_i(x,Q^2)$ ($\bar{f}_i(x,Q^2)$) is the probability of finding a quark (anti-quark) of flavor i and charge e_i with momentum fraction x at a 4-momentum transfer Q^2.

Because of the lower energy, SLAC data were restricted to the valence quark region ($x \geq 0.1$) [1]. Once CERN and Fermilab were available to produce sufficiently intense muon beams with energies in excess of 100 GeV, the DIS cross-section on the proton was measured down to and below $x = 10^{-3}$ [2]. In the 1990's, the HERA collider extended the DIS cross-section on the proton to below 10^{-4} [3,4]. Today, an experimental determination of $F_2^p(x,Q^2)$ exists for more than 4 orders of magnitude in x and Q^2, as shown in Figure 2.2 [5].

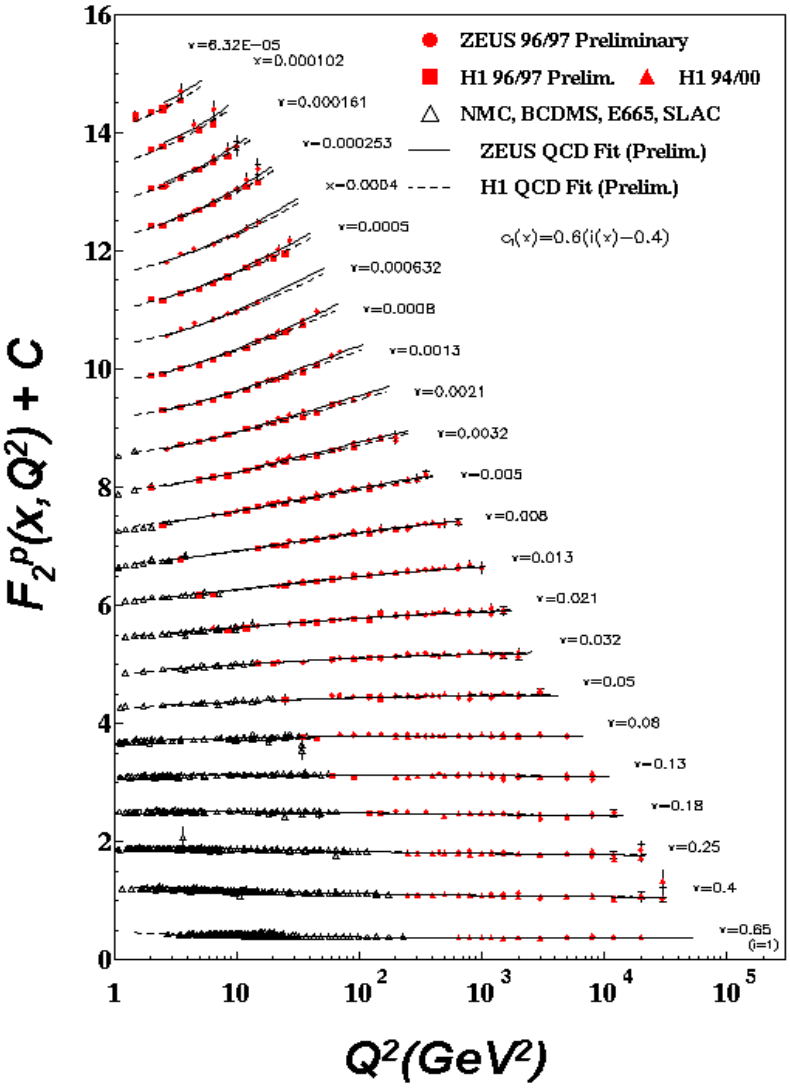

Figure 2.2: F_2 (x) at Fixed x vs. Q^2

These data [5] are from HERA and fixed target experiments, together with Zeus and H1 QCD fits.

In addition to providing a determination of the parton distribution of the nucleon, these data provide one of the experimental cornerstones of Quantum Chromo-Dynamics. Typically, the parton distributions, f_i, are determined from a global fit to the world's data on DIS and other hard scattering data. The basic procedure involves parameterization of the $f_i(x,Q^2)$ at a low value of $Q^2 = Q_0^2$ such that the $f_i(x,Q^2)$ can be calculated at higher Q^2 by using Next-to-Leading-Order (NLO) Dokshitzer-Gribov-Lipatov-Altarelli-Parisi (DGLAP) evolution equations [6,7]. Data are fitted for all $Q^2 > Q_1^2$, where $Q_1^2 > Q_0^2$ is a value of Q^2 where perturbative QCD (pQCD) is believed to make the dominant contribution. The dramatic rise of F_2 with increasing Q^2 at low x is in excellent agreement with the theoretical predictions.

Figure 2.3 shows one set of parton distributions.

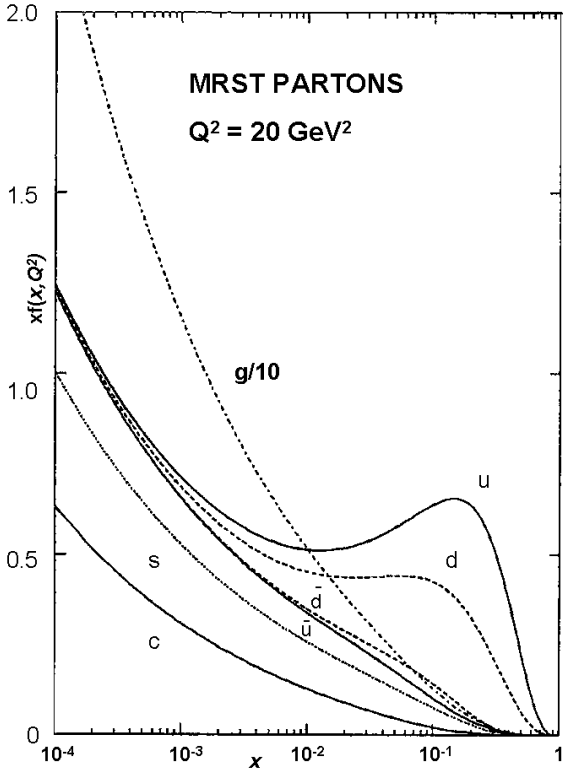

Figure 2.3: Parton Distributions (MRST) at Q^2 = 20 (GeV/c)^2

Parton distributions as a function of Bjorken x for a fixed value of Q^2 = 20 GeV^2. The plots are obtained from the global analysis of MRST [6] of hard scattering data using linear DGLAP QCD evolution equations. The role of valence quarks is exaggerated. The distributions for u and d quarks ride on a large background of u and d sea quarks, and the gluon distribution is 10 times larger than shown.

Note the

- Dominance of the *u* and *d* valence quark distributions at large *x*,
- The rise of the sea quark distributions ($\bar{u}, \bar{d}, s, c$) at low *x*, and
- The large size of the gluon distribution *g(x)* at low *x* (ten times larger than shown in Figure 2.3).

In this type of global analysis, data from other types of hard processes such as DIS scattering of neutrinos, Drell-Yan (D-Y) production, and prompt photon production, are included. The fraction of the total momentum of the proton carried by the various partons (e.g., strange quarks carry 4.6 % of the proton's momentum at Q^2 = 20 (GeV/c)^2),

can be determined from the parameterizations of Figure 2.3. Further, the global fit contains the QCD parameter $\Lambda_{\overline{MS}}\left(n_f = 4\right) = 300\,\text{MeV}$. It corresponds to a value of the strong coupling constant, $\alpha_s\left(M_Z^2\right) = 0.1175,$ which is in excellent agreement with the world average value $\alpha_s\left(M_Z^2\right) = 0.118.$ This type of precise information is the hallmark of DIS. The predicted rise of F_2 with increasing Q^2 at low x was first observed at HERA and provides a determination of the gluon distribution. The gluon distribution evolves rapidly with Q^2, as shown in Figure 2.4 [8].

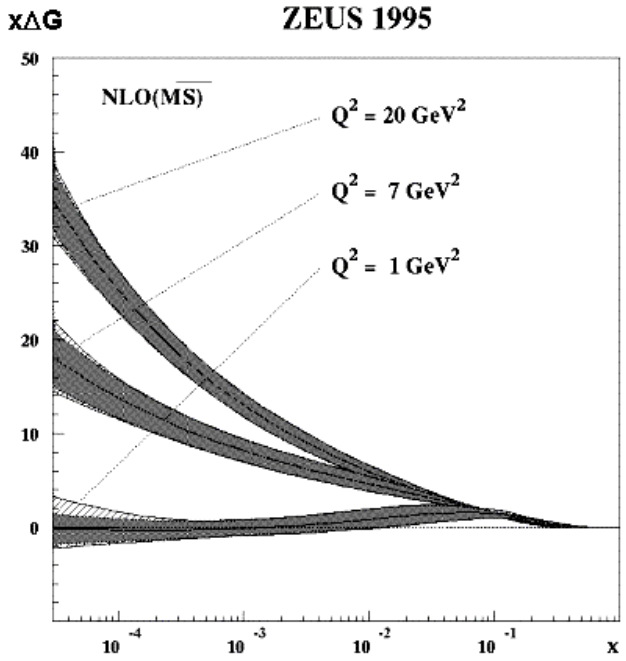

Figure 2.4: The Gluon Momentum Distribution $x\,G(x,Q^2)$ As a Function of x at Fixed Q^2

Q^2 values of 1, 7, and 20 GeV/c^2. *These data are from the ZEUS QCD fit [8].*

In Figure 2.4 the gluon distribution for Q^2 = 1 GeV^2 shows the following interesting features. The gluon distribution is comparable to the quark and anti-quark distribution at $x \sim 0.1$. In fact, gluons carry nearly half the nucleon momentum even at a low-resolution scale of $Q^2 \sim 1$ GeV^2. Therefore, the gluons play an important role in the nonperturbative nucleon wave function. Secondly, the gluon distribution at small x has a very different trend from those at the higher Q^2. It is smaller than the sea quark distributions in the ZEUS QCD fit. However, the systematic experimental uncertainties in the extraction of gluon densities are large in this region. In addition, higher twist effects may be large. This suggests a breakdown of the leading twist DGLAP analysis. Currently, accurate knowledge of the gluon densities for $x \le 0.05$ is limited to $Q^2 \ge 5\text{-}7$ GeV^2 where the sensitivity is limited to the nonperturbative gluon input.

There also are considerable systematic uncertainties in determining gluon densities at large x and moderate Q^2. The database of hard processes dominated by the scattering off gluons is insufficient for $x \ge 0.2$ and Q^2 of a few GeV^2.

2.2 Spin and Flavor Distributions in the Nucleon

An important goal of hadronic physics is to understand the spin structure of the nucleon as reflected in the constituent partons. In spin-dependent DIS, with polarized leptons and nucleons, the inclusive spin asymmetry is proportional to the spin-dependent structure function $g_1(x,Q^2)$. By analogy to F_2 in unpolarized DIS, $g_1(x,Q^2)$ is a charge weighted sum over flavors of the spin-dependent parton distribution, $\Delta f_i(x,Q^2)$:

$$\Delta f_i(x,Q^2) = f_i(x,Q^2)\uparrow + \bar{f}_i(x,Q^2)\uparrow - f_i(x,Q_2)\downarrow - \bar{f}_i(x,Q^2)\downarrow.$$

In this expression, $\uparrow$ ($\downarrow$) indicates the parton spin parallel (or antiparallel) to the spin of the nucleon. The integrated spin-dependent parton distribution, $\Delta f_i(Q^2) \equiv \int_0^1 dx \Delta f_i(x,Q^2)$, is the total fraction of the nucleon's spin carried by the quark flavor f_i. When the principle of conservation of angular momentum is applied to the constituents of the nucleon, the spin projection of the nucleon can be expressed as

$$\frac{1}{2} = \frac{1}{2}\Delta\Sigma + \Delta G + L.$$

$\Delta\Sigma$ (= $\Delta u + \Delta d + \Delta s$) is the total quark contribution, ΔG is the total gluon contribution, and L is the contribution from orbital angular momentum of the quarks and gluons. It must be noted that these contributions are dependent on the renormalization scheme.

There has been considerable progress in measuring spin-dependent DIS over the last decade in fixed target experiments at SLAC [9], CERN [10] and DESY [11].

- The spin-dependent structure function g_1 was determined for both the proton and neutron by inclusive scattering over two orders of magnitude in x and Q^2.
- $\Delta\Sigma$ was determined to be considerably smaller (~0.3) than the value predicted by the simple quark model.
- Next-to-Leading-Order analysis of the world's polarized DIS data is now possible and suggests that the gluon polarization is large. Figure 2.5 shows the results from a NLO pQCD analysis of the world's data on inclusive lepton-nucleon scattering [10] to determine the polarized parton distribution.
- A major triumph for QCD and the precision of these experiments was the verification at the level of 5% [9] of the Bjorken Sum Rule prediction for $\int_0^1 ((g_1^p(x,Q^2) - g_1^n(x,Q^2))dx$. Theoretically, the calculation involves pQCD to third order in α_s. It also requires knowledge of target mass and twist-4 corrections. The data were obtained with a new generation of polarized beams, targets, and spectrometers.
- There has been significant progress in decomposing $\Delta\Sigma$ into contributions from different quark flavors using flavor tagging in semi-inclusive scattering. Figure 2.6 shows the present status of the polarized valence quark, sea quark and gluon distributions from semi-inclusive DIS measurements of SMC and HERMES.

Figure 2.5: The Status of Polarized Parton Distributions and Their Uncertainties.

These distributions were extracted from a NLO pQCD analysis of the world sample of published inclusive polarized DIS data (as of 1998) [10]. The uncertainties shown with the best fit (cross hatch) are statistical. The middle error band (vertical hatch) is the experimental systematic uncertainty and the lowest error band (horizontal hatch) is the theoretical uncertainty in the pQCD analysis method. The largest uncertainty exists in the polarized gluon distribution. The singlet quark and non-singlet quark distribution are determined with much smaller uncertainties.

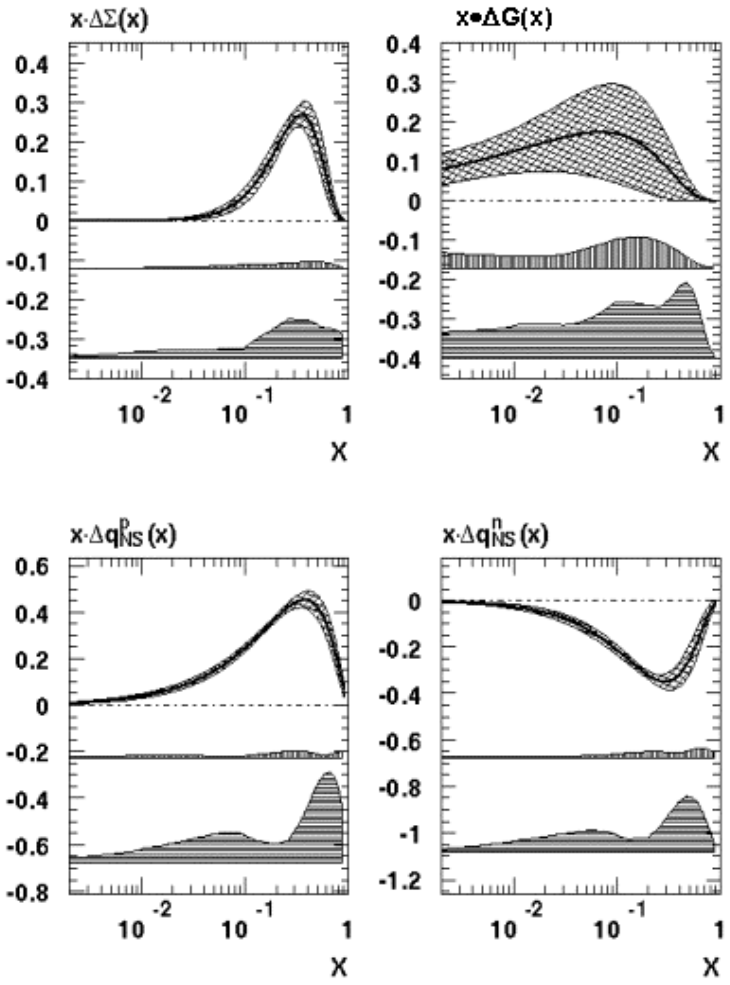

The role of nonperturbative phenomena in forming parton densities is a key to understanding the nucleon structure. There are indications that nonperturbative effects are important in forming the gluon densities. One important finding of the deep inelastic and Drell-Yan experiments is that the dominant contribution to the light quark (*u, d*) sea at intermediate Q^2 is nonperturbative and the perturbative (photon-gluon fusion) contribution is small. Two complementary lines of evidence point to this conclusion. One observation, originating from DIS neutrino experiments, is a strong suppression of the strange sea compared to the non-strange sea at Q^2 of a few GeV^2 despite the small value of the strange current quark mass. A second piece of evidence is the observation of

a significant difference of $\bar{u}$ and $\bar{d}$ distributions. These should be equal if the nucleon sea is created entirely by pair production from gluons. Since the small masses of the up and down quarks are far below the confinement scale, and the exclusion principle has little impact, one expects that the up and down quark seas would be symmetric in the absence of non-perturbative physics.

Figure 2.6: Status of Experimental Determination of Polarized Valence Quark, Sea Quark, and Gluon Distributions.

$x\Delta u_v, x\Delta d_v, x0.5\left(\Delta\bar{u}+\Delta\bar{d}\right)$ and $x\Delta G$ are shown as a function of x for Q^2=2.5 GeV^2. The values represented by the circles and the open triangles were derived from inclusive and semi-inclusive DIS at HERMES and SMC (the lower areas indicate the systematic uncertainties in the HERMES measurement). The circle represents the only direct measurement of ΔG, derived in LO QCD from the asymmetry in the photo-production of high p_t hadron pairs at HERMES; no theoretical uncertainty is included. The full curves represent current parameterizations of the polarized parton distributions derived from inclusive measurements; the dotted curves correspond to maximum polarizations of unity. (The 3 different curves for xΔG(x) represent a small sub-sample of all curves compatible with existing data.)

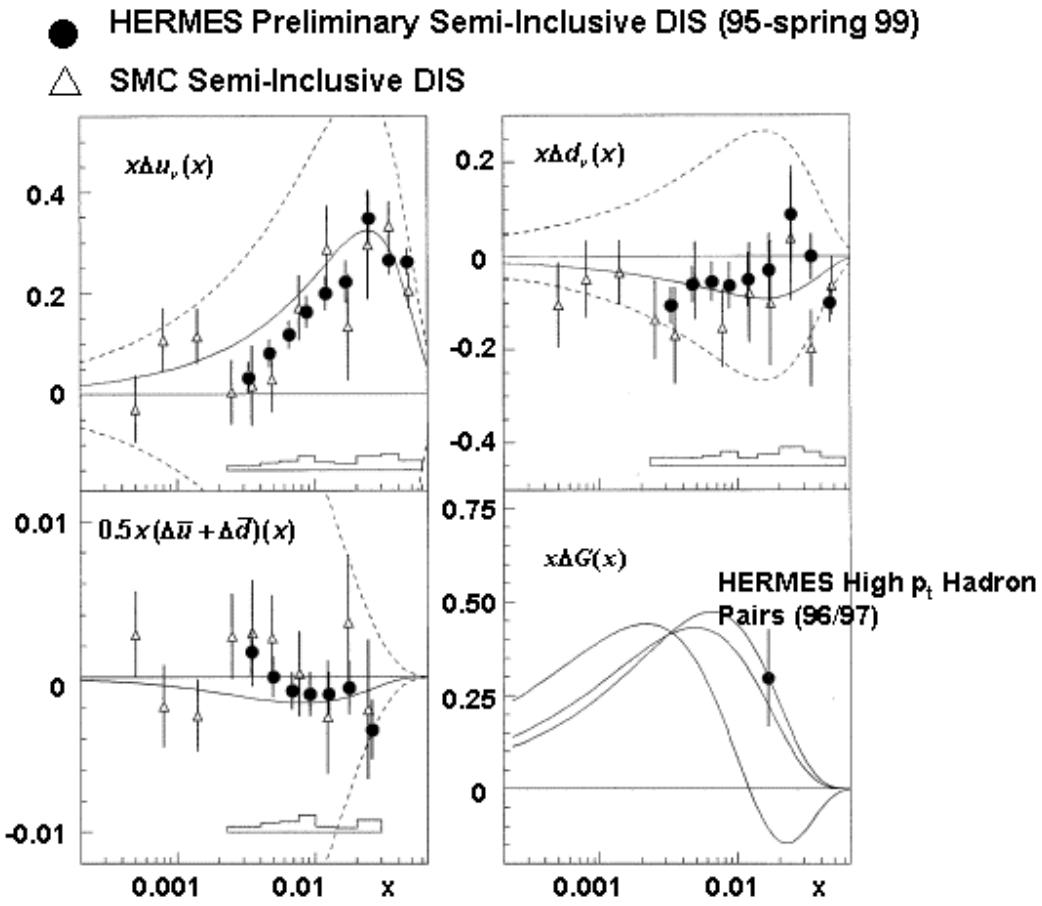

However, DIS measurements comparing the structure function of the proton to that of deuterium do not support this picture. The NMC experiment [12] demonstrated that the integral of $F_2^p(x)$ - $F_2^n(x)$ over x (neglecting shadowing effects in electron-deuteron scattering) was 0.235 ± 0.026 rather than the expected value of 1/3. The difference means that the integral of $\bar{d}(x) - \bar{u}(x)$ for the proton equals 0.149 ± 0.039.

This was pursued at Fermilab [13] by a relative measurement of the Drell-Yan yield from deuterium to that from the proton. This type of measurement can be made directly sensitive to the $\bar{u}$ and $\bar{d}$ content of the targets. The measurement showed that the deuterium Drell-Yan yield was much greater than twice that of the proton. Using charge symmetry, the ratio of these yields can be converted to the ratio of $\bar{d}_p(x)/\bar{u}_p(x)$ for the proton, or $\bar{d}_n(x)/\bar{u}_n(x)$ for the neutron. These ratios are shown in Figure 2.7 (a). Figure 2.7 (b) shows $\bar{d}_p(x) - \bar{u}_p(x)$ extracted from this ratio compared to HERMES data. The value of the integral of the difference is 0.118 ± 0.011, in good agreement with the value extracted from DIS (0.149 ± 0.039) [14] and shown in Figure 2.7. The observed asymmetry can be described in a number of nonperturbative models of the nucleon. One of these includes a class of models that considers fluctuation of the proton into NB and)B states. Here the asymmetry is due primarily to larger amplitude of $p \rightarrow n\mathrm{B}^+$,)B. [15,16,17]

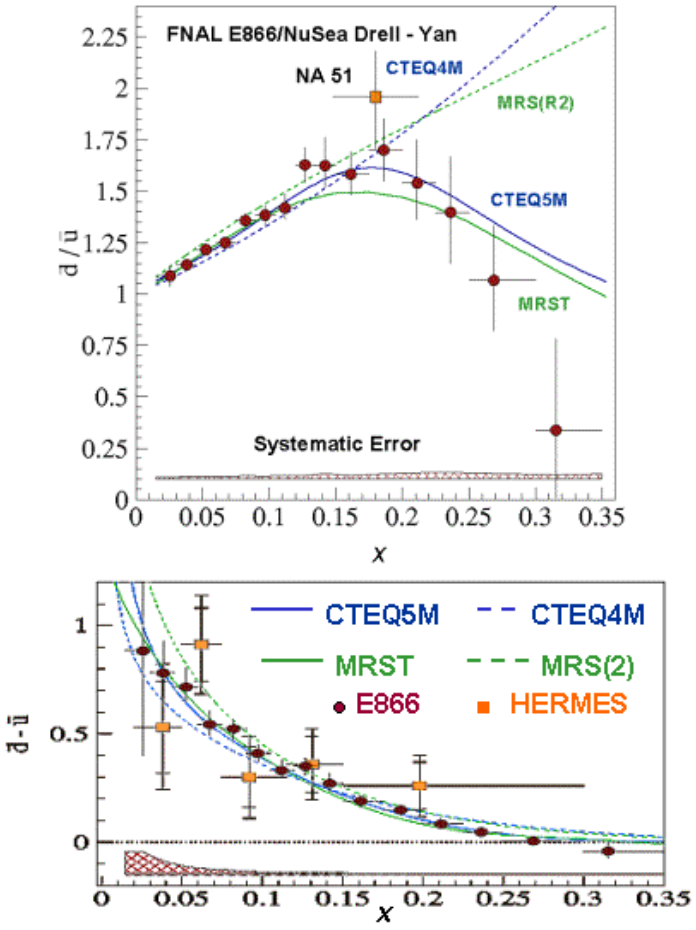

Figure 2.7: Ratio $\bar{d}(x)/\bar{u}(x)$ from the Charge Symmetry Ratio of the Drell -Yan Yields

(a) The ratio $\bar{d}_n(x)/\bar{u}_n(x)$ in the proton as measured from the relative Drell-Yan yields from the difference (b) $\bar{d}(x) - \bar{u}(x)$ in the proton, using the values of $\bar{d}(x)/\bar{u}(x)$ from above and $\bar{d}(x) + \bar{u}(x)$ from measured parton distributions.

The other two types of models are those in which pions are emitted by constituent quarks [18], and the chiral soliton models [19] where the asymmetry is caused by the different deformation of the Dirac *u* and *d* sea by the soliton field. A critical experiment that would discriminate between the pion model of the sea and chiral soliton dynamics is measurement of the polarization of the sea. This polarization is negligible in the pion model while in the chiral soliton model the $\bar{u} - \bar{d}$ asymmetry should be larger in the polarized case than in the unpolarized case. (See Figure 2.8)

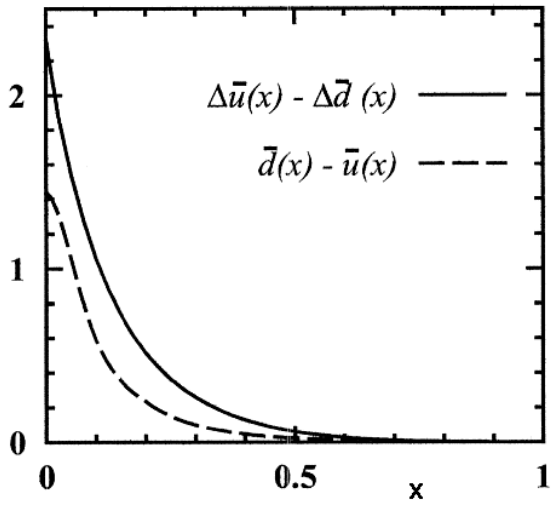

Figure 2.8: Predictions From the Chiral Soliton Model

The dashed curve is a prediction for the unpolarized case [19]. It is consistent with the experimental data in Figure 2.7. The solid curve is a prediction for the polarized case showing an enhancement of asymmetry for the polarized sea.

2.3 Nuclear Modifications

The conventional description of a nucleus states that it is a collection of nucleons, weakly bound in a potential created by their mutual interaction. Therefore, many were surprised when the EMC experiment [20] uncovered a systematic nuclear dependence to the nuclear structure function $F_2^A(x,Q^2)$ in iron when compared to deuterium. The effect reached 20% for $x \sim 0.5$. This is significantly larger than a natural scale ($\leq 5\%$) for nuclear effects that is given by the ratio of the binding energy or the kinetic energy per nucleon to the nucleon mass. A host of dedicated fixed target experiments [21,22,23] confirmed the existence of the nuclear dependence but with some significant modifications of the original EMC results at small *x*. Figure 2.9 (a) shows an idealized version of nuclear modification of the relative structure functions per nucleon. It is 2/A times the ratio of a measured nuclear structure function of nucleus A to that for deuterium. The rise at the largest values of *x* is ascribed to the nucleon's Fermi momentum. The region above $x \geq 0.1$ is referred to as the EMC effect region. When $x \leq 0.05$, the nuclear ratio drops below one. This is usually referred to as the nuclear shadowing region. Figure 2.9(b) presents a sample of the data that produced high precision relative structure functions over a broad range in A, *x* and Q^2. A recent review [24] contains a summary of the data and the various interpretations.

Figure 2.9: Ideal and Measured Nuclear Modification of the Relative Structure Functions Per Nucleon

Figure (a) shows an idealized version of the ratio of the structure function of a nucleus, $F_2^A(x,)$ per nucleon to $F_2^d(x)$ of deuterium. Figure (b) shows the measured $F_2(x)$ structure functions for C, Ca, and Xe relative to deuterium.

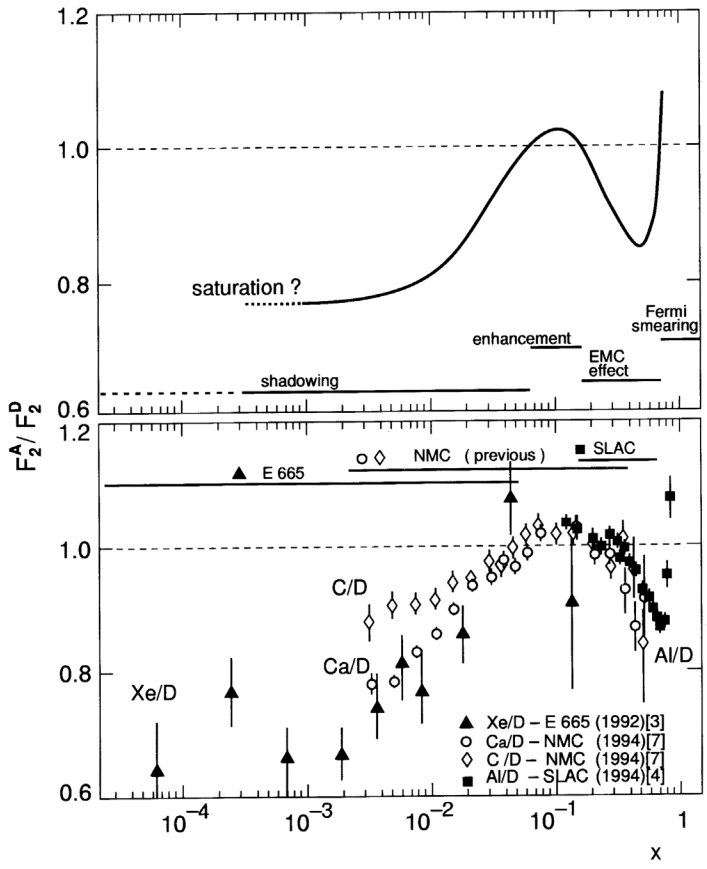

2.3.1 The EMC Effect and Anti-Quarks in Nuclei

A popular interpretation of the EMC effect is based on models where internucleon interactions at a wide range of internucleon distances are mediated by meson exchanges. The traditional theory [25,26] of nuclear interactions predicts a net increase in the distribution of virtual pions in nuclei relative to that of free nucleons because the meson interactions are attractive in nuclei. In these models nuclear pions may carry about 5% of the total momentum to fit the EMC effect at $x \geq 0.3$. Each pion carries a light-cone fraction of about 0.2-0.3 of that for a nucleon.

The possibility of scattering sea antiquarks belonging to the nuclear pions off a hard probe led to a predicted enhancement of the nuclear sea of 10% to 15% for $x \sim 0.1$ - 0.2 and for $A \geq 40$. This enhancement was expected because conventional nuclear matter theory predicts that the number of exchanged mesons increases [25] with nuclear density. This conventional view of nuclear binding is challenged by the constancy with A of the

antiquark distribution. Surprisingly, no enhancement was observed on the level of 1% accuracy in the Drell-Yan experiments (see Figure 2.10).

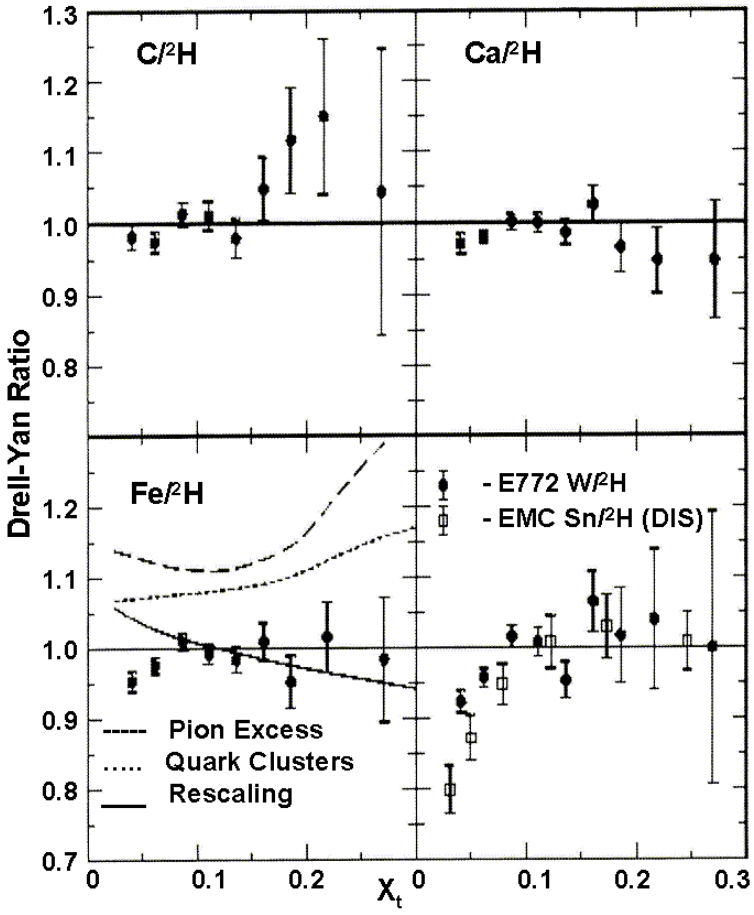

Figure 2.10: The Ratio of the Antiquark Distribution Per Nucleon Relative to Deuterium

This figure shows data from a Drell-Yan experiment [27] for the antiquark ratio in nuclei relative to the deuteron and compared with the theoretical predictions and the EMC data for the F_2 ratio for tin and deuterium.

More recently, preliminary results [28] from Thomas Jefferson Laboratory indicate that there is no observable pion excess in the A $(e,e'\mathrm{B})$ experiment (E91-003). A number of authors [29] point out that one can readily adjust parameters of the pion interactions in nuclei to reduce the pion excess to a level consistent with the Drell-Yan data. Energy excitation for the residual nuclear system also reduces the contribution of pions to the nuclear parton densities [30]. However, this would reduce to a negligible level the role of pions in the EMC effect for F_2^A.

Several joint QCD analyses of the nuclear DIS and Drell-Yan data combined with the application of the baryon charge and momentum sum rules [31,32,33] provided further information on the nuclear effects for the parton densities. These analyses indicate that the valence quark distribution in nuclei is enhanced at $x \sim 0.1 - 0.2$, while the gluons in nuclei carry practically the same fraction of the momentum (within 1%) as in a free nucleon. Assuming that the gluon shadowing is similar to that for quarks, these analyses predict a significant enhancement of the gluon field in nuclei at $x \sim 0.1 - 0.2$.

2.3.2 Nuclear Shadowing

Shadowing is best understood from the space-time evolution of highly relativistic collisions. The (- *p* cross-section is only 0.1mb [34] for energies in excess of 2 GeV. This corresponds to a mean-free-path of more than 100 fm in nuclear matter. While the high-energy γ - A cross-section might be expected to be proportional to A this is not the case. The observed increase in the cross-section is smaller than A times the (- *p* cross-section. This is because the photon can fluctuate into a $q\bar{q}$ pair that has a cross-section typical of the strong interactions (20mb) and is absorbed readily (mean-free-path = 3.7 fm). If the fluctuation persists over a length greater than the internucleon separation distance (2 fm), its absorption "shadows" it from encountering subsequent nucleons. The coherence length of the virtual photon's $q\bar{q}$ fluctuation with typical mass of the order $\sqrt{Q^2}$ is $l_{coh} = \frac{1}{2m_n x}$. Therefore, the onset of shadowing is expected and observed at $x \sim 0.05$. Based on this picture, shadowing should become a weak function of x when the coherence length becomes long compared to the nuclear diameter ($l_{coh} > 2.4A^{1/3}$). Studies of the possible saturation of shadowing in heavy nuclei requires measurements at $x \sim 10^{-3}$. Figure 2.8b shows data from the fixed target experiments NMC and E665, demonstrating that high quality data exists only for $x > 4 \times 10^{-3}$. The E665 data below $x = 10^{-3}$ have Q^2 below 1 GeV^2 and decreasing further with decrease of Q. The uncertainty associated with analyzing these data makes their interpretation in terms of parton densities difficult. Furthermore, deep connections may exist between the phenomenon of shadowing and that of parton saturation and the behavior of matter at very high density. Again, the existing data lack the dynamic range of Q^2 at fixed x to address this physics convincingly.

2.3.3 Gluon Distributions

Our knowledge of the nuclear gluon structure functions ($G_A(x,Q^2)$) is nearly non-existent when compared to our current knowledge about the quark distributions in nuclei. The only direct indications of the gluon modification in nuclei come from two NMC high precision measurements of the ratio of the DIS of tin (Sn) and carbon (C). The first experiment [14] measured the ratio of inclusive J/ψ production off the two nuclei and showed an enhancement of the ratio by about 10%. Using the gluon fusion model this can be interpreted as a ratio of the gluon densities in Sn and C for $0.1 < x < 0.2$. Another measurement of the scaling violation for the ratio of F_2^{Sn}/F_2^{C} showed an increase of the ratio with increase of Q^2 consistent with predictions [31,32]. Gousset and Pirner [35] noted that this measurement actually allows a fairly direct measurement of the A-dependence of the gluon density provided higher twist effects are neglected. Since the ratio is close to one in a wide x range, the main contribution to the scaling violation comes from the gluon contribution to the scaling violation. As a result, the scaling violation is proportional to the deviation of the ratio of the nuclear gluon densities from 1. The result of this extraction [35] is also shown in Figure 2.11. It suggests a significant enhancement of the gluons in heavier nuclei at $x \sim 0.1$.

Figure 2.11: Ratios r*(x)* and $f_1(x)$

The ratio, r(x) of the per nucleon gluon distributions in Sn *relative to* C *and the ratio, $f_1(x)$ of their $F_2(x)$ structure functions [35]. The box represents the extraction of r(x) from J/ψ electro-production in the process $\mu + A \rightarrow \mu + J/\psi + X$.*

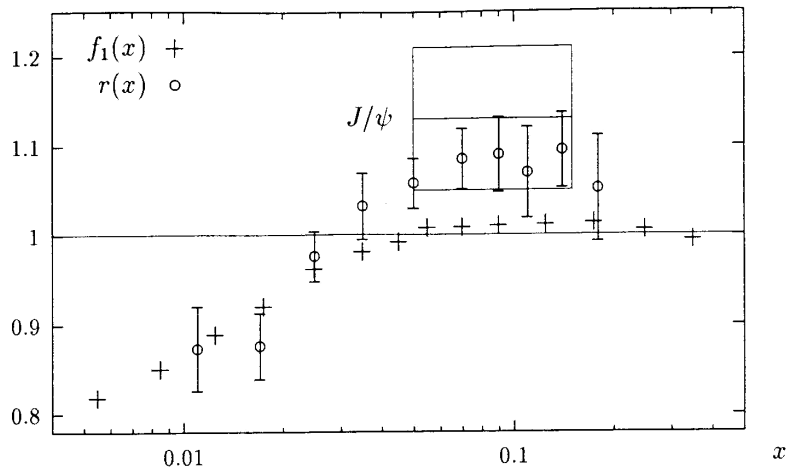

$$r_{A,d}(x) = \frac{d\left(\frac{F_2^A(x,Q^2)}{F_2^d(x,Q^2)}\right)}{d\ ln\ Q^2} \quad .$$

The current data appear to indicate a very provocative picture of parton nuclear densities in the $x \sim 0.1 - 0.2$ region, which corresponds to distances of ~ 1 – 1.5 fm. In the context of space-time correlation (Section 2.4), this is comparable to the scale of distances for medium range and short range internucleon forces. The gluon and valence quark fields are enhanced while the sea is somewhat suppressed. Qualitatively, this may point to the importance of nucleon-nucleon forces that originate from gluon-induced interactions between nucleons, as well as forces due to the valence quark interchanges between nucleons [35,36].

2.3.4 Nucleon Fragmentation and Pion Parton Densities

Recent advances in QCD allow analyses of the Q^2 evolution of semi-inclusive DIS scattering where a hadron, h, is fixed in the nucleon fragmentation region with a fixed Feynman x_h and a fixed transverse momentum. The QCD factorization theorem states that the "conditional parton distribution functions [37] or extended fracture functions" [38] satisfy the same QCD DGLAP evolution equations as the inclusive structure functions. The first studies of these processes were performed at HERA for diffractive kinematics when h is a proton with x_p close to 1, and for the fragmentation kinematics where both protons and neutrons can be detected. The data are consistent with the factorization theorem though not detailed enough to claim the confirmation of this important property of QCD.

Researchers explored the production of leading neutrons as a way to study the parton structure of the pions. This work was complementary to studies of the Drell-Yan process of pion-nucleon scattering [39]. The information is important for understanding the dual role of the pions as the primary dynamic degree of freedom of the chiral dynamics and the most deeply bound state of quarks and antiquarks. For example, the chiral quark model [40] predicts that the pion sea carries a larger momentum fraction than the proton.

The main assumption of these analyses is that so-called "Sullivan" process [41] of scattering off the pion cloud dominates the process of neutron production. However, the current analyses have to include production of neutrons in a broad kinematic range where the dominance of the pion pole in the amplitude is questionable. Meson exchanges and absorptive effects must also be included. With increase of Q^2 other complications arise since the dominant part of the e – p cross-section at small *x* originates from photon-gluon fusion. In this case the scattering off the pion field is a small contribution [42]. Therefore, further studies need tighter kinematic ranges. It also would be interesting to study fraction functions for production of leading hyperons and investigate whether this information can be used to study kaon parton distributions.

2.4 Space - Time Correlations in QCD

Hard deep inelastic processes involve interactions with quarks and gluons at short distances, while at large distances we observe only hadrons. Therefore, different essential degrees of freedom are important at the different stages of the DIS process. QCD is a very successful theory for describing the numerous inclusive and semi-inclusive hard phenomena that are not sensitive to the long distance effects. In these processes space-time evolution of the system occurs over long space-time distances and is accounted for by the completeness of the final states. At the same time, the theory predicts remarkable phenomena arising from the long distance quantum structure of the interactions. These phenomena include color transparency, the remarkable behavior of parton energy loss in a nuclear medium, color opacity, and the nuclear medium effects on parton fragmentation. They are discussed below. Another phenomenon of this kind, nuclear shadowing, is discussed in Section 2.3.2.

These phenomena provide a unique opportunity to probe the space-time interplay between partonic and hadronic degrees of freedom in color confinement, and the role of color coherence in the space-time evolution of hard processes. The ability to reach high energies is critical since this provides significant simplification of the analysis. At high energies the space-time evolution of these processes slows down due to Lorentz dilation and occurs over large *longitudinal* distances when viewed in the rest system of the target. Therefore, to study the space-time structure of the strong interactions, researchers would like to have:

- A large enough *x*-range where weak coupling methods are applicable.
- Access to a wide range of nuclei and energies to study the nuclear and energy dependence of final states.

The Electron Ion Collider will provide these unique opportunities.

At the EIC nuclei can be used as super microvertex (femto) detectors to investigate the properties of quark-gluon systems, produced in various hard processes, by imbedding the hard process in the nucleus. The space-time picture of deep inelastic processes strongly depends on the value of Bjorken x. An analysis of the structure of the correlations of the electromagnetic currents in DIS reveals that one probes the target wave function at space-time points separated by longitudinal distances $l_{coh} = \frac{1}{2m_n x}$ and transverse distances of $\sim 1/Q$. At large enough x ($x \geq 0.2$) the virtual photon transforms into the strongly interacting state very close to the active nucleon, which, on average, is in the middle of the nucleus (Figure 2.12). The kinematics are optimal for studying the dynamics of partons produced in nuclear media. In this case, the key issues are the magnitude of the energy loss of propagating partons, its dependence on the distance traversed, and the concomitant broadening of their transverse momentum spectra.

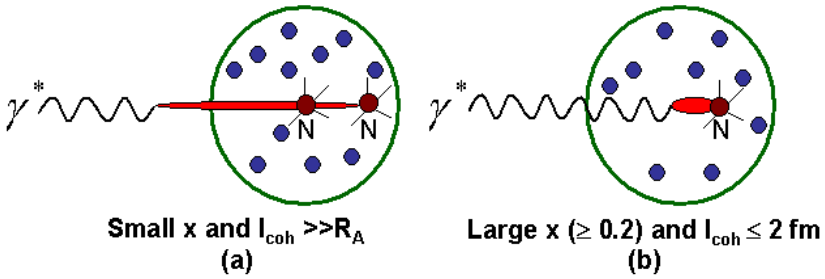

Figure 2.12: Coherence Length at Large and Small *x*.

(a) Schematic diagram of the probe formed outside the nucleus and at distances comparable to the nuclear size, and (b) inside the nucleus.

At smaller x (≤ 0.05) the longitudinal scale l_{coh} exceeds the nuclear size of the heaviest nuclei. At sufficiently small x (x < 0.005 for the heaviest nuclei) DIS processes go through several stages well separated in space.

- First, a virtual photon transforms into a quark-gluon wave packet well before the nucleus (at distances as large as one hundred fermi at the EIC).
- Next, the wave packet interacts coherently with the target over a relatively short period of time without changing its transverse size.
- Finally, over a longer interval, the fast component of the quark-gluon wave packet transforms into a hadronic final state when it is well past the nucleus. This interval could be as large as $2q_0/\mu^2$ where q_0 is the energy of the virtual photon and $\mu \leq 1$ GeV is a soft hadronic scale.

Currently, space-time studies are limited to semi-exclusive experiments that investigate the phenomenon of color transparency, and more generic inclusive studies of quark

propagation through nuclei. Both of these studies involve fixed targets and are summarized below.

2.4.1 Color Coherent Phenomena

The dynamics of the propagation of small color singlet objects through nuclear media is a fundamental question of QCD dynamics governed primarily by pQCD. Color screening of the interaction ensures that the cross-section with nucleons is small in a wide range of energies. Color singlet objects should interact weakly with a single nucleon of the target. Additional interactions are suppressed by powers of Q^2. This phenomenon is called "color transparency" since the nucleus appears transparent to the color singlet projectile [43,44]. Subsequently, it was suggested that the interaction of small color singlet projectiles with nuclei is large at very high energies. This phenomenon is "color opacity" [45,46].

Several studies of color transparency were performed at high energies and at small enough x where the initial quark-gluon system is formed before the nucleus. The earliest was a study of coherent J/ψ photoproduction off nuclei [47]. The amplitude of the process at small t (momentum transfer) is approximately proportional to the nuclear atomic number A. This indicates that the $c\bar{c}$ pair that passes through the nucleus is weakly absorbed. For hadronic projectiles, a similar and approximately linear A-dependence of the amplitude was observed recently for coherent diffraction of 500 GeV pions into two jets [48]. This is consistent with the predictions [45].

In pQCD, hard exclusive processes generated by longitudinally polarized photons are dominated by production of quark-antiquark pairs in a small transverse size configuration [46]. For transverse photons, a more gradual shrinking is expected. A number of papers [49,50,51] predict that the onset of color transparency at sufficiently large Q^2 will be observed for the production of vector mesons in the coherent diffractive process:

$$\left.\frac{d\sigma(\gamma^* + A \to V + A)}{dt}\right|_{t=0} \propto A^2 .$$

For incoherent diffraction at sufficiently large t (> 0.1 GeV^2):

$$R(Q^2) \equiv \frac{\dfrac{d\sigma(\gamma^* + A \to V + A')}{dt}}{\dfrac{A d\sigma(\gamma^* + N \to V + N)}{dt}} = 1 \cdot$$

The first measurements of the incoherent diffractive production of vector mesons were performed by the E665 collaboration at FNAL [52]. A significant increase of the nuclear transparency, as reflected in the ratio, $R(Q^2)$, was observed (Figure 2.13). The limited luminosity and center-of-mass energy do not provide a statistically convincing demonstration of color transparency. In addition, two effects complicate the interpretation of the data as an observation of color transparency. The first is a

correlation between Q^2 and the average x in the data sample. Larger Q^2 corresponds to larger x where a photon transforms more frequently into a hadronic state inside the nucleus and passes through a shorter distance of nuclear media. This results in larger values of R.

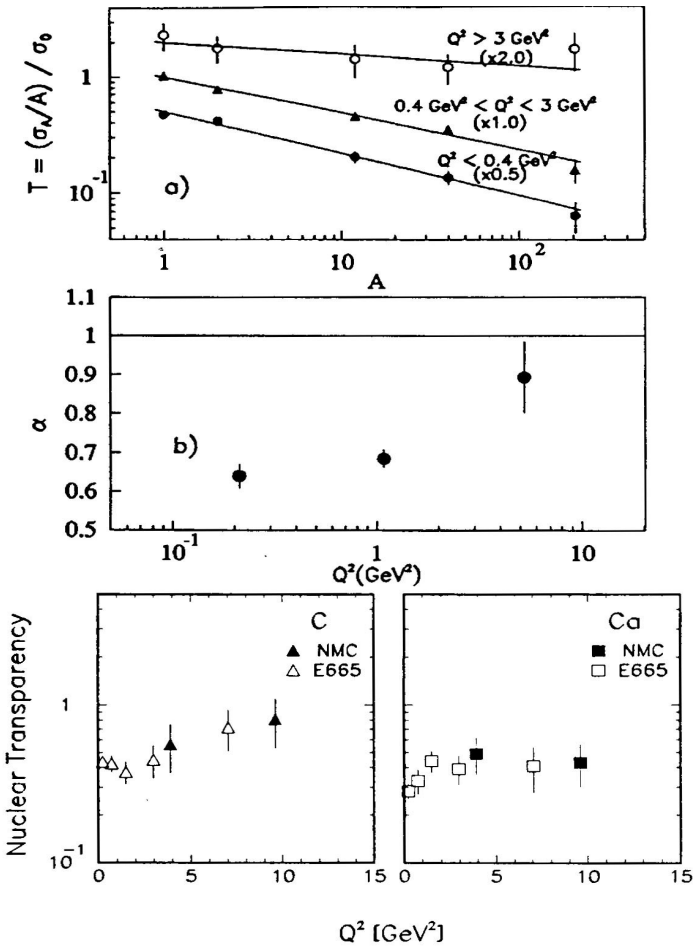

Figure 2.13: Possible Evidence for Color Transparency

The present evidence for color transparency showing both the Q^2 and A dependence of the relative yields of rho mesons produced on fixed nuclear targets using high-energy muons.

The value of R for the largest Q^2 (especially for heavy nuclei) is substantially larger than the increase of R due to the variation of x alone. The second complication is the problem with fixed target experiments. In fixed target experiments, hadron production cannot be excluded from the nuclear fragmentation region. The energy cuts of E665 allow a significant contribution to the observed cross-section of processes with hadron production. Currently, there are no theoretical predictions for the A-dependence of these inelastic contributions.

2.4.2 Parton Propagation Through Nuclear Media

Studies of the propagation of colored partons through nuclear media may provide insights into the many-body structure of QCD. The relevant questions are:

- Over what space-time intervals can pQCD describe the process?

- How does the formation time (or distance) of produced hadrons depend on their energy?

These questions have a strong connection to the dynamics of the nucleus-nucleus collision and are explored further in Section 3.2.3. Recent theoretical studies in this field focus on two limits:

- Propagation of partons through an extended nuclear media where multiple rescatterings provide a hard scale [53], and
- The limit of a thin target where only double scattering is possible [54].

Experimental studies of these phenomena performed at fixed target energies using lepton and hadron beams are inconclusive. Nevertheless, these studies established several interesting patterns, discussed below, which may be studied further with the Electron Ion Collider.

2.4.2.1 p_t Broadening of the Parton Spectrum

The QCD predication for transverse momentum broadening that results from multiple scattering is similar to that of ordinary multiple scattering. A parton from a projectile proton or virtual photon collides with various target nucleons exchanging transverse momentum ($\vec{p}_\perp$) at each collision before forming a Drell – Yan pair or a leading quark (in DIS). The expression in the case of quarks [53] is

$$<\vec{p}^{\,2}_\perp> = \frac{\alpha_s C_F \pi^2}{2}(xG)\rho L \approx 0.5\alpha_s\left(\frac{\mathrm{L}}{5\mathrm{fm}}\right)\ \mathrm{GeV}^2.$$

Here, C_F is the color Casimier of the quark, ρ is the nuclear matter density and L is the length of matter transversed. The Drell – Yan data [55] appear to agree with this expression and with the prediction for the small size of the effect (empirically, $\Delta<p^2_t>\approx$ 0.12 $(\mathrm{GeV/c})^2$ for heavy nuclei). The same experiment showed a very large difference in the A dependence of acquired transverse momentum of di-muons from the Drell-Yan process as compared to those from J/ψ and Υ production [56] and decay (Figure 2.14).

The existence of a difference is not surprising. Only an incident quark undergoes strong interactions in the Drell-Yan process, while the vector mesons formed by gluon fusion undergo strong interaction both on the incident gluon and on the resulting $c\bar{c}$ and $b\bar{b}$ pairs. However, it is difficult to explain the large difference, as much as a factor of 5. It also is noteworthy that J/ψ and Υ show the same effects, because the Υ is appreciably smaller than the J/ψ and should experience weaker interactions in the medium.

Another interesting observation [57] is that the p_t imbalance in the production of di-jets in nuclear photoproduction suggests a significantly larger p_t broadening effect. This mismatch may suggest non-universal behavior of the p_t broadening effects. Alternately, it may be due to a contamination of the jets in γ - A scattering by soft fragments. Parton

p_t broadening also may be responsible for the anomalous behavior of inclusive hadron production in hadron-nucleus scattering at high p_t. In this case, the ratio of inclusive hadron production in hadron-nucleus scattering to the same process on a nucleon, $A^{f(x,p_t)}$ shows an effective exponent, $f(x, p_t)$, exceeding 1 at $p_t \geq 1.5$ GeV. This is the "Cronin" effect [58].

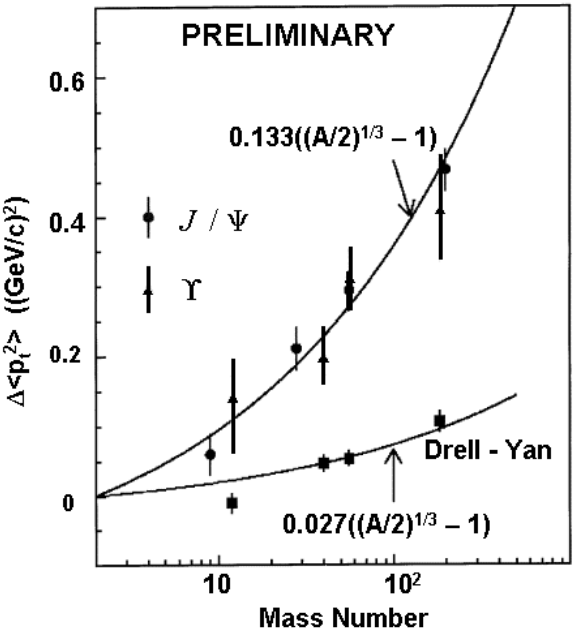

Figure 2.14: The A-Dependence for di-muon Pairs.

The A dependence of the measured $<p_t^2>$ *for di-muon pairs from Drell-Yan production, J/ψ and ϒ production using 800* GeV *protons on fixed targets.*

2.4.2.2 Energy Losses of the Leading Partons

Recent work on the energy loss of high-energy partons in a finite QCD medium, including cold nuclear matter suggests that the energy loss depends weakly on the energy, and may be quite small [53]. Further, the energy losses in hot matter should be much larger than in cold matter. This implies that jet quenching may be an excellent probe of the matter produced at early times in A - A collisions. Therefore, experimental studies of parton propagation effects in finite cold matter are important. Jet quenching in hot and cold nuclear matter is discussed further in Section 3.2.3.

Recent work shows that medium induced gluon radiation off a very energetic incident quark or gluon is independent of the initial jet energy, provided it is large enough in the rest frame of the medium ($E \geq 30$ GeV for quarks). For a quark jet, the medium induced energy loss increases *quadratically* with the length, L, and is independent of the energy for $E \to \infty$. For L = 5 fm, the asymptotic energy loss, ΔE, is estimated to be less than 1GeV in a cold nuclear medium. If true, this makes it difficult to empirically confirm this remarkable prediction for the L-dependence of the energy loss.

Deep inelastic scattering data are qualitatively consistent with small energy loss [59,60,61]. The data indicate that the multiplicity of the leading hadrons is moderately reduced (by ~10%) for virtual photon energies of the order of 10 – 20 GeV for scattering

off ^{14}N. At higher energies, the leading multiplicities gradually become A-dependent, indicating a weak absorption of the leading partons [60,61]. In this context, it is important to clarify the universality of quark and gluon nuclear fragmentation functions.

2.4.2.3 Hadron Formation Inside Nuclei

A fundamental question is whether some hadrons that are formed inside the nucleus subsequently reinteract with a hadronic strength. This is usually discussed in the framework of the formation length, l_{form}. One expects $l_{form} \approx \frac{E_h}{\mu^2}$ where E_h is the hadron energy and μ^2 is a soft scale that may be as large as 1 GeV^2 or as small as 0.1GeV^2. (The latter may in principle depend on h, x and Q^2). Therefore, hadrons with $E_h \le R_A \mu^2$ that are formed inside the nucleus can rescatter. Information about the overall interaction of the state initially produced in the DIS event with the residual nucleus is very limited because of a lack of good statistical data on the nuclear fragmentation region.

In the intermediate energy kinematics (for photon energies $\nu \le 20\,\text{GeV}$), where absorption/reinteractions of the leading quarks are observed, several experiments provide evidence of significant secondary interactions of the system produced with the nucleus [62]. The data is more ambiguous at the highest available fixed target energies. However, the data at these energies (E665), suggest that secondary interactions with the nuclei may be relatively small at high energies. The analysis [63] of the E665 data [64] on the rate of emission of soft neutrons from Lead (Pb) indicates that a very small fraction of the mesons produced in the collisions reinteract with the nucleus at $\nu \ge 100\,\text{GeV}$. This suggests that at high energies only very low energy mesons are formed inside the nucleus.

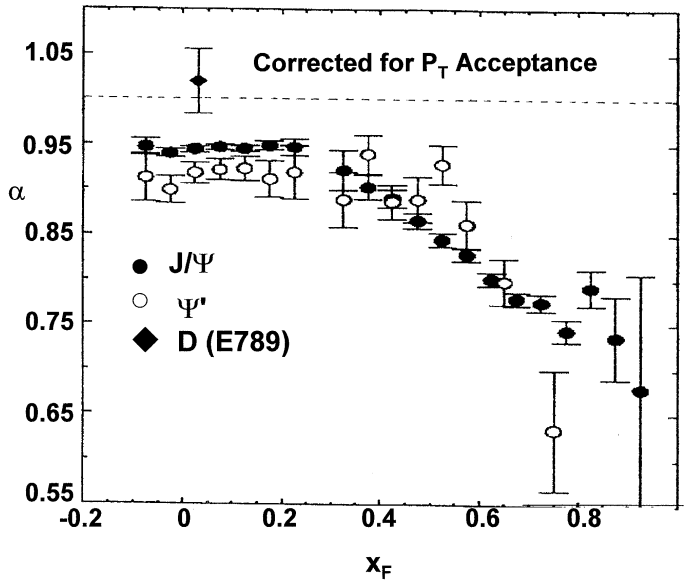

Figure 2.15: Characterization of the J/ψ and ψ'.

The x_F dependence of and A^α characterization of the J/ψ and ψ' yields from nuclear targets bombarded with 800 GeV *protons.*

A possible dependence of the space-time evolution on the properties of the produced hadron is illustrated by another example from the hadron-nucleus experiments. Figure 2.15 shows the dependence of the cross-sections observed in p - A reactions as a function of $x_F = x_1 - x_2$. At small or negative x_F the relative velocity of the $c\bar{c}$ system and the nucleus is small enough that the J/ψ and ψ' have sufficient time to form within the nuclear medium. The radius of ψ' is twice that of J/ψ so it is more readily absorbed, as reflected in the Figure 2.15. At larger x_F, the $c\bar{c}$ pair emerges from the nucleus before either state has the chance to form so that both display similar nuclear dependence. Therefore, the formation and coherence times are critical to understanding observed reaction yields.

2.5 References

1. Whitlow, L.M. et al., *Phys. Lett. B* 282, 475 (1992); Whitlow, L.M., SLAC preprint SLAC-357 (1990)
2. Arneodo, M. et al., New Muon Collaboration, *Nucl. Phys. B* 483, 3 (1997)
3. Aid, S. et al., H1 Collaboration, *Nucl. Phys*. *B* 470, 3 (1996); Adloff, C. et. al., *Nucl. Phys*. 497, 3 (1997)
4. Derrick, M. et al., ZEUS Collaboration, *Z. Phys*. *C* 69, 607 (1996); Derrick, M. et al., *Z. Phys*. *C* 72, 399 (1996)
5. ZEUS Collaboration, results presented at ICHEP-00, Osaka, Japan.
6. Martin, A.D., Roberts, R.G., Stirling, W.J. and Thorne, R.S., *Eur. Phys. J. C* 4, 463 (1998)
7. Lai, H.L. et al., *Eur. Phys. J, C* 12, 375 (2000)
8. ZEUS Collaboration, *Eur. Phys. J. C* 7, 609 (1999)
9. E155 Collaboration, *SLAC-PUB-7994*, July 2000 [hep-ph/0007248]
10. Adeva, B. et al., SMC Collaboration, *Phys. Rev. D* 58, 112002 (1998)
11. Ackerstaff, K. et al., HERMES Collaboration, *Phys. Lett. B* 464, 123 (1999); Airapetian, A. et al., *Phys. Rev. Lett*. 84, 2584 (2000)
12. Armaudruz, P. et al., New Muon Collaboration, *Phys. Rev. Lett*. 66 2712 (1991); Arneodo, M. et al., New Muon Collaboration, *Phys. Rev. D* 50, R1 (1994)
13. Hawker, E.A. et al., E866 Collaboration, *Phys. Rev. Lett*. 80, 3715 (1998)
14. Arneodo, M. et al., New Muon Collaboration, *Phys. Lett. B* 332, 195 (1994)
15. Kumano, S., *Phys. Rep*. 303, 183 (1998)
16. Speth, J. and. Thomas, A. W., *Adv. Nucl. Phys*. 24, 84 (1998)
17. Peng, J.C. and Garvey, G.T. in "Trends in Particle and Nuclear Physics", Volume 1, Plenum Press, New York (1999)
18. Eichten, E.J. et al., *Phys. Rev. D*, 2269 (1992)
19. Pobylitsa, P.V. et al., *Phys Rev. D,* 034024 (1999)
20. Aubert, J.J. et al., EMC Collaboration, *Phys. Lett*. *B* 123, 275 (1983)
21. Arnold, R.G., et al., *Phys. Rev. Lett.* 727 (1984)
22. Arneodo, M. et al., New Muon Collaboration, *Nuc. Phys*. *B* 441, 3, 12 (1995)
23. Adams, M.R. et al. E665 Collaboration, *Z. fur Phys*. *C* 67, 403 (1995)
24. Geesaman, D.F., Saito, K. and Thomas, A.W., *Ann. Rev. Nucl*. *Part. Sci*. 45, 337 (1995)
25. Friman, B.L., Pandharipande, V.R. and Wiringa, R.B., *Phys. Rev. Lett*. 51, 763 (1983)
26. Pandharipande, V. R. et al., *Phys. Rev. C* 49, 789 (1994)
27. Alde, D.M. et al., *Phys. Rev. Lett*. 51, 763 (1990)
28. Jackson, H.E., "17th International Conference on Few Body Systems", Taipei, 2000; Jackson, H.E., Spokesperson, JLab E91-003
29. Brown, G.E., Buballa, M., Li, Z. and Wambach, B., *J. Nucl. Phys. A* 593, 295 (1995) [arXiv:nucl-th/9410049]
30. Kolton, D.S., *Phys. Rev. C* 57, 1210 (1998)
31. Frankfurt, L.L., Strikman, M.I. and Liuti, S., *Phys. Rev. Lett*. 65, 1725 (1990)
32. Eskola, K.J., *Nucl. Phys. B* 400, 240 (1993)

33. Eskola, K.J., Kolhinen, V.J. and. Ruuskanen, P.V., *Nucl. Phys. B* 535, 351 (1998) [arXiv:hep-ph/9802350]
34. "Review of Particle Physics", *Eur. Phys. J. C* 15, 1 (2000)
35. Gousset, T. and Pirner, H. J., *Phys. Lett. B* 375, 349 (1996)
36. Frankfurt, L.L. and Strikman, M.I., *Phys. Rept*. 160, 235 (1988)
37. Collins, J.C., *Phys. Rev. D* 57, 3051 (1998) [Erratum-ibid, *D* 61, 019902 (1998)]
38. Grazzini, M., Trentadue, L. and Veneziano, G., *Nuc. Phys. B* 519, 394 (1998) [arXiv:hep-ph/9709452]
39. Badier, J. et al., NA3 Collaboration, *Z. Phys. C* 18, 281 (1983); Conway, J.S. et. al., *Phys. Rev. D* 39, 92 (1989)
40. Suzuki, K. and Weise, W., *Nucl. Phys A* 634, 141 (1998)
41. Sullivan, J.D., *Phys. Rev D*, 1732 (1972)
42. Frankfurt, L., Koepf, W. and Strikman, M.I., *Phys. Lett. B* 405, 367 (1997)
43. Brodsky, S.J., "Proceedings of the Thirteenth International Symposium on Multiparticle Dynamics", ed. Kittel, W., Metzger, W. and Stergiou, A. (World Scientific, Singapore, 1982) page 963
44. Mueller, A.H. "Proceedings of the Seventeenth Rencontre de Moriond, Moriond", 1982, ed. Tran Thanh Van, J. (Editions Frontieres, Gif-sur-Yvette, France, 1982) Vol. I, page 13
45. Frankfurt, L., Miller, G.A. and Strikman, M., *Phys. Lett. B* 304, 1 (1993)
46. Brodsky, S.J., Frankfurt, L., Gunion, J.F., Mueller, A.H. and Strikman, M., *Phys. Rev. D* 50, 3134 (1994)
47. Sokoloff M.D. et al., Fermilab Tagged Photon Spectrometer Collaboration, *Phys. Rev. Lett. 57,* 3003 (1986)
48. Aitala, E.M. et al., E791 Collaboration, *Phys. Rev. Lett.* 86, 4773 (2001) [arXiv:hep- ex/0010044]
49. Brodsky, S. J. and. Mueller, A. H., *Phys. Lett. B* 206, 685 (1988)
50. Frankfurt, L. L. and Strikman, M. I., *Phys. Rept*. 160, 235 (1988)
51. Kopeliovich, B.Z., Nemchick, J., Nikolaev, N.N., and Zakharov, B.G., *Phys. Lett. B* 309, 179 (1993) [arXiv:hep-ph/9305225]E
52. Adams M.R. et al., E665, *Phys. Rev. Lett*. 74, 1525 (1995)
53. Baier, R., Schiff, D., and. Zakharov, B.G., *Ann. Rev. Nucl. Part. Sci*. 50, 37 (2000) [arXiv:hep-ph/0002198]; Kopeliovich, B.Z., Tarasov, A.V. and Schafer, A., *Phys. Rev. C* 59, 1609 (1999)
54. Qiu, J.W. and Sterman, G., [arXiv:hep-ph/0111002]
55. McGaughey, P.L., Moss, J.M. and Peng, J.C., *Ann. Rev. Nucl. Part. Sci*. 49, 217 (1999) [arXiv:hep-ph/9905409]
56. Leitch, M.L., et al., E866 Collaboration, APS Long Beach Meeting, May, 2000
57. Naples, D. et al., E683 Collaboration, *Phys. Rev. Lett*. 72, 2341 (1994)
58. Cronin, J.W. et al., *Phys. Rev. Lett*. 31, 1426 (1973)
59. Airapetian A. et al., HERMES Collaboration, *Eur. Phys. J. C* 20, 479 (2001) [arXiv:hep-ex/0012049]
60. Adams M. R. et al., E665 Collaboration, *Phys. Rev. D* 50, 1836 (1994)
61. Ashman J. et al., European Muon Collaboration, *Z. Phys. C* 52, 1 (1991)
62. Burkot, W. et al., BEBC WA21/WA59 Collaborations, *Z. Phys. C* 70, 47 (1996) [arXiv:hep-ex/9612015]

63. Strikman, M., Tverskoii, M.G. and Zhalov, M.B., *Phys. Lett. B* 459, 37 (1999) [arXiv:nucl- th/9806099]
64. Adams M.R. et. al., E665 Collaboration, *Phys. Rev. Lett*. 74, 5198 (1995) [Erratum-ibid. 80, 2020 (1995)]

3.0 Scientific Opportunities with an Electron Ion Collider

In this section, the scientific vistas opened up by the EIC are described. The EIC will provide unprecedented data on hadronic structure by hard scattering of the virtual photon from the fundamental quarks and gluons of the nucleon and nuclear beams in the collider geometry with high luminosity and polarized beams of variable energies. In particular, the EIC will be able to detect particles over a wide range of rapidities. It will enable precision Deep Inelastic Scattering (DIS) measurements on nucleon and nuclear targets over $10^{-4} < x < 1$ and $1 < Q^2 < 10000$ $(\mathrm{GeV/c})^2$. The scientific impact of the EIC is clearly illustrated by considering a selected number of important scientific questions. We note that studies of both polarized electron – proton and unpolarized electron – ion DIS scattering at high energies, similar to the EIC, were done at DESY [1].

Parton Structure of the Unpolarized Nucleon: The nucleon's gluon structure can be determined unambiguously and with unprecedented accuracy using several independent techniques over $10^{-3} < x_{gluon} < 1$. Flavor separation can be achieved for valence quarks in a nucleon at large x by "tagging" the scattering off a neutron in electron-deuteron scattering, and for sea quarks, including strange and charm quarks, by studies of the final states. Unique tests of the range of applicability of perturbative QCD for inclusive scattering will be achieved because of the wide dynamic range of the EIC and the ability to measure longitudinal cross-sections by varying the energies of the electron and proton beams.

Spin Structure of the Nucleon: The spin-1/2 nucleon is built from quarks, gluons, and their interactions. A complete understanding of the spin structure of the nucleon in terms of QCD is extremely important. It is as essential to confirming QCD as understanding the spin structure of atoms was to QED. Several decades of principally inclusive experiments at SLAC, CERN, and DESY yielded determinations of the spin structure functions $g_1^p(x,Q^2)$ and $g_1^n(x,Q^2)$ over a limited range of x and Q^2. These data have allowed a test at the 5% level of the Bjorken Sum Rule [2], a fundamental relationship between the strong and electro-weak interactions that predates QCD. Further, the data provided a determination of the fraction of the proton spin carried by quarks ($25 \pm 10\%$) that is surprisingly low. Finally, NLO analysis of the world's data indicates, with large uncertainty that the gluon polarization is sizable and consistent in sign to make up the deficit due to the quarks. Recently, semi-inclusive measurements provided a flavor decomposition of the quark spin; the u quarks are positively polarized, the d quarks are negatively polarized, and the polarization of the antiquarks is consistent with zero.

The EIC will be the first facility to comprehensively address all aspects of the spin structure of the nucleon. Assuming that the principle of conservation of angular momentum holds, the spin-1/2 can be decomposed as

$$1/2 = 1/2\ \Delta\Sigma + \Delta G + \Delta L.$$

$\Delta\Sigma$ is the fraction of the nucleon spin carried by the quarks, ΔG is the contribution to the nucleon spin due to gluons, and ΔL is the contribution due to the orbital angular momentum of the quarks and gluons.

The EIC will dramatically increase the precision in determining g_1^p and g_1^n at low x. This will decrease significantly the uncertainties in the evaluation of the first moments of the spin structure functions and make it possible to determine the Bjorken Sum Rule at the level of 1%, provided instrumental uncertainties can be minimized. Further, the predicted, but as yet unobserved decrease of g_1^p at low x can be observed by the EIC in one week of data taking.

Within the next decade, direct information on the gluon polarization at high Q^2 will be obtained at RHIC-spin research from proton-proton scattering. In addition, HERMES and COMPASS using lepton beams will produce significant information in limited kinematics. Although the RHIC spin program will cover a broader range of Q^2 in measuring the gluon spin structure it obviously will not be able to employ leptoproduction, the most consistent determinant of gluon structure to date.

Generalized Parton Densities: The EIC will enable investigations of a new class of hard exclusive processes, calculable in QCD, where a photon or a meson is produced in the photon direction and a baryon is produced in the nucleon direction. Elucidation of these processes will lead to much more detailed information about longitudinal and transverse distributions of the partons in nucleons, including those that cannot be accessed in Deep Inelastic Scattering. In addition it will enable a comparison of parton distributions in different baryons. These inclusive studies also have a potential to determine the contribution to the nucleon spin from the orbital angular momentum, ΔL.

Role of Quarks and Gluons in Nuclei: The structure and properties of atomic nuclei are the basis for understanding many important aspects of the physical world, e.g. energy production, the origin of the elements, and the properties of the super-dense nuclear matter in the cores of neutron stars. Nuclear physicists have made great progress in explaining the fundamental characteristics of nuclei in terms of nucleons, and in modeling internucleon interactions through meson exchange and their interaction. However, the ultimate goal to completely understand microscopic nuclear structure in terms of the fundamental constituents of QCD, quarks and gluons, remains elusive, though the current DIS data reviewed in Section 2 strongly hint at the importance of quark and gluon degrees of freedom in nuclear microscopic structure. The EIC is proposed as a means to obtain definitive data and to realize this important goal.

Using DIS, researchers have determined that the momentum distribution of the quarks contained in a nucleus is measurably different from those in a free nucleon. However, almost no data exist on the gluon distribution in nuclei, though the NMC data suggest a significant enhancement of the gluon densities at x ~0.1– 0.2. The EIC will provide the conditions to determine nuclear modification of gluons in the range $10^{-3} < x_{\text{gluon}} < 1$ with high precision using several independent techniques. The EIC will enable separate

studies of nuclear effects for the sea and valence quarks, complementing tantalizing results from the Drell – Yan processes on the lack of nuclear enhancement of the sea.

A central issue with respect to nuclei is that of nuclear binding. What role do quarks and gluons play in this process? Studies of the A-dependence of different flavors as well as of gluons will clearly broaden our understanding. Studies of the parton structure of the off-mass-shell nucleons in the scattering off the deuteron and the lightest nuclei with a tagged spectator will make it possible to discriminate between different interpretations of the EMC effect. The unique collider geometry will allow selection of kinematics where scattering off a virtual meson may dominate. As a result quark and gluon distributions in the pion will be measured. This new and important information is essential to understand the role quarks and gluons play in binding the atomic nuclear system.

The EIC is also an essential tool in understanding the detailed characteristics of ultra-relativistic heavy ion collisions. The parton distributions in heavy nuclei are an essential input to any calculation of the processes taking place in these collisions and the EIC will determine these directly. Further, signatures for new phenomena e.g. the quark gluon plasma, typically involve propagation of jets or particles through nuclear matter. With the EIC, researchers will be able to observe clearly the signatures of known hard scattering processes in nuclei. These experiments will therefore provide the foundation necessary for understanding newly discovered phenomena.

Hadronization: In a hard scattering process, a colored quark or gluon constituent of a proton is struck with high momentum. However, because of the nature of QCD, this high energy colored parton will materialize in a detector as a system of color neutral particles, e.g. mesons. This process is termed hadronization. A basic but essentially unanswered question is: how do partons evolve into hadrons? Experiments to date have focused primarily on inclusive DIS, but to address this question measurements that determine the final state must be carried out. Special hadronization effects are expected for exclusive deep inelastic processes where a virtual photon converts into a forward going $q\bar{q}$ pair that for sufficiently large Q^2 is predicted to have a small transverse size. QCD predicts a new phenomenon in this situation, color transparency, a weak absorption due to color screening of the system while passing through nuclei where $x \geq 0.01$. For smaller x, QCD predicts an onset of another regime of perturbative color opacity, absorption of small $q\bar{q}$ systems caused by coherent interactions with several nucleons of the nucleus. The EIC, with its collider geometry and a suitably designed detector, will be able to reconstruct the complete final state in DIS from the proton, neutron and nuclear targets, and for the first time, the hadronization process will be extensively studied on the nucleon and nuclear targets in the complete kinematic range.

Search for new phenomena: At small x, several models predict that the gluon density will saturate, and subsequently grow only slowly. In particular, it is predicted that the saturated partons form a novel Color Glass Condensate (CGC). The colored partons in this state have remarkable properties analogous both to spin glasses and to the Bose-Einstein Condensates studied in condensed matter and atomic physics. Discovering the CGC and understanding its possibly universal properties would be a major advance in

our understanding of QCD at high energies. Observables that are sensitive to the gluon distributions in nuclei are the best way to search for the CGC. The EIC, with its high energies, unprecedented luminosity, collider geometry and, not least, its ability to vary the energy of both beams and the atomic number of the ions is the ideal machine for discovery of the CGC and for a detailed investigation of its properties.

The EIC's polarized, intense, colliding, high-energy beams will usher in an exciting, new era in the study of the fundamental structure of matter. By utilizing hard scattering process directly interpretable in terms of QCD, the EIC will provide the most precise information on the parton structure of nucleons and mesons. In conjunction with the anticipated advances in the ability to perform first principles calculations with QCD, the EIC will stringently probe the Standard Model of the strong interaction. Further, experiments using nuclear beams will provide definitive data on the role of quarks and gluons in the structure of atomic nuclei. These data are essential in the search for new phenomena. With its unmatched capabilities and a suite of optimally designed detectors, the EIC will be a forefront facility in the study of the fundamental structure of matter for at least a decade.

3.1 Exploring Nucleons

The high luminosity of the EIC provides a wide range of opportunities for experiments of polarized and unpolarized Deep Inelastic Scattering. In this section we discuss opportunities to better determine the properties of the nucleon.

3.1.1 Unpolarized Parton Distribution Functions

Deep inelastic lepton-proton/deuteron scattering studies performed over the last two decades, both in a fixed target mode and in a collider mode have not answered many fundamental questions ***quantitatively***. This situation will not improve in the near future since there will be no new facilities or experiments with the necessary kinematic range. There are several reasons why the EIC will enable quantitative studies of processes in electron-proton/deuteron collisions:

- High luminosity.
- The ability to vary both the energy of the electron and the nucleon beams.
- The ability to polarize both nucleon and electron beams.
- The ability to compare interactions with protons and neutrons by tagging spectator nucleons in electron – deuteron interactions.
- The potential for a broader angular coverage including nucleon and current fragmentation regions.
- The ability to deal more effectively with electromagnetic radiative corrections by detection of hadrons and photons in the final state.

While all of these may be done in the future at HERA, they would require a significant modification and upgrade of the current accelerator and detector facilities.

Some of the discussion that follows involves educated conjectures. The discussions are intended to guide a quantitative modeling of current and future accelerator and detector proposals (See sections 4 and 5). However, if these conjectures are confirmed, the EIC in the electron-nucleon mode will be a *high resolution, high precision probe of hadron structure and provide a means of investigating the space-time picture of confinement.*

3.1.1.1 Inclusive Measurements: F_2^p, σ_L

Despite many years of DIS measurements, our knowledge of nucleon parton densities is incomplete. Consider for example inclusive measurements such as F_2^p, σ_L. Previous experiments determined F_2^p with a good accuracy and $\frac{\partial F_2^p}{\partial \ln Q^2}$ with reasonable accuracy. The data are well fitted by LO or NLO DGLAP evolution equations. However this involves free fitting parameters: the coupling constant of strong interaction, $\alpha_s(Q^2)$ at the normalization point for large *x* and the gluon density at $x \le 0.15$. In addition, the fits make assumptions about the absence of higher twist effects for $x \le 0.2$. The situation is complicated further because experiments measure the differential cross-section, which under the experimental conditions is approximated by the sum of the transverse and longitudinal photon cross-sections: σ_T and σ_L. Since σ_L cannot be measured directly, an uncertainty is introduced in the extraction of the structure functions. This leads to a very large uncertainty in the gluon density in nucleons in a broad range of *x* for $Q^2 \le 2\ \text{GeV}^2$. The fact that LO and NLO fits of the data are comparable in quality illustrates this problem.

The EIC will provide large counting rates for a very large range in $ln\ Q^2$ for $x \le 0.3$. In addition, the EIC will be able to vary both the energy of the electron beam and the proton energy. Therefore, it will be possible to do the following either significantly better or for the first time;

- Measure σ_L with a number of cross checks, and
- Measure the curvature of the scaling violation $\frac{\partial F_2^p}{\partial \ln Q^2}$.

These two measurements combined would provide a stringent test of the regime of applicability of pQCD, and measure the gluon density, with a good precision in a wider range of Q^2 and *x*. These measurements have the potential to distinguish between gluon distributions in protons, and in nuclei where non-linear effects are enhanced. In addition, they will help isolate the contribution of higher twist effects in nucleons.

3.1.1.2 Flavor Dependence of Parton Distribution

Our current understanding of flavor dependence of the parton densities is very limited. This includes both the separation of sea and valence quarks, and flavor dependence of the sea. The fundamental questions, which have to be addressed, are related to the interplay of perturbative (gluon fusion type) and nonperturbative contributions to the sea, the underlying nonperturbative dynamics responsible for $\bar{u} - \bar{d}$ asymmetry and suppression of the strange sea.

Our knowledge of the non-vacuum channel is good but incomplete. In particular, the scaling violation for $x \leq 0.2$ is measured only in neutrino scattering (F_3) using nuclear targets. It is not clear whether the Regge type behavior holds for the non-vacuum channel for $x \to 0$ and $Q^2 =$ constant. Use of deuteron beams and spectator tagging will enable measurement of $F_2^p - F_2^n$ and perhaps $\sigma_L(p) - \sigma_L(n)$ with a high degree of accuracy. This would provide a very clean test of the NLO DGLAP equations, a highly precise measurement of the running $\alpha_s(Q^2)$, and may reveal higher twist effects that were not accessible because of the insufficient accuracy of the current data.

The measurement of the difference of the cross-sections of the leading π^+ and π^- production, in combination with studies of the final states, will allow separation of the sea and valence quark contributions to F_2 and σ_L.

The flavor dependence of the sea is still a mystery. The only positive knowledge we have comes from the FNAL Drell - Yan experiment that established a large $\bar{u} - \bar{d}$ asymmetry. The HERMES experiment did confirm this observation by a study of final states but clearly better statistics and large Q^2 range are needed. This and related studies with polarized beams will provide important insights into the interplay of various chiral aspects of the nucleon wave function. This topic is hotly debated in the literature; different chiral models predict qualitatively different patterns for the polarization effects and for the final states.

Charm Sea: With the EIC it will be possible to measure charm production over a wide range of Q^2. There is a large rapidity interval between the leading charmed hadron and the second charmed hadron in nonperturbative models of charm [3]. These models predict the associated production of charm in the target and current fragmentation regions. In contrast, the perturbative fusion mechanism predicts the production of both charmed hadrons in the current fragmentation region. Study of the Q^2 dependence of the charm production will allow independent measurements of the gluon parton distributions down to $x \leq 0.1$.

Strange Sea: High precision measurements of the leading kaon production in the current fragmentation region, especially K_S, K^-, will facilitate measurement of s and $\bar{s}$ as well as the separation of nonperturbative and perturbative contributions by a study of the

correlation between the production of strangeness in the current and target fragmentation regions.

3.1.1.3 Tagging Of Scattering from Neutrons in Electron Deuteron Scattering

3.1.1.3.1 Measurement of F_2^n for Large x

Accurate information on the behavior of the parton densities in the extreme kinematic limit of $x \to 1$ would enhance our understanding of the nucleon's partonic structure [4]. The d/u ratio is especially interesting since its deviation from ½ provides a sensitive measure of the pattern of breaking of the SU(6) symmetry.

Consider the high $x \to 1$ behavior of $\frac{F_2^n}{F_2^p}$:

- In a world of exact spin-flavor SU(6) symmetry

$$\frac{F_2^n}{F_2^p} = \frac{2}{3}.$$

- In nature SU(6) symmetry is broken. The nucleon and Δ masses are split by about 300 MeV. Further, from DIS we know that the d quark distribution is softer than the u quark distribution. Based on phenomenological arguments [5,6,7] symmetry breaking was thought to arise from a suppression of the "diquark" configuration, S=1, relative to those of S = 0. Therefore, a dominant scalar valence diquark component of the proton suggests that in the $x \to 1$ limit, the cross-section is essentially given by a single quark distribution (i.e. the u), in which case:

$$\frac{F_2^n}{F_2^p} \to \frac{1}{4}, \quad \frac{d}{u} \to 0 \quad [S = 0 \text{ dominance}].$$

  This expectation has, in fact, been built into most phenomenological fits to the parton distribution data [8].

- An alternative approach, based on pQCD [9], predicts that the relevant component of the proton valence wave function at large x is that associated with states in which the total "diquark" spin projection, S_z, is zero: (qq) S_z=0 (qq) S_z=1, $x \to 1$. In this picture as $x \to 1$, one predicts:

$$\frac{F_2^n}{F_2^p} \to \frac{3}{7}, \quad \frac{d}{u} \to \frac{1}{5} \quad [S_z = 0 \text{ dominance}].$$

Note that the d/u ratio *does not vanish* in this model.

Since F_x^n is significantly smaller than F_x^p at large x, its extraction is sensitive to nuclear effects and in particular the EMC effect that is expected in all nuclei. Two analyses tried

to correct for the possible EMC effect in the deuteron [10,11]. One used the estimate of the EMC effect in the deuteron from [12]; the other used a model of the EMC effect based on the description of the deuteron with one on-mass-shell and one off-mass-shell nucleon. Both analyses indicate that the d/u ratio may be much closer to the pQCD prediction than previously thought based on the analysis that modeled the deuteron neglecting the EMC effect. Clearly measurements free of nuclear effects need to be performed.

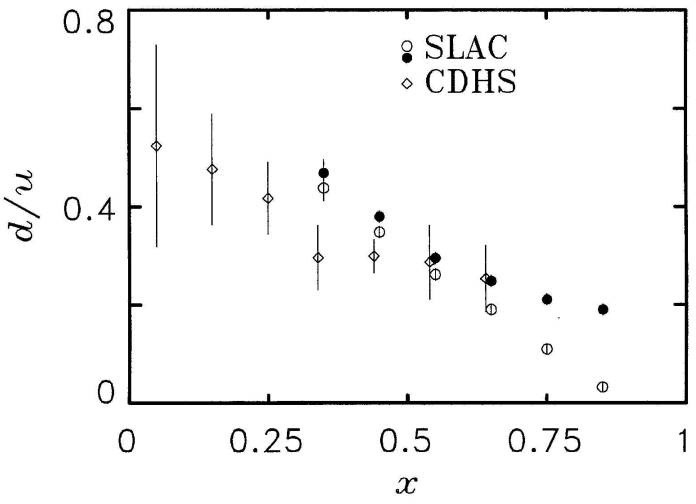

Figure 3.1: d/u Ratio Using Off-Shell Deuteron Calculations and On-Shell Kinematics

d/u ratio [13,14] extracted from SLAC data using two different methods: the model from reference [4] (full circles), and the original SLAC procedure (open circles). Also shown for comparison is the ratio extracted from neutrino measurements by the CDHS collaboration [15].

A completely new technique to determine the neutron structure function at large x will be possible with the EIC. Nuclear effects in the deuteron structure function originate from the situation where two nucleons come close enough to each other and have significant relative momenta. Selection of processes where the spectator proton carries momentum that is close to zero in the deuteron rest frame, or equivalently carries a fraction of the deuteron momentum close to one half and a small transverse momentum in the EIC frame, creates a situation where the distance between the nucleons in the initial state is $\geq$4fm and the neutron is essentially free. Kinematics of the DIS scattering for $x > 0.1$ leads to a negligible contribution to the cross-section of processes where the spectator originates from the elementary e - N scattering [16].

For example, by scattering a 5 GeV electron from a 50 GeV/c deuteron and detecting the spectator proton, F_2^n (x), can be determined cleanly at high x. By measuring F_2^n (x) as a function of the momentum of the recoiling proton, the dependence on the off-shell nature of the nucleon can be eliminated by performing a Chew-Low type extrapolation to the nucleon pole. It is estimated that a ±3% measurement of $\frac{F_2^n}{F_2^p}$ at x = 0.8 should be possible with the EIC in one year of data acquisition. This technique can also be employed to determine g_1^n at high x.

3.1.1.3.2 Measurement of F_2^n for Small x

Measuring the difference $F_2^p - F_2^n$ for small x is a unique way to investigate the small x dynamics in the non-vacuum channel. The extraction of this difference from the comparison of inclusive e - d and e - p scattering is strongly model dependent for $x \leq 0.02$ where the difference $F_2^p - F_2^n$ becomes comparable to the nuclear shadowing correction, $\Delta\sigma \equiv F_2^d - F_2^p - F_2^n$, that is estimated to be of the order of 2-3% of F_2^d. Tagging the scattering off neutrons is more difficult in this case because of the contribution of the diffractive processes that do not shift appreciably the longitudinal momentum of the nucleon. It will be possible to improve greatly the measurements of $F_2^p - F_2^n$ at small x by studying the transverse momentum distribution of the nucleons and simultaneously measuring the processes $e + d \rightarrow e + p + X$ and $e + d \rightarrow e + n + X$ with protons and neutrons in the spectator kinematics, and by using information on the final state (diffractive versus non-diffractive).

3.1.2 Polarized Parton Distributions

Since RHIC can provide different species of hadrons for collision and since the electron and hadron beams of the EIC will be polarized, the EIC will be a powerful tool for exploring the spin properties of nucleonic matter. This section describes some of the important opportunities that would be afforded by the EIC.

3.1.2.1 Polarized Structure Function $g_1(x,Q^2)$ of the Nucleon

Measuring the polarized structure function, $g_1(x,Q^2)$, of the proton and neutron using either deuteron or ^{3}He beams would be one of the unique sets of measurements possible with the EIC. The spin structure function at low x is interesting not only because of its relevance to the spin sum rules, but also because the pQCD analyses at NLO made very dramatic predictions for the low x behavior of the structure functions. These low x predictions, based on the fits to existing data, indicate that below the present lowest measured x value (0.003), g_1^p and g_1^n become large and negative. The physical origin of this dramatic decrease is thought to be due to the large and positive polarized gluon distribution at relatively larger values of x.

Figure 3.2 shows the dramatic behavior predicted from pQCD analysis of the spin structure functions as a function of x for different values of Q^2 (2,10,100 GeV^2) [17]. The projected EIC statistical uncertainties correspond to 400 pb^{-1} luminosity for e - p scattering with an almost 4π acceptance detector such as ZEUS or H1 in HERA at DESY. Clearly, the measurements possible with the EIC will easily distinguish between the QCD calculations at different scales and establish the pQCD evolution of the spin structure function and the parton distribution in this kinematic region. Note that the luminosity used to estimate the statistical uncertainty, 400 pb^{-1} is rather small for the EIC, which is

expected to provide 85 pb^{-1}/day at full luminosity. In a typical EIC run of one year one can expect ten times the statistical significance shown in Figure 3.2.

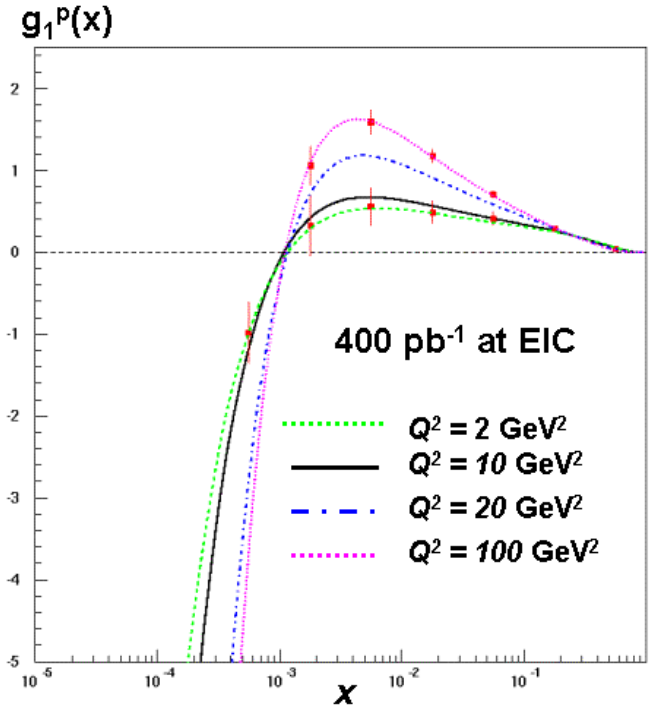

Figure 3.2: Statistical Accuracy of g_1^p (x) Measured as a Function of *x*

This figure shows the statistical accuracy with 400 pb^{-1} *luminosity with the EIC (~ 1 week of data) assuming* 250 GeV *polarized protons and* 10 GeV *polarized electrons. The curves are the best fit to the world's data set evaluated at different* Q^2.

The neutron spin structure function [17] could be measured by circulating polarized deuterons (p + n) or doubly charged helium (2p + n) in the EIC, resulting in e - d and e - He collisions. If the hadronic proton fragments are tagged, an exclusive measurement of the spin structure function of the neutron can be performed. This would allow a very accurate measurement of the spin structure function g_1^n for the first time below a few times 10^{-3}. The variation of the spin structure function of the neutron will be very different from the proton case since at very small *x*, g_1^p and g_1^n should be approximately equal, while in the currently available kinematic regime $g_1^p \approx -g_1^n$. An accurate measurement would be an essential test of pQCD at low *x*. Tagging also will improve dramatically the accuracy of measurements of g_1^n for the entire range of *x* available with the EIC.

Combined data on $g_1^n(x)$ and $g_1^p(x)$ will provide a precise test of the Bjorken sum rule. It is estimated that accuracy of the order of 1% [18] could be expected for such measurement in a rather short running time (~ 1 month of running). The present uncertainty (~5%) associated with the Bjorken sum rule is dominated by the lack of data at low *x*, even after 30 years of experiments.

3.1.2.2 Polarized Gluon Distribution $\Delta G(x,Q^2)$

The polarized gluon distribution, $\Delta G(x,Q^2)$, appears at NLO in the pQCD analysis of the spin structure function. To determine this function experimentally, one needs to analyze the world's available data, assuming certain initial conditions for the polarized parton distributions, and then fit them to the data using the DGLAP evolution equations and the pQCD coefficient and splitting functions evaluated at NLO. The results of these analyses are a set of parton distribution functions, particularly the gluon polarization distribution function, $\Delta G(x,Q^2)$, and its first moment. Figure 2.4 shows the present knowledge of these parton distribution functions. The first moment determined in one analysis [19] is:

$$\Delta G(Q^2 = 1GeV^2) = 1.0^{+1.2+0.4+1.4}_{-0.3-0.2-0.5}$$

The first uncertainties are statistical, the second are systematic experimental uncertainties and the last are uncertainties in the theoretical sources/inputs (e.g., the assumption of the functional form of the parton distribution function at the initial scale, the value of the strong interaction coupling constant $\alpha_S(Q^2)$, the higher order unaccounted corrections). The dominant uncertainties arise from the unmeasured low *x* region. These uncertainties can be reduced by at least a factor of 3 to 5 with data from the EIC at the projected luminosity [17].

3.1.2.2.1 Polarized Gluon Distribution from Photon Gluon Fusion Process

The other ways to determine the polarized gluon distribution involve semi-inclusive and inclusive measurement of processes where the gluon appears at leading order. The process that is most powerful in measuring the gluon polarization is Photon-Gluon-Fusion (PGF). The Feynman diagram for such a process is shown in Figure 3.3 (a). The two quark lines in the final state may materialize as quark-jets if the interaction occurs at high enough energies (Di-Jet Analysis), or the jets may hadronize which can be observed as oppositely charged leading hadrons (High p_t Hadron Track Analysis). The fundamental physics at the vertex is the same in each case. The experimental background in Photon Gluon Fusion measurements is shown in Figure 3.3 (b). This is called the QCD - Compton (QCD-C) diagram.

Figure 3.3: Photon Gluon Fusion Process and QCD-Compton Process

Photon Gluon Fusion process (a) is the principal means for accessing the polarized gluon distribution in the nucleon. The QCD - Compton process (b) that contributes as background.

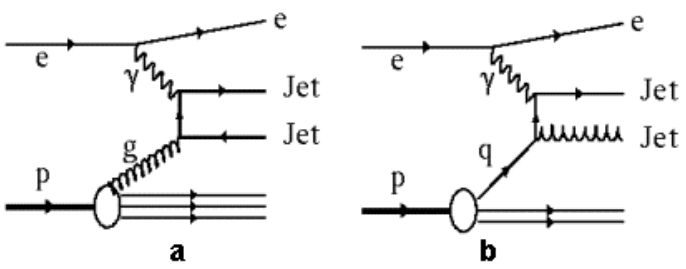

This background can be reduced to less than 10% [20], by choosing the kinematics of the events appropriately. It is estimated that the data obtained at the EIC for about a week of running, can determine the first moment of the polarized gluon distribution and it could be measured with an accuracy of (+/- 0.3) See Figure 3.4. This method of determining the polarized gluon distribution function does not include assumptions about the functional form of the parton distribution function, as is the case for the NLO pQCD. Therefore, the shape of the gluon distribution function is highly constrained.

Similar results were obtained for High-p_t Hadron Track analysis, as used by HERMES [21]. One advantage of having two analyses is that they use different detection components in a collider detector [22]. As such, the same quantity ΔG would be accessed with mutually exclusive detector systems. It was noted in a similar study presented at a polarized HERA workshop that about 60% of the events detected in the Di-Jet analysis also showed up in the High-p_t Hadron Track analysis. Thus, a "common" dataset can be analyzed in both ways, providing an important crosscheck for understanding the uncertainties in different experimental systems.

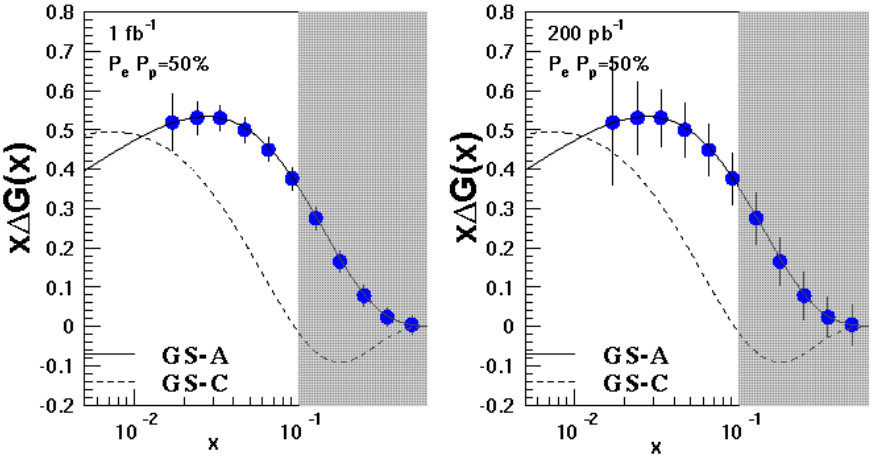

Figure 3.4: Asymmetry Analysis Based on Photon Gluon Fusion Method

Figures (a) and (b) show the result of analysis based on Photon Gluon Fusion method. Clearly the projected EIC statistical uncertainties for 1 fb^{-1} *and* 200 pb^{-1} *would easily distinguish between two different published polarized gluon distributions (GS-A and GS-C) both consistent with existing data. This study was performed using the acceptance of the H1 detector at HERA and the NLO calculations recently made available for the PGF and QCD-C processes. The shaded area in the figures shows regions where the QCD-C background is expected to be large.*

3.1.2.2.2 Combined Analysis of $g_1(x,Q^2)$ and Di-Jet Events

Since pQCD analysis of $g_1(x)$ and the Di-Jet asymmetries probe the same gluon distributions, if a combined analysis of the two is performed, it is expected that the gluon distribution could be determined with smaller uncertainties. This type of analysis was

carried out in detail for polarized HERA studies [23] and shows that such a global analysis does indeed reduce the uncertainties in the gluon distribution. A similar preliminary analysis for the EIC [15] indicates that the effect of combined analyses reduces the uncertainty of the polarized gluon distribution by about a factor of 3.

3.1.2.2.3 Photoproduction

In the photoproduction limit, i.e. in the region where the intermediate photon virtuality is small, the e - p cross-section can be approximated as a product of a photon flux and an interaction cross section of the real photon with the proton. Measurements at HERA in this photoproduction limit led to significant improvement in our knowledge of the structure of the photon and the proton, and a better understanding of the transition from a virtual to a real photon. At the Yale-EIC workshop many of these issues were explored assuming high-energy EIC polarized proton and electron beams. Only the most attractive and unique topics are discussed below. Other interesting topics such as open charm production, Drell-Yan processes, large p_t photon and inelastic J/ψ production have been considered for polarized HERA studies [24]. The high luminosity at the EIC would provide for substantially better measurements over those possible at HERA.

A detailed study was performed [25] of the physics with 1-2 jets or High-p_t Tracks originating from Photon Gluon Fusion diagrams. It shows that this would be a significant probe of the polarized gluon distribution, and would be sensitive to the polarized parton distributions inside the photon, Δq^{γ}.

Figures 3.5 (a) and (b) show the projected statistical uncertainty achievable with 1 fb^{-1} data at the EIC for a single and double jet asymmetry plotted against the pseudorapidity, η_{LAB} , and transverse momentum square, p_t^2, respectively. The statistical errors for the EIC luminosity are very small. The different theoretical curves in Figure 3.5 (a) (upper curves) originate from different assumptions about the gluon distributions; indicating that the data will distinguish between different polarized gluon distributions. The difference between the upper curves and lower curves in Figure 3.5 (a) is due to the different assumptions about the structure of the polarized photon. Clearly, with the statistical accuracy shown in the figure these can be resolved easily.

Figure 3.5 (b) shows the asymmetries in Di-Jet photoproduction assuming maximal, minimal and fitted photon parton distributions. This uses un-polarized data from HERA. A polarized EIC with this luminosity could easily determine the structure of the polarized photon. Note that even with the inefficiencies of a detector and the machine (~30% each), the necessary measurement accuracy could be achieved in less than one month with the EIC. The measurements of the photon structure function would be unique, as well as fundamental and groundbreaking, without competition for a long time to come. The only comparable measurements of any significance would be made at a gamma-gamma collider now under consideration for construction towards the end of the next decade.

Figure 3.5: Projected Statistical Uncertainty at the EIC for Single and Double Jet Asymmetry

Figure (*a)is the single jet production asymmetry* $A^{1\text{-}jet}$ *vs.* η_{LAB}. *A calculation shown along with statistical accuracies expected with* 1 fb^{-1} *data from the EIC Figure (b) is the di-jet production asymmetry* $A^{2\text{-}jet}$ *as a function of* log_{10} (p_t^2) *shown with the statistical uncertainty expected in this measurement at the EIC. Theory curves are explained in [23].*

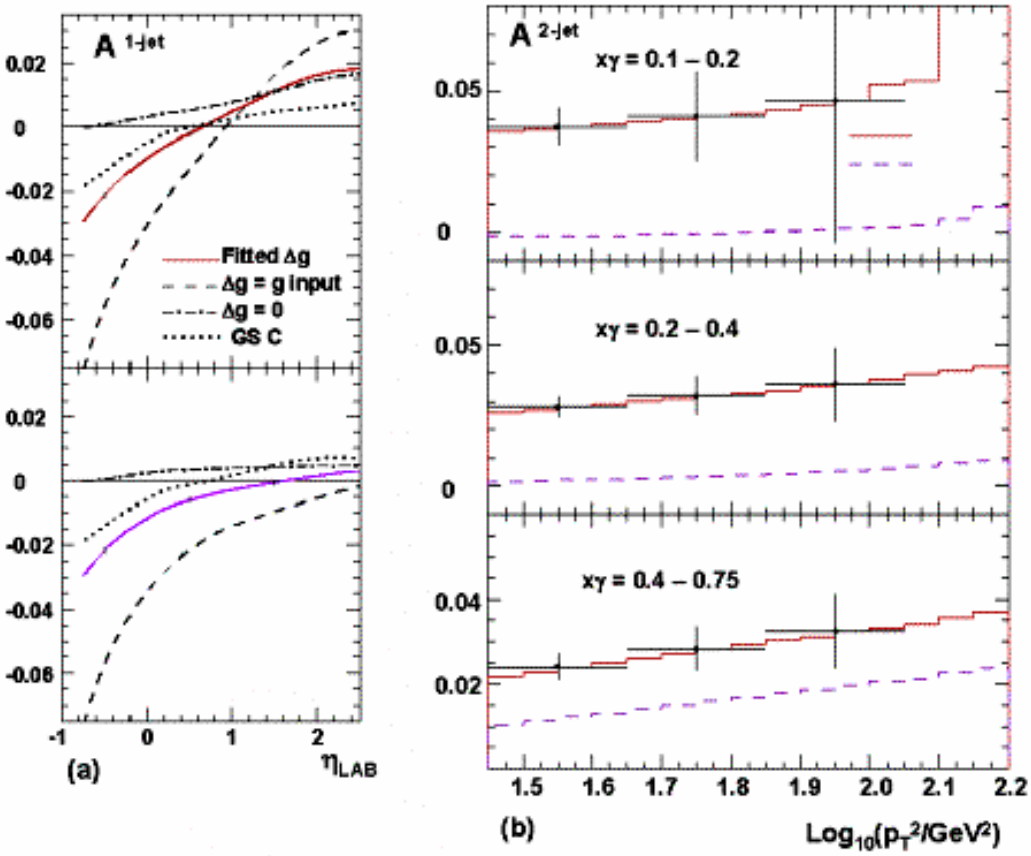

3.1.2.3 Photoproduction and Drell-Hern-Gerasimov Spin Sum Rule

The H1 and ZEUS detectors at DESY routinely take data using "electron taggers" situated in the beam pipe 6 - 44 meters away from the end of the detectors. They detect the scattered electrons from events having very low Q^2 and scattering angles. If electron taggers were included in the EIC, similar measurements could be performed. The Q^2 range of such measurements at the EIC is estimated to be 10^{-8} – 10^{-2} GeV^2, in the center-of-mass region of 30-70 GeV. These measurements would be directly relevant to the Drell-Hearn-Gerasimov (DHG) spin sum rule, which relates the real photon-proton cross sections when the photon and proton are aligned and anti-aligned:

$$\int_{\nu-th}^{inf} \frac{d\nu}{\nu}(\sigma_{\uparrow\downarrow}^{\gamma p} - \sigma_{\uparrow\uparrow}^{\gamma p}) = -\frac{4\pi^2\alpha\kappa^2}{2m^2{}_p}.$$

In this expression κ is the magnetic moment of the proton and α is the electromagnetic fine structure constant, or coupling constant. This measurement can be made in the ν range of 600 GeV to few TeV. Although the contribution to the DHG sum rule from this region is small, the information from the EIC would be valuable. All other experimental measurements are performed in the ν range of 10-20 GeV. It is necessary to extrapolate to high ν to obtain the complete integral, and to do this it is necessary to assume a certain shape of the cross-section coming from the Regge type of behavior in this region. No other accelerator facility will be able to check this experimentally. It would be an important input for other measurements, presently underway around the world, to acquire these data points and constrain the extrapolations that are now based on unverifiable assumptions.

3.1.2.4 Flavor Decomposition of Quark Spin Structure

Significant insights into the nucleon's spin and flavor structure can be gained by using semi-inclusive scattering in which hadrons produced in a photon-quark reaction are detected in coincidence with the scattered lepton. Knowledge of the identity of these hadrons and their kinematic correlation with the momentum and energy of the virtual photon will allow separation of the contributions from the different quark flavors involved in the scattering event. In combination with polarized targets and beams, the spin contribution of the individual flavors can be determined as well. The spin contribution of the strange quarks is especially important; their role in nucleon structure is one of the most ill understood aspects of the nucleon spin.

In fixed target experiments, Lorentz boost of the beam produces the so-called current hadrons at forward angles in the laboratory frame. This region is difficult to instrument adequately, especially since the luminosity is increased to gain significant statistical accuracy. In addition, almost all of the fragments of the target nucleon are lost at small energies and large angles. Correlation of these target fragments with the hadrons directly produced would enhance the power of the semi-inclusive technique.

A polarized ion-electron collider has the ideal geometry to overcome the shortfalls of the fixed target experiment for semi-inclusive studies. The collider kinematics open up the final state into a large solid angle in the laboratory, which, using an appropriately designed detector, would allow complete identification of the hadronic final state both in the current and target kinematic regions of fragmentation phase space. At the EIC energies the current and target kinematics are well separated thereby greatly improving the reliability of the application of the factorization theorem to the fragmentation processes.

Figure 3.6 shows estimates of the precision with which one could measure quark spin distributions at the EIC. The plotted uncertainties are statistical only. The simulation was based on an integrated luminosity of 1 fb^{-1} for 5 GeV electrons on 50 GeV protons with both beams polarized to 70%. The simulated events were produced using the DIS generator LEPTO [26], and the hadronization performed using the LUND string model at

Leading Order in pQCD. Inclusive and semi-inclusive asymmetries were analyzed using the purity method developed by the SMC [27] and HERMES [28] collaborations. Further details are given in [29].

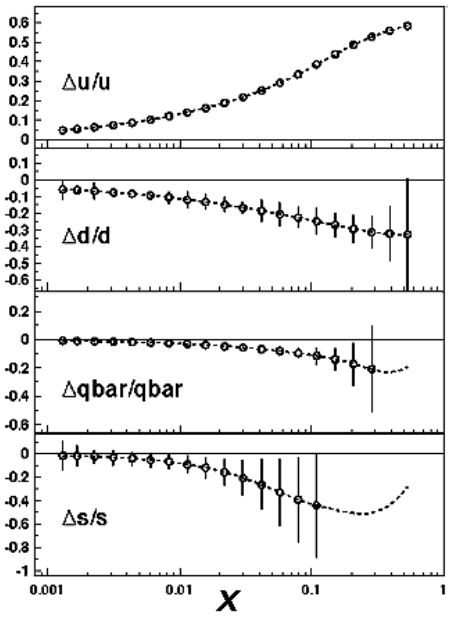

Figure 3.6: Projected Precision of the EIC for Measuring Quark Spin Distributions

It is clear that excellent precision for)q/q can be obtained down to $x = 0.001$. With proton beams (targets), one obtains greater precision for up quarks than down quarks. Excellent precision for down quark spins could be obtained by using deuteron or helium beams.

The expected statistical precision of quark polarizations for up, down, the light anti-quarks and strange quarks, using polarized [30] and unpolarized [31] parton distribution functions are shown in Figure 3.7. Here the four charged pion and kaon asymmetries were chosen as input. The measured average Q^2 values per x bin are not shown but are in the range of ~1.1 GeV^2 at lowest x to ~ 40GeV^2 at highest x.

As discussed in Section 2 a recent result showed that $\bar{u}$ and $\bar{d}$ distributions differ strongly for $0.05 < x < 0.2$ and several dynamic mechanisms were suggested as an explanation of this non-perturbative effect. The measurement of spin dependence of the sea may provide a key test. In the models where the sea originates from the scattering off pions, $\bar{u}$ and $\bar{d}$ are practically unpolarized, with some equal polarization generated at large Q^2 from the polarized gluons. Expectations of the chiral soliton model [32], which was derived "microscopically"' within the instanton model of the QCD vacuum and provides a dynamic explanation of the spontaneous breaking of the chiral symmetry, and a good description of $\bar{u} - \bar{d}$ data are qualitatively different. In this model, in the limit of a large number of colors (N_c), $\Delta\bar{u} - \Delta\bar{d} \sim N_c(\bar{u} - \bar{d})$. Therefore, a larger asymmetry is predicted in the polarized case than the one observed for the unpolarized case. (See Figure 2.7)

Figure 3.7: Statistical Precision of the Quark Polarization

Top: Statistical accuracy of the semi-inclusive asymmetries from negative kaon measurements expected from 1 fb^{-1} luminosity operation of the EIC (~2 weeks). Bottom: The comparison of statistical accuracy of the future HERMES measurements with what one can achieve with the EIC for the s quark distribution function.

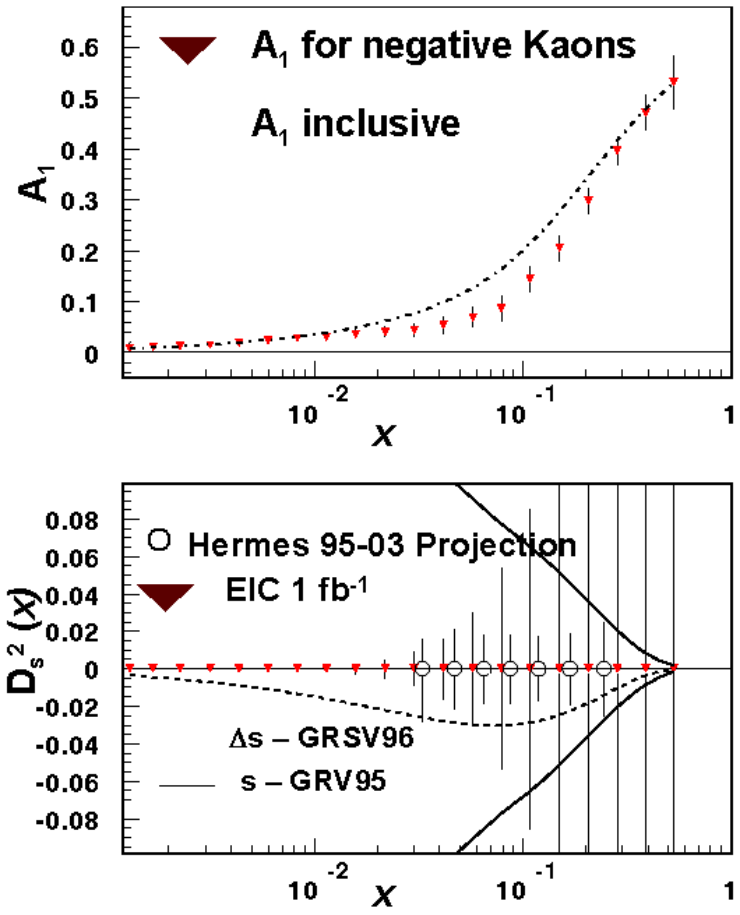

In the second analysis, if it is assumed that the up and down quark distributions are known sufficiently well, one can directly determine the strange quark distribution from any of the specific hadron asymmetries, since they all depend on the strange quark distribution. A sample of the results on the polarized strange distribution extracted from the K^- asymmetry is shown in Figure 3.7, which also displays the asymmetry. As in the previous figure, only statistical uncertainties are indicated. The results are compared with the precision expected from currently planned measurements of the HERMES experiment in the next five years.

In the Figure 3.7, the upper plot shows the simulated K^- asymmetry ($p > 1$ GeV) at measured Q^2 values (not shown). The lower plot shows the expected statistical precision of the strange quark distribution for the EIC simulation in comparison to the projected result of a HERMES analysis [33]. The positivity constraint given by the unpolarized strange quark distribution [30] is also plotted. Both figures show that the use of standard

analysis techniques on semi-inclusive data will yield a much more precise determination of the nucleon spin-flavor structure.

3.1.2.5 Parity Violating Structure Function g_5

Because the high Q^2 measurements are possible with the high-energy EIC, it also will be possible to access the parity violating spin structure functions $g_5^{(W+/-)}$ through the charged current interactions. The events in the case of W exchange are characterized by a large transverse momentum imbalance caused by the inability to detect neutrinos from the event. The charge of the W boson is dictated by the charge of the lepton beam used in the collision. Using the data from such charged current events, the parity violating spin structure functions, g_5, are expressed as:

$$A^{W} = \frac{d\sigma^{W}_{\uparrow\downarrow} - d\sigma^{W}_{\uparrow\uparrow}}{d\sigma^{W}_{\uparrow\downarrow} + d\sigma^{W}_{\uparrow\uparrow}} = \frac{(+/-)bg_1^{W} + ag_5^{W}}{aF_1^{W}(+/-)bF_3^{W}} \approx \frac{g_5^{W}}{F_1^{W}}$$

where a and b, kinematic factors associated with the kinematic variable y and W and includes $W^{(+/-)}$. The spin structure functions, g_5, are combinations of polarized u, c, $\bar{d}$ and $\bar{s}$ quark distributions.

$$g_5^{W+} = \Delta d + \Delta s - \Delta\bar{u} - \Delta\bar{c}$$
$$g_5^{W-} = \Delta u + \Delta c - \Delta\bar{d} - \Delta\bar{s}$$

A Monte Carlo study, including the detector effects, showed that the measurement of the above asymmetry and the parity violating spin structure function is feasible at the EIC. Figure 3.8 (a) shows the asymmetry vs. log (x) and 3.8 (b) shows the spin structure function g_5 vs. log (x) calculated for W^- with 2 fb^{-1} luminosity [34]. Similar estimates exist for W^+ but would require measurements with a positron beam. The curves assume Gehrmann-Sterling spin structure functions for the values of the asymmetries and the spin structure functions, where it assumed that the F_1^W would be measured well at HERA by the time this measurement will be performed at the EIC. The simulated data shown in the Figure 3.8 are for $Q^2 > 225$ GeV^2. Standard assumptions used by H1 collaboration about the scattered electrons for good detection were applied. The results could be obtained (including machine and detector inefficiencies) in a period of little over one month with the EIC luminosity.

It is possible that only one or both of the electron-proton and positron-proton collisions could be performed, depending on which design of the accelerator is finally chosen (Section 4.0). In the linac-ring design, it would be impossible to have positron-proton collisions because there may not be a strong enough positron source. Even if this is the case, there is no foreseeable measurement of the parity violating spin structure function g_5^{W-} anywhere in the world. Therefore the EIC could provide a unique and important measurement that could otherwise be performed only if the HERA proton beam is polarized in the future.

Figure 3.8: Statistical Uncertainty of the Asymmetry of $A(W^-)$ and $g_5(W^-)$

Figure (a) is the projected statistical uncertainty on the asymmetry that can be measured with the EIC operating at high center-of mass energy. Figure (b) assumes that the structure function xF_3 will be measured by the time the EIC takes data, the spin structure function g_5 could be measured with this accuracy.

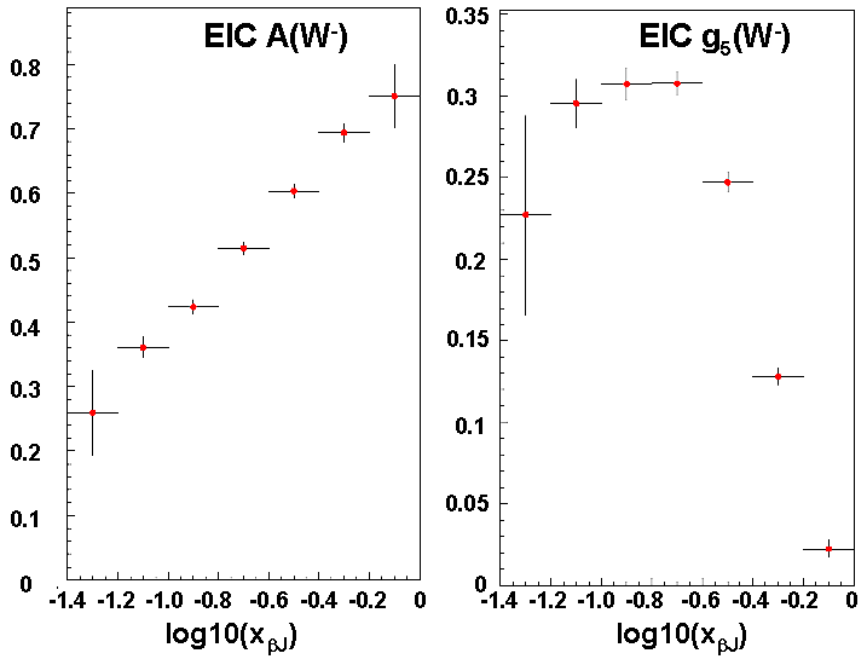

3.1.2.6 Transversity $\delta(x,Q^2)$

Researchers have explored the helicity conserving part of the lepton-nucleon scattering cross-section by measuring the nucleon structure functions, F_2 and g_1. In contrast, no information is available on the helicity flip amplitude. The absence of experimental measurements is a consequence of the chiral odd nature of the helicity flip amplitude and the related transversity quark distribution, $\delta(x,Q^2)$ that prevents the appearance of the helicity flip contribution at leading twist in inclusive experiments.

The current interest in transversity distributions comes from a recent HERMES result that suggests that the Collins fragmentation function, H_1, is sizable. The Collins fragmentation function is determined by measuring the azimuthal dependence of the leading hadrons in the quark jet. A semi-inclusive DIS experiment at the EIC would probe this spin structure function. A transversity measurement at the EIC will extend the HERMES x-range from $x = 0.04$ down to $x = 5 \times 10^{-4}$, in about a fraction of a week of data acquisition with 10% of the presently published HERMES statistical accuracy [35]. The measurement would require a large acceptance detector with rapidity coverage of at least –3.5 to +3.5. Figure 3.9 shows the statistical accuracy possible for the measurement for five different z bins (z is the fraction of proton momentum carried by the tagged final state hadron) in 1-day data acquisition at the EIC.

Figure 3.9: Potential Statistical Accuracy for Measuring the Transversity Distribution Function δ(x)

These figures show the potential statistical accuracy for measuring five different z bins. z is a fraction of proton momentum carried by the tagged final state hadron. Statistical errors shown could be achieved in 1-day of running of the EIC.

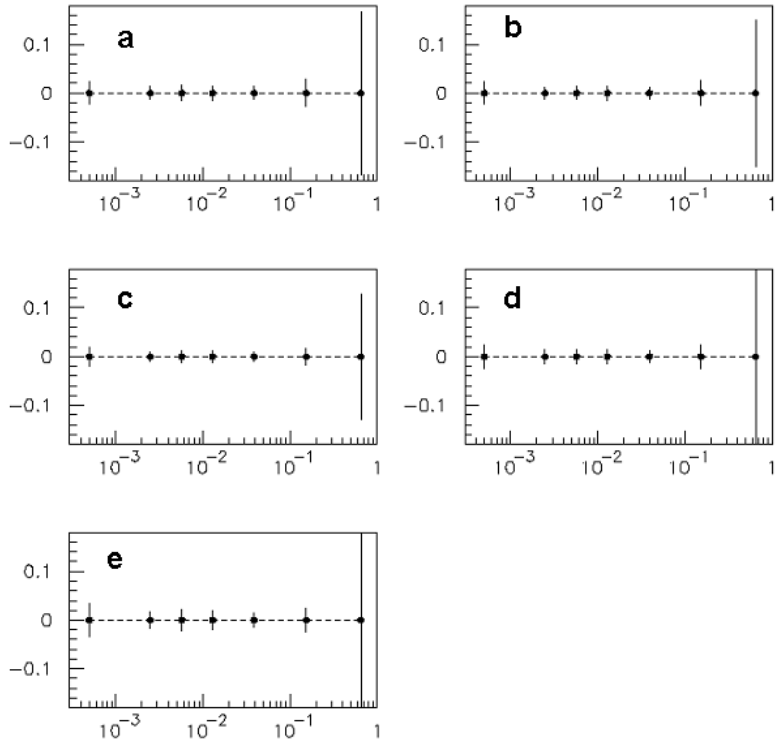

3.1.3 Hard Exclusive Deeply Inelastic Processes and Hadron Structure

There was a surge of theoretical and experimental studies of large Q^2 exclusive processes: DES or Deep Exclusive Scattering including production of photons, and Deeply Virtual Compton Scattering, DVCS:

- Deeply Virtual Compton Scattering (DVCS)

$$e + N \rightarrow e + \gamma + Baryon(N, \Delta, N\pi),$$

- Deep Exclusive Scattering – DES

$$e + N \rightarrow e + Meson + Baryon(N, \Delta, N\pi, \Lambda)$$

One also can consider the processes, where a few mesons, a baryon or an antibaryon are produced instead of a meson [36].

The factorization theorems for these processes, DVCS [37,38,39,40] and DES [41,42], state that the amplitude of the process can be written as a convolution of three blocks: a generalized parton distribution (GPD) of the nucleon (a nucleon-baryon transition), the

hard interaction block calculable in pQCD, and the light-cone wave function of a photon or for the produced mesonic system in a minimal Fock $q\bar{q}$ state (Figure 3.10)

The GPDs, which describe DCVS and DES, can be qualitatively interpreted as the amplitudes for removing a parton with given quantum numbers from the nucleon and putting another quark back into the system with a different light-cone fraction at the same impact parameter. Therefore, they provide a new highly localized way to probe baryon wave function that is referred to as the "micro-surgery" of baryons. There are four readily accessible quark GPDs, two in the limit of t = 0 and equal quark light-cone fractions (x's) coincide with the usual unpolarized and polarized parton densities. Two other GPDs, which are more sensitive to the chiral degrees of freedom, disappear in the diagonal limit and cannot be probed in the inclusive processes.

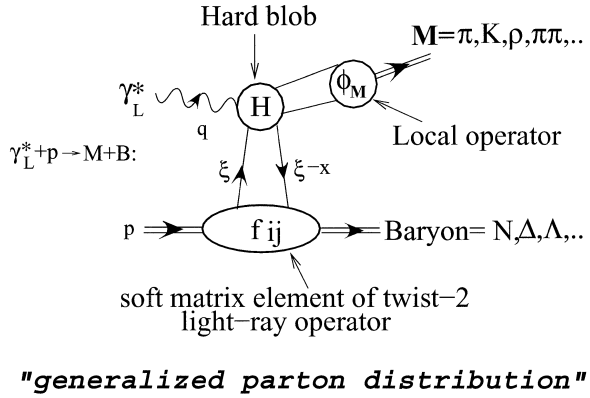

Figure 3.10: The Block Structure of the Amplitude for a Hard Exclusive Process.

This figure shows the process for production of a meson M by a longitudinally polarized photon in a reaction: $\gamma^* + p \to M + B$ where p is a proton and B is a baryon.

There are sum rules [43,38], which connect the integrals over the GPDs with the corresponding nucleon transition form factors. There is also a sum rule, which connects a certain integral of GPDs with unknown parton orbital angular momentum that makes an essential contribution to the total spin of the nucleon [38]. Though these integrals cannot be measured directly by experiment. They strongly constrain the models of GPDs. Recently, several models of GPDs were suggested based on conditions of matching to the diagonal limit, [44], the chiral QCD dynamics [45]. Therefore, the theoretical status looks very promising. Lattice-QCD may even provide "measurements" of GPDs in the kinematics not accessible directly in an experiment.

Recent studies of DVCS resulted in the NLO evolution equations for the amplitudes and led to an understanding of the coupled issues of gauge invariance and higher twist contributions [46,47,48]. Future studies of the DVCS and DES will complement each other. DVCS is likely to reach the scaling limit at lower Q^2 because of the point-like nature of the photon, while DES will provide effective ways to separate different GPDs.

Depending on the process and Bjorken x, the dominant contribution originates from the quark or the gluon exchanges. These processes allow investigation of the parton structure of nucleons and to comparison of it to that of Δ - isobars, hyperons, and $N\pi$. In addition, these processes provide a way to address a novel question about short-range

parton correlations in nucleons. For example, what is the probability of finding small color singlet clusters in the nucleon composed of a quark-antiquark pair, three quarks or even three antiquarks? These processes also probe the minimal light-cone $q\bar{q}$ components of various mesons and a few meson systems. In addition, these processes are a way to address a number of key questions about high-energy QCD including the determination of the maximum transverse color separations in high-energy strong interactions that are dominated by pQCD, and how far down in x one can use linear QCD evolution equations.

A characteristic feature of these processes is that the final state contains a particle or even a few particles that have small momenta in the target rest frame. This is a challenging, though not impossible, task for the high-energy fixed target experiments. Detection of these reactions in the collider kinematics is much easier since the particles that are slow in the target rest frame fly along the beam direction. It is also much easier to select coherent interactions with nuclei.

3.1.3.1 Hadron Micro-surgery and Tomography

Hadron micro-surgery involves either the removal of small transverse size $q\bar{q}$ pair or removal of a parton with given quantum numbers from the nucleon and insertion of another quark (generally with different quantum numbers) with a different light-cone fraction back into the system at the same impact parameter. It provides a new highly localized way to probe baryon wave functions.

Studying the t-dependence of the amplitude adds another dimension to the study of the nucleon. This involves mapping the transverse distribution of the corresponding parton distribution and one can do transverse slices of nucleons at different x. Therefore this can be considered a kind of hadron tomography.

Both hadron micro-surgery and tomography, just like usual DIS processes, are highly localized in the transverse plane. The collider kinematics at the EIC are certainly advantageous for selecting reactions of this kind since exclusiveness can be ensured by detecting hadrons produced along the proton beam.

The use of nucleon spin adds a new dimension to such studies. For example, by using transversely polarized nucleons GPDs sensitive to the chiral degrees of freedom can be studied. Large angular asymmetries are predicted for production of pions and vector mesons for the x-range where quark exchanges dominate [36,49,50]. Large spin effects are predicted for the production of hyperons (whose decays are self-analyzing), and for Δ-isobars for both polarized and unpolarized nucleons.

A study of the onset of the scaling limit for DES will be important for understanding the nature of non-vacuum Reggeon exchanges. For example, it will be possible to study the change in the pattern of the t-dependence of these processes with Q^2. In the soft limit, the t-dependence of these processes becomes much steeper with increasing energy:

($\propto \exp(2\alpha'_R t \ln(s/s_0))$, where $\alpha'_R \approx 1$ GeV^{-2}. It is predicted that with increase of Q^2, $\alpha'_R(eff)$ will decrease similar to the case of the vacuum channel where this effect was predicted for the vector meson production [41] and observed at HERA [51]

Currently such studies are performed with HERMES detector where they are building a special recoil detector for these purposes. These are also a focus of the ELFE proposal. However these will be able to study only significantly smaller Q^2 or larger x where nonperturbative dynamics may dominate. This is because $E^e_{inc} \leq 30$ GeV. It is a challenging problem to use a recoil detector with a polarized target. On the other hand fixed target detectors (if specially designed) may operate at a high luminosity - probably up to 10^{36} and can compensate for lower energies to some extent.

Chiral Dynamics Connection: The fact that the DES amplitudes factorize into three blocks opens a new field for the application and investigation of chiral dynamics. This includes production of the $\pi^+\pi^-$ system near the threshold $(M_{\pi^+\pi^-} < M_\rho)$ [52], producing a low mass $N\pi$ system [50]. The operators involved in this case are different from traditional low energy chiral dynamics and may involve gluonic operators.

3.1.3.2 Probing High-Energy Dynamics

At small x, the transition from soft nonperturbative Pomeron physics to hard perturbative high-energy physics by production of vector mesons is a the main focus. The shrinking of the transverse size of the longitudinal photon regulates this transition.

One of the most interesting interfaces of soft and hard dynamics is the high-energy interaction with nucleons/nuclei of systems of small size. These interactions grow with increase of energy much faster than the hadron-hadron interactions and may lead to a new perturbative regime of saturation discussed later. Exclusive production of vector mesons by longitudinally polarized photons, which is the dominant contribution to the $\gamma^* + N \to V + N$ processes at large Q^2, provides one of the cleanest ways to study such interactions. Studies at HERA revealed (on a semi quantitative level) several indicators of the transition to the hard regime, which is regulated by the shrinking of the transverse size of the longitudinal photon and increase of $\alpha^{eff}_{IP}(0)$ and decrease of α'_{IP} with increase of Q^2. However, to perform qualitative measurements requires a qualitative increase in the statistics, covered energy range, and the acceptance of the detectors.

A detailed study of the t-dependence of these cross-sections would lead to a study of the onset of the dynamics of saturation by the use of impact factor analysis of the scattering amplitudes [53]. Another interesting limit is the interaction of two small dipoles, which may be closer to the limit considered in the BFKL model of high-energy interactions [54]. To enhance this contribution one has to select special final states in the nucleon fragmentation region $p\pi^+\pi^-$ with large relative transverse momenta. This is just one example of the potential of double diffraction for studies of how and whether soft

factorization in the diffraction will break with increase of Q^2 as the transverse size of the exchanged system becomes smaller and smaller.

3.1.3.3 New Nucleon Spectroscopy

Studies of DES processes will provide unique opportunities to look for new baryon states. At intermediate x the main advantage is the ability to select the isospin state of the baryonic system, as compared to the spectroscopy in the $\gamma + N \rightarrow "resonance"$ processes.

The case of small x is especially interesting since the nucleon is interacting with the two-gluon ladder that is well localized in the transverse plane but extends over the whole nucleon in the longitudinal direction when viewed from the nucleon rest frame. Therefore, we can expect that this probe will effectively excite gluonic degrees of freedom in the nucleon and only in I = 1/2 state.

3.1.3.4 Experimental Considerations

The experimental requirements for a complete investigation of GPDs are formidable. Many different processes must be investigated at very high luminosity, at large enough Q^2, and with suitable energy resolution to determine reliably the final hadronic state. It is clear that one will need different accelerators to fulfill this ambitious task. EIC would be complementary to the fixed target experiments, both in kinematic range and with respect to the channels easily studied.

It is clear that measurement of DVCS is one of the cleanest processes for obtaining experimental information on GPDs. It is highly desirable to have data over a large kinematic range in x and Q^2 and low momentum transfer to the proton. Further, the measurements must be carried out in a manner to guarantee exclusivity, i.e., that the proton is intact in the final state.

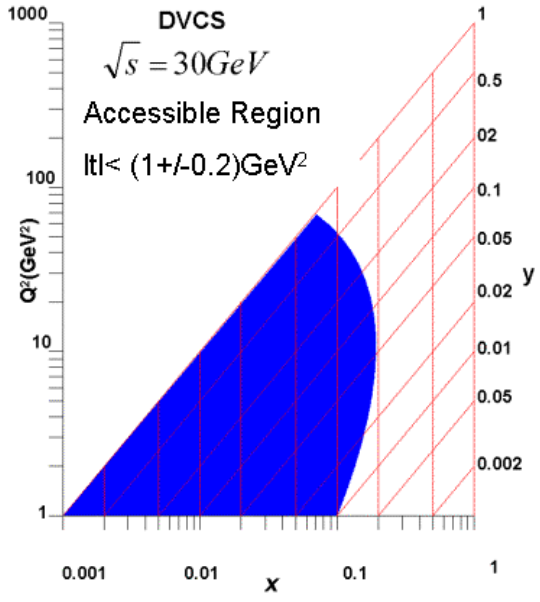

Figure 3.11: x vs. Q^2 Range of DVCS Measurable at the EIC ($\sqrt{s} = 30$ GeV)

Beam energies corresponding to $\sqrt{s}$ ~30 GeV are possible with the EIC. The lines are lines of constant y indicated on the right hand side.

At the EIC, measurement of DVCS would be accomplished by detecting the scattered electron and final-state photon at angles of about 30^0, and ensuring that no particles other than the forward-going fast protons are emitted in the final state. This technique has been used successfully in ZEUS and H1 experiments at DESY to measure DVCS at low x and high Q^2. Figure 3.11 shows the expected kinematic range for DVCS accessible at the EIC ($\sqrt{s} = 30GeV$).

3.1.4 Fragmentation: Hadronization and Spin Fragmentation

A fundamental question in hadronic physics is how quarks or gluons from high-energy scattering evolve into hadrons. This process is known as *hadronization*, often termed *fragmentation* in Deep Inelastic Scattering reactions. It is a clear manifestation of color confinement: the asymptotic physical states detected in the experiment must be color-neutral hadrons. Hadronization also appears in an astrophysical context as part of the transition from a deconfined state of free quarks and gluons in the Big Bang, into nucleons that provide the seeds for nuclear synthesis. Important areas of future study include:

- Understanding fragmentation in spin-dependent processes.
- Using fragmentation as a tool for hadron structure studies.
- Probing the global structure of the hadronic final state.

Inclusive scattering experiments give precise information on single-quark probability densities. However, much more precise data is needed to isolate the effects of particular quark flavors and helicities in order to explore fully the partonic substructure of matter. This additional data will enable an understanding of the process by which quarks in high-energy processes neutralize their color in the transitions leading to the colorless mesons and baryons detected in DIS reactions.

A polarized electron ion collider in the $\sqrt{s}$ ~30 GeV energy regime would enable studies of a number of interesting phenomena in quark-nuclear physics. One such phenomenon is the fragmentation of quarks into hadrons. In these studies, a quark makes a transition into a final hadron, which is then detected. The most commonly studied process is that of current fragmentation, shown schematically in Figure 3.12 (a).

There also is the process of target fragmentation in which a quark is struck by a virtual photon in a lepton-induced reaction, and one observes the subsequent decay of the remnants of the nucleon. The kinematic situation for target fragmentation is shown schematically in Figure 3.12 (b).

Target fragmentation is a largely unexplored regime of QCD. Observing such processes requires a detector capable of measuring decay fragments separated from the current jet by a large interval in rapidity. As a result, the collider geometry is essential for studies of

the target fragmentation region. In Figure 3.13 we show a plot [55] of rapidity versus fragmentation energy fraction *z,* for a γ* *N* invariant mass (W = (1-*x*)ys = 20 GeV).

Figure 3.12: Primary Contributions to Fragmentation Processes Leading to Hadrons in the Final State.

Figure (a) shows current fragmentation and (b) target fragmentation where the quark is struck by a virtual photon while baryon remnants fragment into the final hadron.

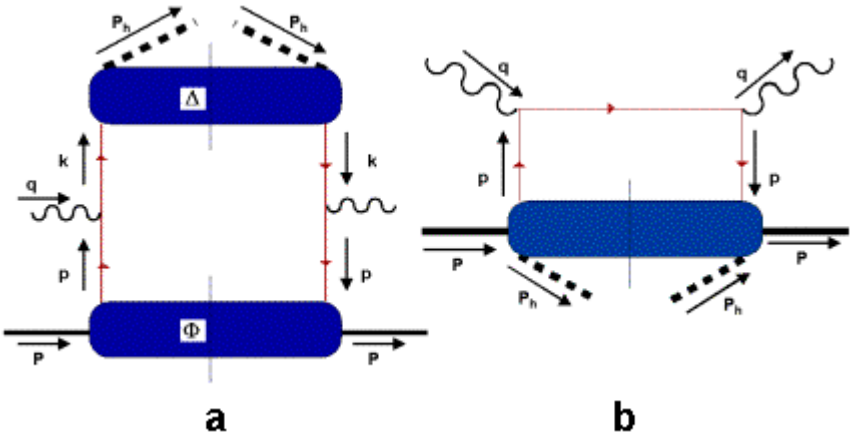

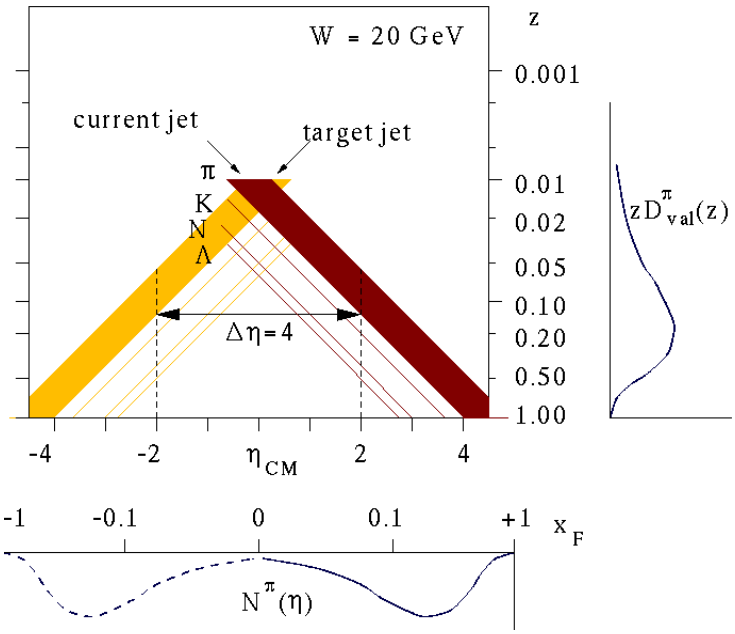

Figure 3.13: Relation Between z-Values in Fragmentation and Center-of-Mass Rapidity (W= 20 GeV).

Experience from the EMC results suggests that both current and target fragmentation regions extend over a rapidity range $\Delta\ \eta\ \sim\ 2$, where the rapidity is defined as $\eta = 0.5 \ln (P^{-}_{h}/P^{+}_{h})$. Figure 3.13 shows the z values, and demonstrates that a collider, with the properties defined in this proposal, will have the ability to access and separate both the current and the target fragmentation regimes.

Target fragmentation in DIS limit can be described in terms of quantities that are referred to as either extended [56] or conditional parton distribution functions [57]. A conditional parton distribution function represents the probability of finding a parton of a certain flavor, i, together with a hadron h, in the target nucleon. It is convenient to characterize the kinematics of the production of hadron, h, in the target fragmentation by introducing light-cone fraction of the initial proton momentum carried by the hadron: $x_h \equiv \frac{E_h + p_{3h}}{E_{inc} + p_{inc}}$, t, the invariant momentum transfer to h, and the fractional light cone momentum of the struck parton relative to the light cone momentum carried by the hadrons that do not belong to the system "h": $\beta = \frac{x}{1 - x_h} (0 \le \beta \le 1)$. A factorization theorem [57,58] states that these functions satisfy the same DGLAP equation for its μ dependence with the same kernels as for fully inclusive parton densities.

To date most of the studies of fragmentation phenomena were performed at HERA for production of leading protons and neutrons. In the diffraction kinematics studies ($1\text{-}x_p \equiv x_{IP} \le 0.02$) of inclusive hard diffraction, $e + p \to e + X + p$ confirmed the validity of the factorization theorem and led to the first determination of diffractive parton densities using the soft factorization assumption of the independence of the β distributions on x_{IP}. One of the most intriguing conclusions of these studies is the large value of the gluon diffractive distributions. This conclusion was confirmed by studies of the hard diffraction at Tevatron and has important implications for e - A physics. These studies clearly have to be extended to study the t-dependence and to check the soft factorization approximation.

In the case of the neutron production, studies were done in the limit of small x, and relatively large ($1\text{-}x_n$), corresponding to small β. In this case one expects that fragmentation is weakly correlated with x, flavor, etc of the struck parton, leading to an analog of the limiting fragmentation in soft processes [59]. This behavior is consistent with the data. At the same time one can try to interpret the neutron production as the scattering of pions assuming dominance of the process of dissociation ($p \to \pi^+ + n$) with subsequent hard scattering off the pion. In this interpretation, this process is directly proportional to the pion structure function, and might allow an independent determination of the pion structure function [60]. The main problem is the background from other fragmentation processes that may be as large as or even larger than this process for small x, β where the data were obtained.

The region that is practically unexplored is the region of finite x where a parton carrying a substantial fraction of the nucleon momentum is removed. Obviously production of baryons in this limit is very sensitive to the structure of baryons and the space-time picture of confinement. A few examples indicate the richness of this completely unexplored avenue of research.

- One of the most intriguing features of confinement in DIS is that after hard scattering at finite x, a state is produced with color distributed over large rapidity intervals.

Studies of various long-range correlations in rapidity for various observables, for example fluctuations of the differential multiplicity may provide new clues to the dynamics of the confinement.

- The presence of polarization will allow investigations of the degree of coherence of the system produced using the Collins variable for the target fragmentation region and investigated as a function of x, quark flavor, etc.
- The detection of strange baryons, with the possibility of studying their polarization through their decays, will allow studies of transfer of spin for different directions of the initial polarization of the nucleon. Similar possibilities exist for production of Δ isobars and excited baryon states.
- Investigation of the correlation between the decay of the produced system ($x_F = \frac{x_h}{1-x}$ distribution) and x_{Bj} will provide qualitatively new information about the structure of the bound state. In the picture of the nucleon composed of the valence quarks and sea partons there may be a strong change of the x_F dependence from $\propto (1-x_F)$ at $x > 0.2$ to $\approx const(x_F)$ for $x \sim 0.1$ and $1/x_F$ for $x \le 0.01$ [61]. It would be revealing to compare decay of the residual system if a valence quark or a valence gluon is removed. Also, if the struck gluons are polarized it would be interesting to find out whether residual fragments are polarized.
- Since large x DIS processes remove quarks from rather rare configurations in nucleons, there may be a significant modification of the composition of the final state for $x \ge 0.4$, in particular, enhanced production of excited baryons at large x_{Bj} including baryons from 20-plet [62] that cannot be excited in many single quark excitation processes [5].

3.1.5 Parton Distribution Functions of Mesons

At present, the pion is believed to contain a valence quark and antiquark as well as a partonic sea. Several theoretical calculations focused on explaining the pion structure function in the valence region. These include Dyson-Schwinger [63] and Nambu and Jona-Lasinio models [64]. Lower order moments of the structure function were determined by lattice gauge calculations [65]. Typical agreement with the pion structure function is shown in Figure 3.14 that shows a curve from the Dyson-Schwinger model compared to the data from a pionic Drell-Yan experiment [66] in the valence region. The general features of the valence structure of the pion are understood qualitatively. However, the $q\bar{q}$ sea in pions is not well understood. The kinematics where scattering off the pion cloud dominates in neutron production have not been unambiguously identified. This is due to the limited acceptance for neutrons and the limited momentum resolution of HERA. Additionally, only the region of low x can be probed at HERA because of the extremely high energy.

Figure 3.14: Pion Structure Function from Drell-Yan Scattering

Existing data for the pion structure function from Drell-Yan scattering processes [66]. The solid curve represents a calculation of Hecht et al. [63].

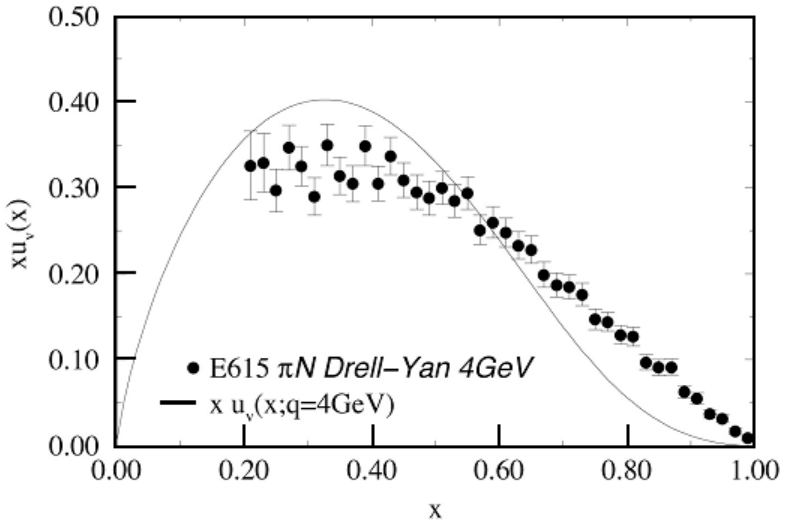

The pion structure can be measured by exploiting the Sullivan [60] process, illustrated in Figure 3.15.

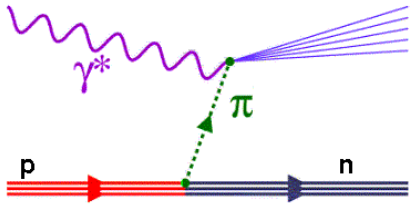

Figure 3.15: Deep Inelastic Scattering from the Pion Cloud Surrounding a Proton.

In this case, the kinematics are chosen so that the DIS occurs from the pion cloud surrounding the proton. Because of the relatively high center-of-mass energy of the Electron Ion Collider, one can select kinematics where the pion is nearly on-shell. The key to the experimental technique is to measure the outgoing neutron in coincidence with the scattered electron. A simulation of a possible experiment with a luminosity of 10^{32}cm^{-2}s^{-1} and 10^6 seconds of beam time is shown in Figure 3.16. Clearly, the experiment can readily be performed at the Electron Ion Collider facility.

The challenge of determining the pion structure function from the Sullivan process involves suppression of the background contribution from other mechanisms of fragmentation. It will be necessary to study the process as a function of the momentum transfer, t, and to use the Chew-Low procedure to extrapolate the differential cross-section for fixed β, Q^2, as a function of t to the pion pole at $t = m_\pi^2$ to separate the pion

pole contribution. This would require good resolution in β and t $\left(t = -\frac{(1-x_n)^2 m_N^2}{x_n} - \frac{p_t^2}{x_n}\right)$ and therefore in x_n and p_t for the detected neutron.

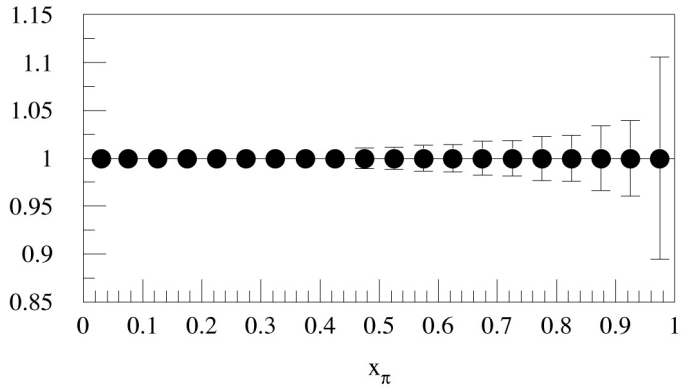

Figure 3.16: Simulated Errors for Measurement of Pion Structure Function in DIS Events

This simulation uses a 5 GeV *electron beam colliding with a* 25 GeV *proton beam with a luminosity of* 10^{32}cm^{-2}s^{-1} *and* 10^6s *of running.*

The valence structure of the kaon is comprised of a light *u* or *d* quark/antiquark and a strange quark/antiquark. If our understanding of the meson structure is correct, then the large difference between the strange quark and *u* or *d* quark masses gives rise to a very interesting effect for the kaon structure function. The strange quark, because of its large mass, carries more of the kaon's momentum than the *u* quark. Then, the u_v quark distribution in the kaon should be shifted lower in *x* than that in the pion. The sea in the kaon could be measured as well. In this case, one can consider the same process as illustrated in Figure 3.15, but with the pion replaced with the kaon and the neutron replaced with a Λ. The forward going Λ must then be detected. Since the KNN coupling constant is comparable to that for πNN, the experiment could readily be performed at the EIC. However, determination of the kaon structure function would be more problematic since the dominance of the kaon exchange far away from the kaon pole would be difficult to justify.

3.2 Exploring the Nucleus

In this section, we discuss the scientific opportunities available with the EIC in DIS of nuclei. At very high energies, the correct degrees of freedom to describe the structure of nuclei are quarks and gluons. The current understanding of partonic structure is just sufficient to suggest that their behavior is non-trivial. The situation is in some way reminiscent of QED. The rich science of condensed matter physics took a long time to develop even though the nature of the interaction was well understood. Very little is known about the "condensed matter", many-body properties of QCD, particularly at high energies. In this section, we propose that the EIC is the right machine to open up this new frontier of QCD. We further argue that there are sound reasons based in QCD, to believe that partons exhibit remarkable collective phenomena at high energies. If the EIC can probe this regime, it has the potential to revolutionize our understanding of the strongest force in nature.

In Section 3.2.1, we discuss the measurement of parton distributions in nuclei in high energy DIS. The EIC will be able to measure the parton distributions to higher statistical accuracy and in a significantly wider x and Q^2 range than previous fixed target experiments. With the higher statistical accuracy and the wider kinematic range, there are several outstanding questions that can be addressed. In Section 3.2.2 we discuss how the EIC helps expand our microscopic understanding of nuclear binding. Modifications of the parton densities at $x \sim 0.1 - 0.4$ may be related to the microscopic structure of intranuclear forces that result in nuclear binding. With the large range of nuclear targets available, this issue can be addressed with the EIC. The space-time evolution of partons in a nuclear medium is discussed in Section 3.2.3. The key concepts are energy loss, transverse momentum broadening, color transparency and color opacity. These can be tested in the EIC environment, and may provide concrete manifestations of quantum mechanical coherence in QCD.

The concepts and measurements discussed here would fill in significant gaps in our understanding of nuclear structure. They will prove crucial to understanding other experiments at high energies. In particular, they will deepen our understanding of the initial conditions for the formation of the quark gluon plasma in heavy ion collisions. They also will provide a firm understanding of the final states that are probes of the properties of the quark gluon plasma. High-energy DIS may, however, reveal that the parton distributions are remarkable in and of themselves, and may answer outstanding question on the nature of high-energy scattering in both nuclei and nucleons. This aspect will be discussed in Section 3.2.5 where many of the concepts presented here will be discussed from a different perspective.

3.2.1 Parton Distributions in Nuclei

What is known about the distributions of quarks and gluons in nuclei? We noted in Section 2, that past fixed target experiments measured structure functions for nuclei for a wide range in x and Q^2. Primarily the A-dependence of the structure function, $F_2^A(x,Q^2)$, was measured with very limited information about the A-dependence of the longitudinal structure function ($F_L^A(x,Q^2)$). In the Leading Order in QCD in the limit of large Q^2, this structure function is interpreted as the sum of quark and anti-quark distributions in the nucleus. However, much of the data at low x (< 0.005) have been at low Q^2 (Q^2<1 GeV^2). Information on the A-dependence of the gluon structure function ($G_A(x,Q^2)$) could in principle be extracted from the scaling violation of the ratio of F_2^A / F_2^d or from the charm production that is dominated by the photon-gluon fusion. In practice the data are limited to the comparison of two nuclei, tin (Sn) and carbon (C), and suggest a two sigma effect of enhancement of the gluon field with an increase of A at $x \sim 0.1$. However the range of Q^2 is not large enough and minimal Q^2 is too small to make unambiguous conclusions from the scaling violation data. The dominance of gluon fusion in J/ψ production is not as clear as it is for open charm production. Nevertheless, when the deep inelastic data are combined with the Drell-Yan data on the A-dependence of the antiquarks in nuclei, there is an extremely provocative picture of enhancement of

the gluon and valence quark fields at $x \sim 0.1$. This may be relevant for understanding the microscopic origin of the nuclear forces.

The EIC, with its ability to perform measurements at low x and at high Q^2, and to tune the center-of-mass energy, will provide high precision structure function data for a range of light and heavy nuclei, in *terra incognita.* The longitudinal structure, which is very sensitive to the gluon density function at $x \leq 0.1$, will be measured in the small x region for the first time. Further, in the collider environment, semi-inclusive measurements will be significantly easier. The A dependence of the valence quark distribution from semi-inclusive final states could be extracted by measuring the difference of the cross-sections for production of π^+ and π^- for energies where leading hadrons are not absorbed in nuclei. When combined with the measurements of the A-dependence of F_2^A, this could provide independent information about the A-dependence of the sea.

By measuring nuclear structure functions, questions about the partonic structure of nuclei at high energies will be answered on fundamental level. EIC will enable probes of the more interesting properties of these structure functions that distinguish them from *nucleon* structure functions. The most striking of these is shadowing.

Even though shadowing has been observed at small x (< 0.1) in fixed target experiments, it is still not clear where use of the leading twist formalism of QCD, which allows interpretation of the process as scattering off quarks and gluons, becomes applicable. For example, the parton model interpretation of experimentally measured structure functions as quark and gluon distributions breaks down in the low x and low Q^2 region.

Shadowing is the phenomenon where $F_2^A(x, Q^2)/A\,F_2^N(x,Q^2)$ is less than 1 at small x(< 0.1). It reaches full strength in the region where the coherence length of the projectile probe $\left(l_{coh} \sim \frac{1}{2m_N x}\right)$ exceeds the intra-nuclear longitudinal distance between any two nucleons in the nucleus. The nuclear parton distribution is not merely the sum of nucleon parton distributions but also contains the interference between the parton distributions of the nucleons. When the coherence length is larger than the nuclear diameter, $l_{coh} >> 2A^{1/3}$, or $x << 1/(4m_N A^{1/3})$, the projectile interacts coherently with the entire nucleus and nuclear collective effects may be large.

There are several unresolved questions about shadowing as given in the framework of QCD. EIC will be the tool to help answer these questions.

- Is shadowing a leading twist effect, namely, is it unsuppressed by a power of Q^2? An empirical answer to this question would help settle whether shadowing is an intrinsically leading twist phenomenon [For a review see 67], or whether it is due to weak coupling, higher twist, high parton density effects [68,69,70].
- What is the relation of shadowing to parton saturation? Does parton saturation provide a microscopic understanding of shadowing?

- Is there a minimum to the shadowing ratio for fixed Q^2 and A with decreasing x? If so, is it reached faster for gluons or for quarks? Predictions for quark and gluon shadowing in a specific leading twist model [71] based on diffraction information from HERA are shown in Figure 3.17. [For review see [72,73]]
- What is the relation of shadowing to diffraction in e – N scattering? The relation is well established at low parton densities. In particular, the data for F^A_2/F^d_2 are explained in many models all based on the Gribov relation [74] between shadowing and diffraction. How is it modified at high parton densities? The EIC can test this fundamental relation directly.
- Is shadowing universal? For instance, are the gluon structure functions extracted from p - A collisions at RHIC identical to those extracted from e - A in the same kinematic regime. The naive assumption that this is the case may be untrue if higher twist effects are important. What are the implications for nucleus-nucleus collisions?
- Shadowing is believed to be an initial state effect, a property of the structure functions. Can we use shadowing measurements to separate initial from final state effects in studies of energy loss in e - A collisions?
- How large is shadowing for valence quarks? Is it larger or smaller than for the sea quarks?

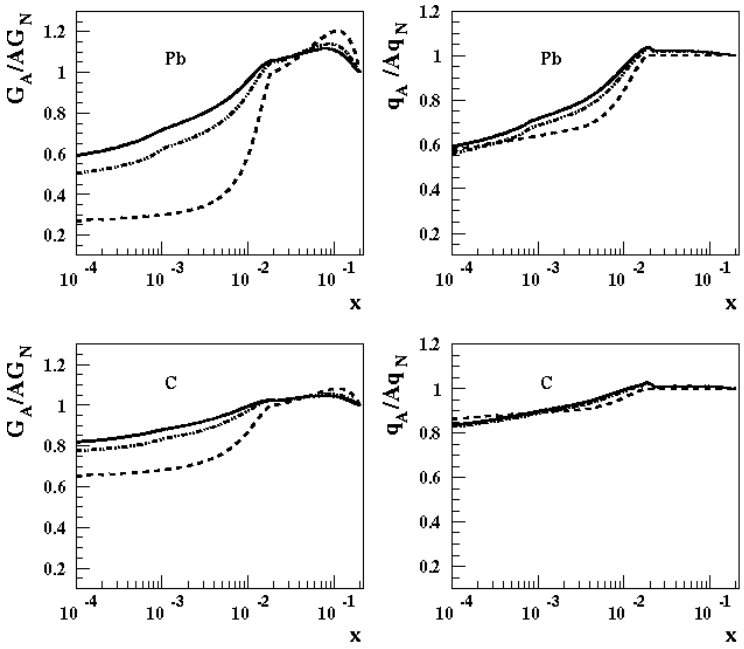

Figure 3.17: Gluon and Quark Shadowing for Pb and C

Left Panels: Gluon shadowing $G_A(x,Q^2)/AG_N$ (x,Q^2) vs. x_{Bj} for Pb and C. Right Panels: Quark shadowing $q^A(x,Q^2)/Aq^N(x,Q^2)$ vs. x_{Bj} for Pb and C. The different curves correspond to Q=2 GeV *(dashed),* Q=5 GeV *(dotted) and* Q=10 GeV *(solid). Calculations are from reference [71,75].*

The answer to the first three questions can be obtained by measuring the structure functions $F_2^A(x,Q^2)$, $F_L^A(x,Q^2)$, and $G_A(x,Q^2)$ and their logarithmic derivatives with respect to x and Q^2 with statistical precision in a wide x-Q^2 range. Estimates for the EIC (Section 4.0) suggest that a luminosity of 100 pb^{-1} is possible. The statistical accuracy of data for this luminosity, compared to that of the NMC fixed target result, for the

logarithmic derivative of ratio $R=F_2^A(x, Q^2)/A\,F_2^N(x,Q^2)$ with respect to Q^2 is shown in Figure 3.18.

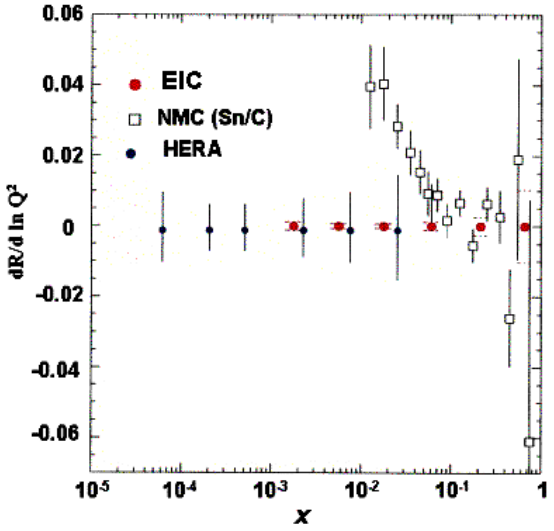

Figure 3.18: Projected Statistical Accuracy of the Measurement of ln Q^2 Derivative of the Ratio (F^A_2/AF^N_2) as a Function of x

The projected statistical accuracy of $\partial(F_2^A/F_2^N)/\partial \ln Q^2$ *as a function of x for Ca and D with the EIC per* pb^{-1}. *Current estimates suggest that the EIC will have a luminosity of several hundred* pb^{-1} *for DIS off large nuclear targets.* [76]

With this luminosity, logarithmic derivatives can be extracted with high statistical accuracy. The important issue facing experimentalists is not statistical accuracy but rather control of systematic errors to better than 1%. In particular, the major problem will be measuring the relative luminosities of the differing e - A interactions to appreciably better than 1%. The presence of the high precision data from NMC [77] for the nucleus/deuteron ratio in the kinematics that overlap with the EIC will be extremely helpful.

In the last decade, great progress has been made in defining and measuring [72,73] diffractive structure functions. At HERA, approximately 10% of the events were hard diffractive events where the proton remained intact and the virtual photon fragmented into a hard final state producing a large rapidity gap between the projectile and target. Hard diffraction probes the partonic content of long-range color singlet exchanges and provides a unique measure of the dynamics of confinement in QCD. The EIC will provide the opportunity to make the first measurement of nuclear diffractive parton distribution functions. It will enable researchers to answer questions definitively about the nuclear-dependence of the parton structure of the color singlet exchanges.

Several models predict that the fraction of hard diffractive events may be significantly larger for nuclei than for nucleons, reaching the level of 30-40% for heavy nuclei. A measurement of hard diffractive events would be a striking signature of novel physics in QCD. Researchers also can address empirically the question raised about the relation of diffraction to shadowing. To measure hard coherent diffraction, one needs to ensure that the nucleus remains intact. It is a rather challenging problem and one possible detector design that addresses this issue is discussed in Section 5.0.

By the time the EIC is available for taking data, there should be data available on structure functions for some of the kinematic region. Experimentalists can then empirically test the question of whether nuclear diffractive parton distributions are universal. Data from HERA and Fermilab suggest [78] that diffractive parton distributions are universal only in a limited sense [57] exclusively for lepton-hadron processes. The universality of nuclear diffractive parton distributions also can be tested with p - A and e - A diffractive distributions. As noted previously, parton distributions can be extracted from semi-inclusive processes. A comparison of these to those extracted from inclusive measurements also is a test of universality.

Many of the topics discussed in this section will be revisited and discussed in the framework of high parton densities in nuclei and their consequences.

3.2.2 Nuclear Binding

In the region of $x \sim 0.1$, one probes internucleon distances at which quark and gluon wave functions of nearby nucleons begin to overlap. As discussed in Section 2, studies of the parton structure of nuclei at $x \geq 0.05$, where shadowing effects are not important, have led to a number of surprises. The EIC will be able to produce quantitative information about modification of parton densities at the $x \sim 0.1$ region that is sensitive to the quark-gluon structure of nucleon-nucleon interactions. Obviously this will have a major impact on our understanding of the nature of the short-range nuclear forces.

Semi-inclusive measurements may provide crucial additional information about the origin of the EMC effect and the role of the meson exchanges. Certainly such studies should be considered in combination with the program to investigate the final state interactions in DIS that will ultimately allow corrections for these effects. Here we consider two examples.

Deuteron Fragmentation and Search for Non-nucleonic Degrees of Freedom in Nuclei: We have discussed the DIS process $e + d \rightarrow e + spectator\ \ p\ +\ X$, which could be used to tag the scattering off a quasi-free neutron. The condition of quasi-free scattering corresponds to requirement that $\alpha \equiv 2p_p / p_d \approx 1$, and $p_t \leq$ 100 MeV. The key question is how does the structure function of the off-shell nucleon depend on its off-shellness or its virtuality [12]? In the kinematics the $\alpha \geq 1$ contribution to production of nucleons in the inelastic e - N scattering is negligible. In the impulse approximation one can write

$$\frac{d\sigma^{eD\rightarrow epX}}{d\phi dx dy d(\log\alpha) d^2 p_t} \approx \frac{2\alpha_{em}^2}{xyQ^2}(1-y)S(\alpha, p_t)F_{2N}^{eff}\left(\frac{x}{2-\alpha}, p_t, Q^2\right),$$

where $S(\alpha, p_t)$ is the nucleon spectral function of the deuteron, and $F_{2N}^{eff}\left(\frac{x}{2-\alpha}, p_t, Q^2\right)$ is the effective structure functions of the bound nucleon. Based on the expectation [79] that final state interactions should not depend strongly on x, it may be advantageous to consider the ratio of cross-sections in two different bins of $\tilde{x} \equiv \frac{x}{2-\alpha}$ where the EMC

effect is small ($\tilde{x} \sim 0.1 - 0.3$) and the bin where the EMC effect is large ($\tilde{x} \sim 0.5 - 0.6$) [12]. The analysis [79] shows that different models of the EMC effect lead to qualitatively different predictions for this quantity; from a 20% effect to no effect at all.

In addition one can look for the exotic processes that could arise because of the presence of hidden color configurations in the deuteron or $\Delta\Delta$ components. These have been predicted for various nuclei such as the deuteron, with probabilities $\geq 1\%$ for the deuteron and few percent for heavier nuclei [see e.g. 80]. Theses exotic states would be manifested in production of Δ – isobars and N*s at $\alpha \geq 1$. Strategies were suggested for studying fragmentation of the deuteron in DIS which would allow observation of the $\Delta\Delta$ and hidden color states if their probability in the deuteron is $\geq 10^{-3}$ [81].

Meson Exchange in Nuclei: Presently, there is very little theoretical guidance on what to expect from a nuclear medium modification of the pion structure function. From a straightforward application [82] of the Nambu-Jona-Lasinio model, it appears that there would be no medium modification. However, the NJL model does not explicitly include binding. If instead, Brown-Rho scaling [83] is valid (i.e., variation of the meson mass with nuclear density), then we expect a significant medium modification as shown in Figure 3.19.

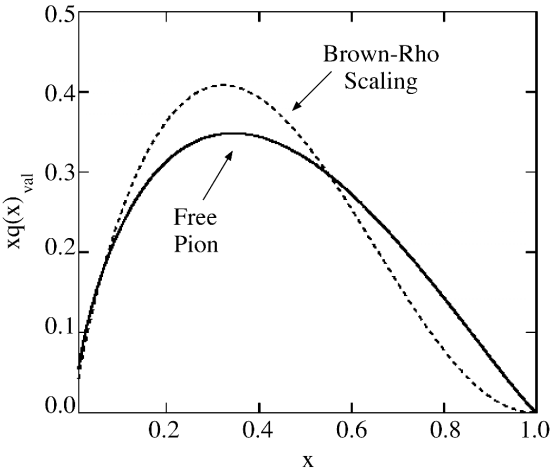

Figure 3.19: Pion Structure Function in Nuclear Medium and Effects of Brown-Rho Scaling

The solid curve represents the Nambu and Jona-Lasinio calculation of the pion structure function in a nuclear medium, while the dashed curve gives the effect of Brown-Rho scaling in nuclear matter [82].

It would be interesting to consider semi-inclusive DIS scattering for the channels where exchange by a pion maybe enhanced to observe whether the pion field is modified in nuclei. The prototypical process is the Sullivan process in a nucleus. An example of the Sullivan process applied to a nucleus is illustrated in Figure 3.20. Here, one performs Deep Inelastic Scattering from a pion in the meson cloud of nucleons in a nucleus [84].

This type of experiment would be extremely difficult in a fixed target experiment since the recoiling nucleus would essentially be a spectator. In principle, the collider geometry should make it relatively straightforward to detect the recoiling nucleus. Whether the Sullivan process corresponds to the right kinematic region at the EIC is a difficult experimental question that requires further study.

Figure 3.20: Deep Inelastic Scattering from Pions in a Nucleus

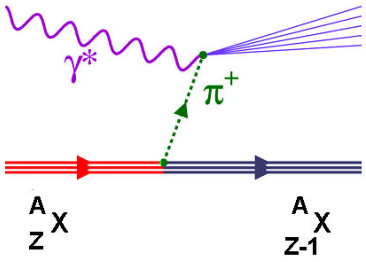

One possible example is the process of scattering off ^{3}He with detection of the final state of ^{3}H. Researchers could investigate the $\beta = x/(1-x_{3_H})$ dependence of the cross-section for different recoil ^{3}H momenta. If the process is dominated by emission of a virtual pion one would be able to interpret this as a measurement of the quark distribution in a virtual pion. There are caveats: the first is the issue of absorptive corrections, and the second is the final state interactions that can easily lead to a break up of the recoil nucleus and which may depend on β and recoil momentum.

Another possible process, which is somewhat less affected by the final state interactions, is the process of the deuteron break up producing two protons with reasonably large momenta in the deuteron rest frame. In this case spectator contribution is strongly suppressed and we may observe effects of meson exchange on the parton level [61].

3.2.3 Space - Time Correlations in QCD Processes

The EIC will allow qualitative progress in studies of the space-time picture of strong interactions relative to previous fixed target DIS experiments. The reasons for this are:

- The high luminosity of the EIC will increase by many orders of magnitude the current data sample of DIS scattering off nuclei at high energies.
- The EIC will provide a much broader range of Q^2 and x making it possible to compare dynamics for approximately the same space-time coherence lengths $l_{coh} \approx \frac{1}{2m_N x}$ as a function of Q^2. Fixing $x(l_{coh})$ allows the separation of events where a photon is transformed into a strongly interacting system either before or inside the nucleus.
- The collider geometry will enable measurements currently impossible in fixed target kinematics. In particular, a hermetic detector would clearly isolate coherent processes as well as quasi-elastic processes in DIS off nuclei.
- The detection of nucleons produced in the nuclear fragmentation region would make it feasible to study DIS as a function of the number of the nucleons involved in the interaction. In particular, it will be possible to isolate the central impact parameters

of collisions. This is very important in studying nuclear amplification effects in space-time evolution.

3.2.3.1 Color Coherent Phenomena

In Section 2.4.1 we briefly reviewed the current status of the investigation of exclusive diffractive processes of nuclei. Perturbative QCD, in the limit of large Q^2 predicts [41] that the cross-section of coherent vector meson production by the longitudinally polarized photons is given by the following equation.

$$\left.\frac{\frac{d\sigma(\gamma^* + A \to V + A)}{dt}}{\frac{d\sigma(\gamma^* + N \to V + N)}{dt}}\right|_{t=0} = A^2 \frac{G_A^2(x,Q^2)}{G_N^2(x,Q^2)}$$

This applies up to small corrections due to the skewed kinematics of the exclusive meson production. It implies that for $0.01 \le x \le 0.05$ one expects an onset of the regime of the color transparency. Qualitatively this is due to the dominance of the small transverse size configurations in the $\gamma_L \to q\bar{q}$ transition and a suppression of the subsequent interaction of the small $q\bar{q}$ dipoles with the media before conversion into the vector meson final state well past the nucleus. The onset of color transparency is expected to occur at significantly smaller Q^2~5GeV^2 than $Q^2 \ge 10$ GeV^2 where the higher twist corrections to the cross-section become small. Similarly, for incoherent processes, such as $e + A \to e + meson + excited\ nucleus$, the cross-section for $-t \ge 0.1\,\text{GeV}^2$ approaches the sum of the cross-sections of scattering of individual nucleons.

Knowing the minimal Q^2 at which Color Transparency is observed would be very important in establishing the Q^2 range in which deep exclusive processes of meson production apply, (e.g., $\gamma_L^* + N \to meson + baryon$) is dominated by the small size $q\bar{q}$ configurations and can be used to the study the fine details of baryon structure and of generalized parton distributions (see Section 3.1.2.7).

The EIC is optimal for these studies since researchers will be able to study processes at fixed x as a function of Q^2 as well as separate both coherent processes where the nucleus remains intact and inelastic diffraction where the nucleus breaks without production of mesons.

For smaller x, coherent interactions of a small dipole with several nucleons will give rise to the onset of color the opacity regime. This interesting regime is discussed further in the sub-section on high parton densities (Section 3.2.5).

At the EIC, DIS off polarized deuterons will facilitate studies of the quark-gluon structure of the neutron. Further, researchers can investigate processes where the incoming system interacts coherently with both nucleons of the deuteron. The simplest process is the coherent production off the deuteron at large enough momentum transfer: $\gamma^* + d \to V + d$.

In this case the double scattering contribution can be separated kinematically and investigated for its Q^2 dependence. If the deuteron beams are polarized it will be possible to study double scattering effects in a much wider range of momentum transfer since the relative importance of the impulse approximation contribution and double rescattering depend strongly on the deuteron polarization over a wide range of momentum transfer [85].

In addition, it will be possible to investigate inclusive diffraction. In the limit where leading twists dominate the study of the A-dependence of diffractive parton densities, the role of diffractive configurations of different transverse size can be separated. This permits the transverse mapping of the "nuclear Pomeron". Recently a special class of semi-inclusive hard diffractive processes off nuclei was observed. The process ($\pi + A \to 2\ high\ p_t\ jets\ + A$) exhibits color transparency and probes the $q\bar{q}$ component of the pion wave function [86]. Similar studies will be possible at the EIC for the quasi-real and virtual photons. Heavy nuclei will enhance Fock space components in the virtual photon wave function with small transverse separation between the constituents: $q\bar{q}, q\bar{q}g$. In addition, the photon wave function for these configurations can be measured, including the dependence of the wave function on the flavor in reactions $\gamma^* + A \to q\bar{q}''\ dijet'' + A$, $\gamma^* + A \to q\bar{q}g''\ trijet'' + A$.

3.2.3.2 Study of Space -Time Correlations in Inclusive Processes

For large values of momentum transfer Q^2 in DIS off a nucleon, the struck quark would normally go through gluon radiation and subsequently hadronize into the final particles in a process known as jet fragmentation. The final hadron distribution, known as the jet fragmentation function, can be separated from the lepton-quark scattering cross-section. It follows the standard QCD DGLAP evolution equation as a result of the final state QCD radiation (We suppress the flavor dependence of the fragmentation functions.):

$$\frac{1}{\sigma^{\gamma^* A}(x,Q^2)} \frac{d\sigma^{\gamma^* + A \to h + X}(x,Q^2 z)}{dz} = f(z, \ln Q^2).$$

Here, z is the light-cone fraction of the photon energy carried by the leading hadron. The universal jet fragmentation functions and their QCD evolution have been studied extensively in many processes other than DIS such as e^+e^- annihilation and $pp(\bar{p})$ collisions. This expression is independent of A, consistent with energy loss only weakly a function of the incident energy. These energy losses occur because of additional scattering of the struck quarks with partons from other nucleons inside the nucleus. This rescattering will induce additional gluon Bremsstrahlung and lead to a modified jet fragmentation function caused by higher twist effects.

The first $1/Q^2$ correction can be written in a generalized factorization approach as a modified fragmentation function [87]. The leading contribution from rescattering of a gluon from another nucleon is proportional to twist-four parton matrix elements of the nucleus. The rescattering-induced gluon Bremsstrahlung with small transverse

momentum l_t or large formation time ($\tau_F \sim Q^2 / l_t^2 M_N$, where M_N is the nucleon mass in the nucleus rest frame) is suppressed because of the Landau-Pomeranchuk-Migdal (LPM) interference with the final state radiation of the lepton-quark scattering. The surviving induced Bremsstrahlung has a minimum transverse momentum $l_t^2 \geq Q^2 / MR_A \sim Q^2 / A^{1/3}$. The twist-4 contribution to the modified fragmentation function in this case is proportional to $C\alpha_s A^{1/3} / l_t^2 \sim C\alpha_s A^{2/3} / Q^2$. This depends quadratically on the nuclear size. This non-Abelian LPM interference effect is a unique and interesting phenomenon in a nuclear environment. The coefficient *C* contains information about the twist-four parton matrix element in a nucleus.

Figure 3.21 shows the predicted nuclear modification to the fragmentation function $D^A(z) / D^d(z)$ for different values of initial quark energy at a fixed value of Q^2= 4 GeV^2. Recent HERMES data fix the constant *C* [88]. The effect of nuclear modification is the largest for small and moderate values of the energy transfer when the total energy loss is large compared to the initial quark energy. For fixed *x* it decreases $\propto 1/Q^2$.

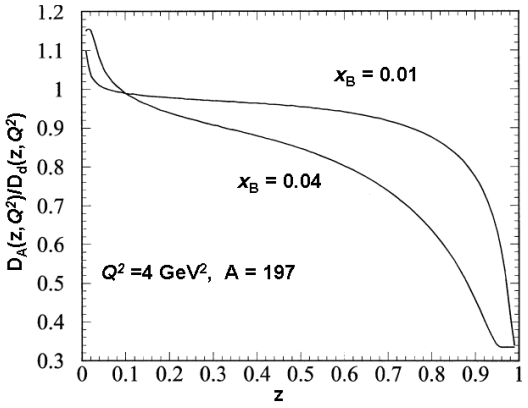

Figure 3.21: Predicted Nuclear Modification to the Fragmentation Function for Different Values of the Initial Quark Energy at Fixed Value of Q^2 = 4 GeV^2

The predicted modification [87] to the quark fragmentation functions for two different values of Bjorken x_B, and Q^2 = 4GeV^2.

The LPM interference effect in the gluon Bremsstrahlung is explicitly embedded in the combined twist-4 parton matrix elements that consist of diagonal and off-diagonal matrix elements. These nuclear twist-four parton matrix elements can be decomposed as the convolution of the generalized parton distributions in nucleons and two-nucleon correlation function inside the nucleus. Therefore, measurements of the nuclear modified jet fragmentation function help elucidate the nuclear properties at high energies and could probe the generalized parton distributions in nucleon.

The modification of the fragmentation function can be viewed as the direct experimental consequence of the parton energy loss caused by the induced gluon Bremsstrahlung. It suppresses the large momentum hadrons in the jet fragmentation process. Therefore, measurement of the modified fragmentation function in nuclear DIS will provide direct information about parton energy loss in nuclear medium.

The EIC will facilitate a check of whether fragmentation functions become universal at large Q^2 because there is a unique Q^2 range at fixed *x*. The high luminosity of the EIC will allow researchers to focus on the region of large *z* and $l_t^2 \geq Q^2 / A^{1/3}$ where

rescattering effects may survive up to much larger Q^2 than in the case of the z-distributions over l_t. It may be promising to study the A-dependence of the imbalance between jets, similar to the lower energy $\gamma - A$ experiment [89].

The space-time picture of the parton - hadron transition in DIS processes is best revealed in the A-dependence of the hadron spectra at small z, and in the nuclear fragmentation region. For large enough x, the process in which a photon knocks a parton from the nuclear interior, provides the cleanest way to look for the formation of slow hadrons from the evolving quark-gluon shower produced in the space-time evolution of the fast quark produced. The parton model for the spectrum predicts [see review in 90] that

- The spectrum is not modified for the energies of the hadrons produced above energy $E_h(A) \sim \mu^2 R_A$.
- The spectrum is suppressed for $E \sim E_h(A)$.
- The spectrum is enhanced by a hadronic cascade at energies much smaller than $E_h(A)$.

The situation will change *qualitatively* at small x where γ^* transforms to the quark-gluon system well before the target. In this case, there will be a suppression of the spectrum at rapidities, $y \sim y_{\max} - \ln(Q^2/Q_0^2)$, and an enhancement of the spectrum by a factor $\sim A\sigma_{tot}^{\gamma^* N}(x,Q^2)/\sigma_{tot}^{\gamma^* A}(x,Q^2)$ at central rapidities [71]. A further enhancement in the nucleus fragmentation region may result from rescattering of hadrons formed inside the nucleus. It would very interesting to compare A-dependence of mesons production of different sizes to see whether effects similar to those observed in production of J/ψ and ψ' in p - A scattering (see Section 2.4) are present in e - A collisions.

The large rapidity coverage of the EIC will facilitate studies of long range rapidity correlations, and event by event fluctuations in the structure of the final states. For example, a wide range of quasi-eikonal shadowing models predicts a strong increase in the fluctuations of local multiplicity, relative to the e - p case, for central impact parameters [91].

Overall, studies of final states in DIS off nuclei, especially at small x, will provide major insights into the dynamics of confinement since they probe the space-time evolution of the process as a function of the length of the target, and they isolate the relative importance of hard and soft physics.

3.2.4 High Density Partonic Matter

A high-energy electron – nucleus collider will provide a remarkable opportunity for exploring the fundamental and universal aspects of QCD. The nucleus, at these energies, acts as an amplifier of the novel physics of high parton densities; aspects of the theory that would otherwise be explored only in an electron - proton collider with energies at least an order of magnitude greater than that of HERA.

High-energy electron scattering off nuclei provides a probe of the "small x" part of the nuclear wave function. In the laboratory frame, x is just the ratio of the longitudinal momentum of a constituent, such as a gluon, to the longitudinal momentum per nucleon. Since the typical momentum of a gluon is at least of the order of the strong interaction scale (Λ_{QCD}~ 200 MeV/c), probing small values of x requires an increase in the energy per nucleon.

At higher and higher energies, smaller and smaller x components add to the nuclear wave function. These components are mainly glue. It is these new components, which change the properties of the nucleus (or nucleon) at higher energies. Therefore, the small x part of the wave function controls the high-energy behavior of hadrons.

There are a number of unsolved problems associated with the high-energy limit of QCD:

- How do hadronic cross sections behave in the high-energy limit? Is their dependence on energy universal?
- How are particles produced?
- How does the total multiplicity depend upon energy?
- How does one compute the gluonic and quark contributions to the hadronic wave function from first principles?
- Is there a universal behavior of hadronic interactions at high energies?

A remarkable consequence of the small x (high energy) limit is that the nucleus looks like a large hadron. When the wavelength of the small x partons is much larger than the Lorentz contracted width of the nucleus (when $x << A^{-1/3}$ in units of the nucleon mass), the partons cannot resolve the structure of the nucleus. This suggests that the behavior of hadrons in the high-energy limit may be universal. We argue later that this universal behavior is associated with a high density of partons. One naturally expects that, at some fixed energy, nuclei will have a higher density of partons than nucleons. This suggests that the universal properties of hadrons at high energy might best be observed in Deep Inelastic Scattering off nuclei. Another reason why the universal limit of high-energy interactions might be more easily observed in nuclei is that edge effects are less pronounced than in other hadrons.

In addition, researchers will also learn more about high-energy hadron-hadron interactions; in particular, understanding the initial conditions for matter produced in high-energy nucleus-nucleus collisions. After the collision takes place, matter evolves through various stages, which includes thermalization and the possible formation of quark-gluon plasma. At the earliest time, the matter is in the quantum mechanical wave functions of the two nuclei. To understand matter at formation and its subsequent evolution requires an understanding of the initial nuclear wave function and its evolution.

At higher energies, the density of small x partons grows. HERA data shows that the density of partons grows as $1/x^{\delta}$ where $\delta \sim 0.3$ for $Q^2 \sim$ few GeV^2. The parton density also grows as we go from nucleons to nuclei. This happens because a high-energy probe

(with $Q^2 >> \Lambda^2_{QCD}$) simultaneously resolves partons from different nucleons along its trajectory. Quantum mechanical coherence indicates that the number of partons per unit area grows as $A^{1/3}$. The density per unit rapidity associated with these partons is

$$Q_S^2 = \frac{1}{\pi R^2}\frac{dN}{dy},$$

where y = ln (1/*x*) is the rapidity. From the above argument of quantum mechanical coherence [70,92,93,94]

$$Q_s^2 = \frac{A^{1/3}}{x^{\delta}}.$$

This equation shows that the density can increase by either increasing A or by decreasing *x*. This simple equation shows that changing a nucleon target to a nuclear target is equivalent to decreasing *x* by at least two orders of magnitude. In other words, nuclei are an efficient amplifier of parton densities. The parton density that would be accessed in an electron-nucleus collision at the EIC would be equivalent to that obtained in an electron-proton collider at energies that are at least an order of magnitude higher than at HERA.

If Q_s is large enough, the strong interaction coupling will become weak: $\alpha_S << 1$. In this limit, QCD is approximately a scale invariant theory. Because the coupling is small, even though there are strong non-perturbative effects, many features of multi-particle production can be computed from first principles in this regime of QCD. It is in this sense that high parton density matter is simple.

Figure 3.22 shows a schematic plot of the ln (1/*x*) and ln (Q^2/Λ^2_{QCD}) plane. In the region of either high Q^2 or large *x,* the high density of partons is not important. Here, "evolution equations" such as DGLAP or BFKL can be used to describe how the parton densities change as one changes Q^2 or ln (1/*x*) respectively.

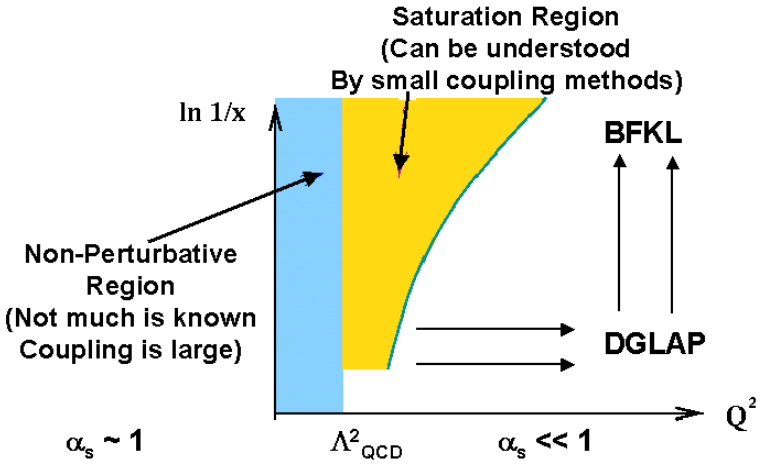

Figure 3.22: Regimes of Applicability of Different Evolution Equations

Schematic diagram of the ln(1/x) – Q^2 plane showing the regimes of applicability of different evolution equations. [95]

If one evolves into the high-density region, these linear evolution equations should be corrected for the high parton density. Indeed, with respect to the ln (1/*x*) evolution, it is not clear that there is an experimental regime where linear evolution can occur without

corrections from the high parton density. The high-density corrections are moderate and perhaps even saturate the growth of parton distributions.

Is there evidence for high parton density effects from existing high-energy hadronic or nuclear experiments? There is evidence from p-A experiments at Fermilab that the typical momenta of partons increases as $p^2_t \sim Q_s^2$. In Figure 2.13**,** the average p_t of Drell - Yan pairs and of J/ψ and Υ particles is shown as a function of the baryon number of the target. However, this result is not conclusive since the magnitude of the p_t broadening is rather small and the experiment probes a kinematic region, which is at rather large *x*. The EIC with access to much smaller x can clarify whether the p_t broadening seen is a genuine high parton density effect. There also are tantalizing hints from HERA that researchers are beginning to see high parton density effects in the regime of Q^2~1-10 GeV^2 and the smallest available *x*. Phenomenological models that contain a saturation scale Q_s^2~1 GeV^2 at x~10^{-4} have been successful in explaining the HERA inclusive, diffractive, and vector meson production data [92]. Model estimates for the EIC give Q_s^2 ~5-10 GeV^2 in a similar *x* range.

3.2.4.1 The Color Glass Condensate

In the high parton density region, the corresponding QCD field strengths squared become $F^2_{\mu\nu} \sim 1/\alpha_S$. Since $\alpha_S(Q_s^2)<<1$, the color field strengths in this regime are large. The non-linearities inherent in the theory are manifest, radically altering the properties of distributions in high-energy collisions.

The saturated gluons in the regime of large field strengths form a Color Glass Condensate (CGC) [70,93,94]. They are colored because gluons carry color charge. The colored fields are disordered since the quark and gluon sources that generate them come from different values of *x,* which are largely uncorrelated. The typical time scale for changes in these sources is long because they are Lorentz time dilated; the sources are moving at high velocities in the laboratory frame. Therefore, the high-density partonic system is exactly like a glass: it is disordered and changes on long time scales, but is frozen on short time scales.

If the gluon density becomes too large, repulsive interactions become important. This density is characteristic of Bose condensates. Quarks, in contrast, are not bosons, and their phase space density is of the order of 1 or smaller. A classical field describes the gluons in the condensate. These fields are the non-Abelian generalization of the Lienard-Wiechart potentials of electrodynamics.

Since the partons at higher momentum scales generate fields at the value of *x* of interest, then on a lower momentum scale, the CGC fields generate additional sources for these lower momentum fields. This suggests that there might be a renormalization group method for computing parton distributions. One successively integrates out fields and replaces them with sources [94]. Significant recent progress has been made in theoretical efforts to understand the high parton density regime [96].

The issue of universality in high-energy hadronic interactions is whether the Colored Glass Condensate renormalization group equations have a fixed point. It is typical of fixed points of renormalization group equations, that their solutions fall into universality classes which are specified only by very generic features of the theory, such as the number of dimensions and internal symmetries. Therefore, it is conceivable that the high-energy limit of QCD is determined by universal, yet non-trivial, properties of the theory.

3.2.4.2 Signatures of the Condensate

There are a number of inclusive and semi-inclusive experimental observables that will be sensitive to new physics in the regime of high parton densities. All the inclusive and semi-inclusive observables studied at HERA can be studied with the EIC with a ZEUS/H1 type detector design. However, it is likely that at the EIC several new observables can be measured for the first time in the small x region. In particular, the EIC will be able to perform semi-inclusive measurements in nuclear DIS well beyond the capabilities of previous fixed target experiments.

3.2.4.2.1 Inclusive Signatures of the Color Glass Condensate

At the luminosities envisaged for the EIC, the structure function $F_2\ (x_{Bj},Q^2)$ and its logarithmic derivatives will be measured with high statistical accuracy. Systematic errors due to uncertainties in radiative corrections need to be quantified. At large Q^2, the logarithmic derivative $dF_2/dln(Q^2)$ is the gluon distribution. As Q^2 decrease, one should see a deviation in the gluon distribution from pQCD fits incorporating DGLAP evolution. In principle, if the Q^2 range is wide enough, there should be a turnover in the distribution around $Q^2 \sim Q_s^2$. A likely remarkable feature of the EIC is direct extraction for the first time of the longitudinal structure function $F_L = F_2 - 2xF_1$. A measurement of F_L provides an independent measure of the gluon distribution. The ratio of F_L / F_T has a very particular behavior in saturation models. Figure 3.23 shows the prediction for this ratio. It has a maximum at a particular Q^2, providing an independent measure of the saturation scale Q_s^2. This maximum grows with increasing nuclear size and decreasing x [97].

A very important inclusive observable is nuclear shadowing. Quark shadowing is defined through the measured ratio of the nuclear structure function to the nucleon structure function: $R_{quark}=F_2^A/AF_2^N$. Gluon shadowing is analogously defined as $R_{gluon}=G^A/AG^N$. Quark shadowing was observed in fixed target experiments (NMC and E665) and gluon shadowing only indirectly through logarithmic derivatives of F_2. However, the gluon shadowing data is at Q^2 of a few GeV^2 where the application of pQCD is unreliable.

There are model calculations based on the information on the gluon induced diffraction at HERA that suggest that gluon shadowing is very large at small x and fairly large Q^2 [71,76] (See Figure 3.17). The EIC will confirm if this is indeed the case. In addition, with and the EIC researchers can determine whether shadowing is entirely a leading twist phenomenon or if there are large higher twist perturbative corrections.

Figure 3.23: The Ratio F_L/F_T vs. Q^2 for Different x

(a) The ratio F_L/F_T as predicted in Ref. [97]. This ratio is plotted as a function of Q^2 for different nuclei and for fixed x_{Bj}. (b) The same ratio for a different value of x_{Bj}.

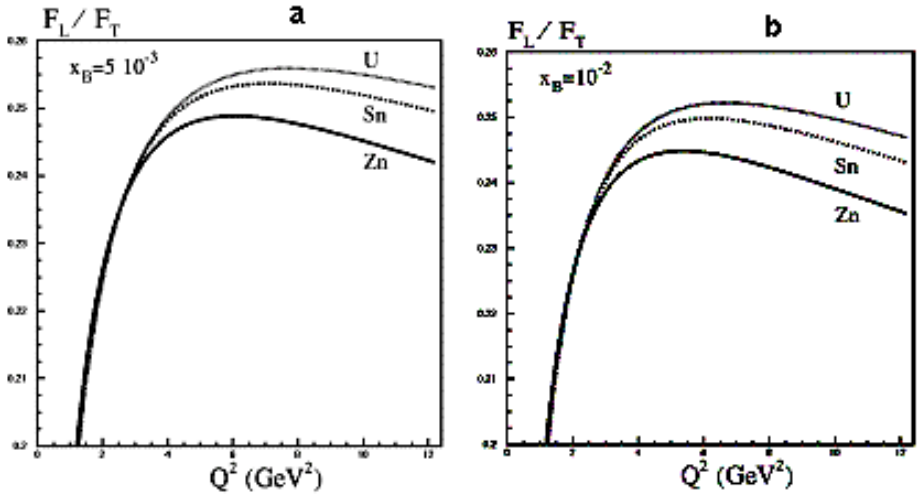

Some saturation models, for instance, predict that perturbative contributions to shadowing will become large as one goes to smaller x [98]. Isolating perturbative from non-perturbative contributions to shadowing will be an interesting theoretical and experimental challenge. Other interesting questions are

- Does shadowing saturate at a particular value of x for a fixed Q^2 and A?
- Does the ratio of quark shadowing to gluon shadowing saturate?

It is well known that there is a close relation between shadowing and diffraction, Figure 3.24.

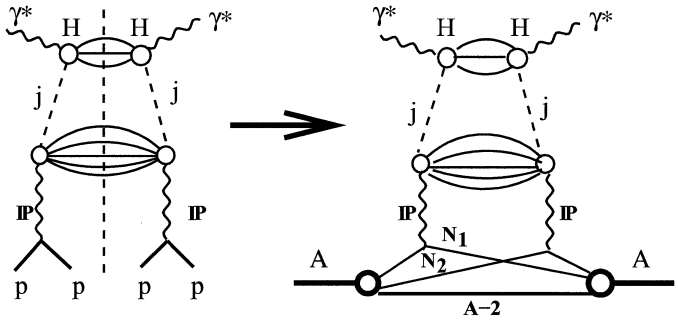

Figure 3.24: Relation between Gluon Induced Hard Diffraction and Leading Twist Contributions

Diagrams [75] demonstrating the relation between gluon induced hard diffraction on protons and the leading twist contribution to nuclear shadowing in DIS.

It is not known whether this relation persists at high parton densities. In an interesting recent exercise, it was shown that diffractive nucleon data at HERA could be used to predict the shadowing of quark distributions that were observed at NMC [99]. Significant deviations from the simple relation between shadowing and diffraction may again suggest the presence of strong non-linearities. At the EIC, the validity of this relation can be explored directly since different nuclear targets will be available. Moreover, the diffractive structure function can be measured independently.

3.2.4.2.3 Semi-inclusive Signatures of the Color Glass Condensate

The most dramatic manifestation of high parton density effects will be in semi-inclusive processes. The most striking of these will be hard diffraction, in which the virtual photon fragments into a final state X with an invariant mass $M_X >> \Lambda_{QCD}$, while the nucleus emerges unscathed from the interaction (Figure 3.25). A striking signal of this would be a large rapidity gap between the fragmentation regions of the electron and the proton. In pQCD, the probability of such a gap is suppressed exponentially.

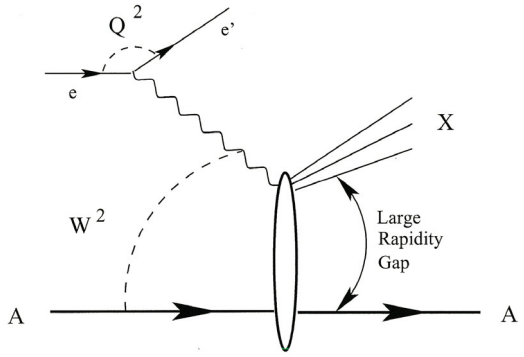

Figure 3.25: Process with a Rapidity Gap Between Systems

Schematic diagram of a process with a rapidity gap between the system X and the nucleus A.

Saturation models for diffraction [100,75] predict that for the EIC, the ratio of the diffractive cross section to the total cross section could be as high as 30% in heavy nuclei. A diffractive structure function, $F^D{}_{A,}$ can be defined rigorously for nuclei. Recent estimates suggest that $F^D{}_L/F^D{}_T$ might also exhibit a maximum as a function of Q^2, whose position increases with decreasing x and increasing Q^2.

An important semi-inclusive observable in e - A DIS at high energies is coherent or diffractive vector meson production. At the EIC, coherent and inclusive vector meson production can be studied for light and heavy vector mesons for a large range in x, Q^2 and the nuclear size A. The forward vector meson diffractive lepton production cross-section off nuclei is given by [41]

$$\left.\frac{d\sigma}{dt}\right|_{t=0} (\gamma_L{}^* A \to VA) \propto \alpha_S^2 x^2 G_A^2(x,Q^2)/Q^6.$$

This quantity is very sensitive to the gluon structure function. The amplitude for diffractive lepton production can be written as a convolution of the $q\overline{q}$ component of the γ^* wave function times the $q\overline{q}$ -nucleus cross-section times the vector meson wave function. In the saturation limit, a semi-hard scale is introduced via the $q\overline{q}$ - A cross-section. Whether this scale is larger or smaller than the scale associated with the size of the vector meson strongly affects the energy, Q^2 and A dependence of the diffractive vector meson cross-sections at small x. In particular, if we assume that the saturation limit coincides with the black body limit for the cross-section ($2\pi R_A^2$) then the Q^2 dependence of the cross-section changes dramatically from $1/Q^6$ to $1/Q^2$. Furthermore one obtains a model independent prediction for the absolute cross-section. [75].

The high parton densities at small x produce large color fluctuations, which are subsequently reflected in large multiplicity fluctuations. For instance, the following phenomena might be expected:

- A broader rapidity distribution in larger nuclei relative to lighter nuclei and protons,
- Rapidity correlations over several units of rapidity; an anomalous multiplicity in one rapidity interval in an event would be accompanied by an anomalous multiplicity in rapidity intervals several units in rapidity away, and
- A correlation of the central multiplicity with the multiplicity of neutrons in a forward neutron detector.

The onset of the CGC regime will manifest itself in a dramatic change of the longitudinal and transverse distributions of the leading hadrons in the current fragmentation region. This will be very different from distributions within the leading twist approximation for both inclusive and diffractive spectra. In particular the leading hadron spectra at large z may be strongly suppressed while production of high p_t jets in coherent diffraction and inclusive scattering will be strongly enhanced [75].

3.2.5 Relation of Physics from the EIC to p-A and A-A Collisions at the Relativistic Heavy Ion Collider (RHIC)

The Relativistic Heavy Ion Collider is currently colliding beams of gold ions at the highest center-of-mass energies of $\sqrt{s} = 200\,\text{GeV/nucleon}$. In the next several years, experiments on proton-proton scattering, proton/deuteron-A scattering, and A - A scattering will be performed for a wide range of center-of-mass energies. In the following, we will discuss some of the novel physics that may be uncovered in these experiments at RHIC (in particular in A - A and p/d - A experiments) and how the EIC will help probe these ideas further.

A goal of the heavy ion experiments is to search for a novel state of matter called the Quark Gluon Plasma (QGP) and to investigate its properties. In general, irrespective of whether a QGP is formed or not, heavy ion collisions will produce large color field strengths immediately after the collision. These large color field strengths likely result from the melting of the Color Glass Condensates (CGC) that characterizes the wave functions of nuclei at high parton densities. Therefore, in principle, heavy ion collisions may provide insight into universal properties of hadronic wave functions at high energies. In particular, there are several topics, where the EIC can help elucidate or complement what we learn from A-A collisions at RHIC about the QGP. Some of these are discussed further and include:

- *Jet Quenching:* Jet quenching has been discussed widely as an important signature of QGP formation [101,102]. The properties of high momentum hadrons traversing a hot QGP may be modified significantly in interactions with a quark gluon plasma. A precise understanding of how their distributions are modified may provide useful information about the properties of the hot matter with which they interact.

- *Saturation of Patron Distributions:* The saturation of parton distributions will significantly affect the properties of final states in heavy ion collisions. In this picture, parton distributions are functions of a saturation scale, Q_s. Final states in heavy ion collisions are sensitive to this scale. Q_s varies with the center-of-mass energy, centrality and atomic number.

- J/ψ *Suppression:* J/ψ suppression was originally suggested as a signal of quark gluon plasma formation since the interactions between heavy quarks would be screened by the QGP.

Jet Quenching: In high-energy heavy-ion collisions, hard partonic scattering can produce energetic partons or jets, which have to traverse the dense partonic matter or quark-gluon plasma before they hadronize. During their propagation in the medium, the produced parton will undergo rescattering with the medium partons. The subsequent radiation will result in energy loss of the jet. This process is referred to as jet quenching. The direct consequence of parton energy loss or jet quenching is the modification of the fragmentation function. Parton energy loss in dense matter is very similar to that in a nucleus. Since the partonic system produced in high-energy heavy-ion collisions has lost its coherence with the initial nuclei, the two-parton correlation that enters in the modified fragmentation factorizes into the initial parton distribution and the parton density in the parton system produced. Therefore, the parton energy loss in heavy-ion collisions is directly proportional to the parton density of the produced quark-gluon medium. Since the parton can undergo multiple rescattering in the medium with a probability that depends on the mean-free-path λ and the thickness of the medium L, the parameter L/λ is a natural expansion parameter for studying parton energy loss. This expansion, known as an opacity expansion, is equivalent to the twist expansion in the DIS problem. For thin plasma, it was shown [102] that the leading contribution of the opacity expansion is sufficient. Since parton energy loss is directly proportional to the parton density in this approximation, its measurement can shed light on the initial condition of the plasma in heavy-ion collisions. The early results from the first year of RHIC experiments [103] show significant suppression of high p_t hadron spectra as predicted by the jet quenching phenomenon. The data indicate a high parton density based on the relationship predicted between parton energy loss and medium parton density. The same measurements in the EIC can provide vital baseline information for comparison between parton energy loss in normal nuclei and dense parton medium in a quark-gluon plasma.

Parton Saturation and Equilibrium: Several models predict that parton distributions will saturate at high energies (or small x and $Q \leq Q_s$). It was predicted that this state is a Color Glass Condensate (CGC). In a high-energy heavy ion collision, the CGC melts producing partons that may subsequently thermalize [103]. The distribution of partons was computed numerically and is proportional to the saturation scale Q_s. A characteristic of the model prediction is that the multiplicity per unit rapidity of hadrons is proportional to $1/\alpha_s(Q_s)$. Since Q_s varies with the centrality of the collision, the multiplicity should vary accordingly. It was argued [105] that the RHIC multiplicity distributions at $\sqrt{s} = 130$ GeV/nucleon [106] are consistent with this expectation. The corresponding distribution at $\sqrt{s} = 200$ GeV/nucleon was predicted [107] and the prediction appears to

be confirmed by recent data [108]. Since the saturation scale depends on the rapidity, the rapidity distributions can be predicted as well. These appear to be confirmed [109]. Additional predictions of the model include m_t scaling [110] of the p_t spectra and predictions for the momentum anisotropy (elliptic flow parameter v_2 [111]). A quantitative analysis of these distributions at present is not available.

One outstanding question in heavy ion collisions is whether the strongly interacting matter formed immediately after the collision (on a time scale $1/Q_s$) equilibrates to form a QGP. Clearly, this depends on the initial conditions [112]. Recently, Baier et al. [113] argued that matter formed from the melting of the CGC is likely to thermalize. They find that the thermalization time and the initial temperature depend on Q_s. Their analysis is most reliable for asymptotically large values of Q_s, so that, for realistic values at RHIC (Q_s ~1 to 2 GeV) the theoretical prediction is less clear.

It is hoped that one can extract the saturation scale *Qs* from the RHIC experiments for a range of center-of-mass energies. However, due to the complexity of final states at RHIC, a precise determination of Q_s will be difficult. Since the EIC is well suited to extract $Q_s(x)$, it will help answer quantitative questions regarding the formation and evolution of the Quark Gluon Plasma.

J/ψ *Suppression*: J/ψ suppression was proposed as a signature of the Quark Gluon Plasma about 15 years ago [114]. The simple yet elegant idea is that the heavy quark-anti-quark potential is screened by light quarks in the plasma. The c and $\bar{c}$ are more likely to go into open charm than into the J/ψ bound state thereby suppressing the number of J/ψ pairs. The dominant mechanism for heavy quark production at high energies is gluon fusion. If initial state gluon shadowing effects in nuclei are important, they also will suppress J/ψ formation. Saturation/higher twist effects on heavy quark production were studied recently for heavy quark pair production in peripheral heavy ion collision and shown to be important [115]. These effects also may mask the effects due to plasma. The EIC, with its potential to perform precision measurements of the nuclear gluon distribution, can clarify the contribution of initial state effects in heavy quark production. Moreover, semi-inclusive experiments at the EIC will enable studies with great precision of effects such as color transparency and color opacity in cold nuclear matter. These will help us understand better and calibrate the final state interactions of heavy quark pairs in hot QCD matter.

We have discussed here a few of the signatures of the Quark Gluon Plasma and High Parton Density matter that may be formed in heavy ion collisions currently underway at RHIC. The EIC is a natural continuation of the RHIC program for studying these collective effects in QCD. The crucial ingredient in many models of heavy ion collisions is the nuclear gluon density. In previous sections, we have pointed out that our understanding of this quantity is very limited in the region of interest. Models at RHIC are hindered by this uncertainty and have to rely on post-dictions and consistency analyses. Thus, in addition to the novel physics that it can explore, the EIC also will help

place on firmer ground many of the insights into QCD gained from heavy ion collisions at RHIC.

A significant aspect of the current RHIC program is to study scattering of protons or deuterons) on a variety of nuclei. These collisions will be at the highest center-of-mass energies ever produced and, since the beam energies and atomic number can be varied, they will produce a wealth of new QCD physics. The p - A program at RHIC was discussed at a BNL workshop in October 2000 [116].

The p - A collisions also will help calibrate the heavy ion experiments on hot QCD matter. For instance, p - A collisions will allow us to extract the nuclear gluon density in a broad x range thereby constraining models of heavy ion collisions. Gluon fusion to jets, vector mesons, open charm and beauty will provide independent constraints on the gluon density. Drell-Yan production will also help calibrate J/ψ suppression in hot QCD matter.

In the discussion on space-time correlations highlights of the p - A physics performed at fixed target experiments were highlighted. In the collider environment at RHIC, novel studies may include studies of hard diffraction, the size and distribution of rapidity gaps with energy and nuclear size, and the first measurement of scaling violations in the Drell - Yan process. Novel saturation effects also can be studied [117,118]. The study of some of these effects may require significant modifications/extensions to the current detectors.

There are some significant differences between the p - A and e - A scattering. In p - A scattering, for instance in the signature Drell - Yan process, it is very hard to reliably extract distributions in the region below the ψ' tail. Thus research is restricted to $Q^2 > 16$ GeV^2. In the x region of interest, saturation effects are probably important at lower $Q^2 \sim$ 5-10 GeV^2. Thus, because of the larger lever arm in Q^2 and x, saturation effects are easier to detect in e - A. While it is difficult in e - A, it does not rule out extracting these effects in p - A.

It will be possible to compare the diffractive parton density in e – A and p – A scattering. The suppression of this density was observed at the Tevetron relative to its value at HERA for a proton target [78]. At the EIC it will be possible to investigate whether this suppression will increase or decrease with A. Clearly this will provide new insights into the dynamics of diffraction in p - p scattering.

3.3 Conclusions

In this section, the unique and outstanding opportunities made possible with the EIC have been described. Important questions, e.g. the spin structure of the nucleon, can be addressed with far greater precision and in a much more comprehensive way than with present or planned experiments. Deep questions, which at present remain inaccessible because of the inadequacies of existing capabilities, become directly tractable with the

EIC. The role of quarks and gluons in understanding atomic nuclei is a prime example. The search for the quark-gluon plasma in ultra relativistic heavy-ion collisions in progress at RHIC and planned at LHC will profit greatly from the EIC. Signatures of this new, deconfined state of matter will involve propagation of partons and hadrons in the nuclear medium. The EIC can provide crucial data by generating such processes using the precisely known electromagnetic interaction. Finally, the EIC will be an ideal facility to look for the predicted Color Glass Condensate phenomenon in strongly interacting matter; its observation would radically alter our understanding of QCD at high energies.

3.4 References

1. Arneodo, M. et al., "Proceedings of Future Physics at HERA, DESY", September 25-26, 1995, [hep-ph/9610423]; "Proceedings of DESY Workshop on Polarized Protons at High Energies", ed. Barber, D., De Roeck, A., Hughes, V.H. and Willecke, S., May 12-20, 1999
2. Bjorken, J. D., *Phys. Rev.* 148, 1467 (1966)
3. Brodsky, S. J., Hoyer, P., Peterson C. and Sakai, N., *Phys. Lett. B* 93, 451 (1980)
4. Melnitchouk, W. and Thomas, A.W., *Phys. Lett. B* 377, 11 (1996)
5. Feynman, R., "Photon-Hadron Interactions", Benjamin, 1972. 282p.
6. Close, F.E., *Phys. Lett. B* 43, 422 (1973)
7. Carlitz, R., *Phys. Lett. B* 58, 345 (1975)
8. Eichten, E., Hinchliffe, I., Lane K. and Quigg, C., *Rev. Mod. Phys*. 56, 579 (1984); Diemoz, M. et al., *Z. Phys*. *C* 39, 21 (1988); Martin, A.D., Roberts, R. and Stirling, W.J., *Phys. Rev. D* 50, 6734 (1994); Lai H.L. et al., CTEQ Collaboration, *Phys. Rev. D* 51, 4763 (1995)
9. Farrar G.R. and Jackson, D.R., *Phys. Rev. Lett*. 35, 1416 (1975)
10. Whitlow, L.W., Riordan, E.M., Dasu, S., Rock S. and Bodek, A., *Phys. Lett. B* 282, 475 (1992)
11. Melnitchouk, W., Schreiber, A.W. and Thomas, A.W., *Phys. Lett. B* 335, 11 (1994)
12. Frankfurt L.L. and Strikman, M.I., *Phys. Rept*. 160, 235 (1988)
13. Whitlow, L.W. et al., *Phys. Lett. B* 282, 475 (1992)
14. Gomez J. et al., *Phys. Rev. D* 49, 4348 (1994)
15. Lichtenstadt, J. "Yale - eRHIC Workshop Proceedings", BNL Report 52592 (2000)
16. Frankfurt L.L. and Strikman, M.I., *Phys. Rept.* 76, 215 (1981)
17. Deshpande, A., "Yale-eRHIC Workshop Proceedings", BNL Report 52592 (2000)
18. Igo, G., "Yale-eRHIC Workshop Proceedings", BNL Report 52592 (2000)
19. Altarelli, G., Ball, R., Forte, S. and Ridolfi, G., *Nucl. Phys. B* 496, 337(1998)
20. Radel, G., "Yale-eRHIC Workshop Proceedings", BNL Report 52592 (2000)
21. Airapentian A. et al., *Phys. Rev. Lett*. 84, 2584 (2000)
22. Cooper-Sarker, A.M., Devenish, R.C.E., and De Roeck, A., *DESY preprint*, 97-226, (1997) [hep/ph/97-226]
23. De Roeck, A., Deshpande, A., Hughes, V., Radel, G. and Lichtenstadt, J., *Eur. Phys. Journal C* 6, 121 (1999)
24. "Proceedings of the 1997 Workshop on Polarized Protons at HERA", eds. De Roeck, A. and Gehrmann, T., DESY-PROC-1998-01
25. Stratmann, M. and Vogelsang, W., "Yale-eRHIC Workshop Proceedings", BNL Report 52592 (2000)
26. Information and code via WWW page http://www3.tsl.uu.se/thep/lepto/
27. Adeva, B. et al., SMC, *Phys. Lett. B* 369, 93 (1996); *Phys. Lett. B* 420, 180 (1998)
28. Ackerstaff, K. et al., HERMES Collaboration, *Phys. Lett. B* 464, 123 (1999)
29. Kobayashi, H., PhD Thesis, Tokyo Institute of Technology (2000).
30. Gluck, M., Reya, E., Stratmann, M. and Vogelsang, W., *Phys. Rev. D* 53 (1996) 4775
31. Gluck, M., Reya, E. and Vogt, A., *Z. Phys. C* 67, 433 (1995)

32. Diakonov, D., Petrov, V.Y., Pobylitsa, P.V., Polyakov, V. and Weiss, C., *Phys. Rev. D* 56, 4069 (1997) [arXiv:hep-ph/9703420]
33. HERMES Collaboration, "The HERMES Physics Program and Plans for 2001-2006," HERMES Report No. 00-003 (2000)
34. Contreras, J., Private communication, to be published; Contreras, J. and De Roeck A., *DESY-PROC*-1998-01
35. Grosse-Perdekamp, M. "Yale-eRHIC Workshop Proceedings", BNL Report 52592 (2000)
36. Frankfurt, L.L., Pobylitsa, P.V., Polyakov, M.V. and. Strikman, M.I., *Phys. Rev. D* 60, 014010 (1999)
37. Dittes, F.M., Muller, D. Robaschik, D., Geyer, B., Horejsi, J., *Phys. Lett. B* 209, 325 (1988)
38. Ji, X., *Phys. G* 24, 1181 (1998); Ji, X*., Phys. Rev. Lett.* 78, 610 (1997); Ji, X., *Phys. Rev. D* 55, 7114 (1997)
39. Radyushkin, A. V., *Phys, Lett. B* 380, 417 (1996); Radyushkin, A. V., *Phys. Rev. D* 56, 5524 (1997)
40. Collins, J.C. and Freund, A., *Phys. Rev. D* 59, 074009 (1999) [arXiv:hep-ph/9801262]
41. Brodsky, S.J., Frankfurt, L., Gunion, J.F., Mueller, A.H., Strikman, M., *Phys. Rev. D* 50, 3134 (1994)
42. Collins, J., Frankfurt, L. and Strikman, M., *Phys. Rev. D* 56, 2982 (1997)
43. Jain, P. and Ralston, J.P., "Proceedings of the Workshop on Future Direction in Particle and Nuclear Physics at Multi-GeV Beam Facilities", BNL (1993)
44. Radyushkin, A.V; [arXiv:hep-ph/0101225]
45. Petrov, V.Y., Pobylitsa, P.V., Polyakov, V., Bornig, I., Goeke, K. and Weiss, C., *Phys. Rev. D* 57, 4325 (1998) [arXiv:hep-ph/9710270]
46. Belitsky, A.V., Müller, D., Niedermeier, L. and Schäfer, A., *Phys. Lett. B* 437, 160 (1998); *Nucl. Phys. B* 546, 279 (1999); *Phys. Lett. B* 474, 163 (2000) [hep-ph/0004059]
47. Diehl, M., Gousset, T., Pire B. and Ralston, J.P., *Phys. Lett. B* 411, 193 (1997)
48. Polyakov, M.V. and Weiss, C., *Phys. Rev. D* 60, 114017 (1999); Diehl, M., Feldmann, T., Jakob R. and Kroll, P., *Phys. Lett. B* 460, 204 (1999); Vanderhaeghen, M., Guichon, P. and Guidal, M., *Phys. Rev. D* 60, 094017 (1999)
49. Frankfurt, L.L., Polyakov, M.V., Strikman, M. and Vanderhaeghen, M., *Phys. Rev. Lett.* 84, 2589 (2000) [arXiv:hep-ph/9911381]
50. Goeke, K., Polyakov M.V. and Vanderhaeghen, M., *Prog. Part. Nucl. Phys*. 47, 401 (2001) [arXiv:hep-ph/0106012].
51. ZEUS Contributions to Europhysics Conference 2001, 548, 594
52. Polyakov, M.V., *Nucl. Phys. B* 555, 231 (1999) [arXiv:hep-ph/9809483]; Clerbaux, B. and. Polyakov, V., *Nucl. Phys. A* 679, 185 (2000)
53. Munier, S. J., Stasto A.M. and Mueller, A.H., *Nucl. Phys. B* 603, 427 (2001) [arXiv:hep-ph/0102291]
54. Fadin, V.S., Kuraev, E.A. and Lipatov, L.N., *Phys. Lett. B* 60, 50 (1975); Balitsky, I. and Lipatov, L.N., *J. Nucl. Phys*, 28, 822 (1978)
55. Mulders, P., [hep-ph/0010199]
56. Trentadue, L. and. Veneziano, G., *Phys. Lett. B* 323, 201 (1994)

57. Collins, J.C., *Phys. Rev. D* 57, 3051 (1998) [Erratum-ibid. *D* 61,019902 (1998)] [arXiv:hep-ph/9709499]
58. Grazzini, M., Trentadue, L. and Veneziano, G., *Nucl. Phys. B* 519, 394 (1998) [arXiv:hep-ph/9709452]
59. Frankfurt, L., Koepf, W. and Strikman, M., *Phys. Lett. B* 405, 367 (1997) [arXiv:hep-ph/9702236]
60. Sullivan, J.D., *Phys. Rev. D*, 1732 (1972)
61. Strikman, M.I. and Frankfurt, L.L., *Yad. Fiz*. 25, 1177, 21 (1977)
62. Strikman, M., "Proceeding of Workshop on Internal Spin Structure of the Nucleon", January 1994, pp. 153-166, World Scientific 1995, eds. Hughes, V.H and Cavata, L.
63. Hecht, M.B., Roberts, C.D. and Schmidt, S.M., nucl. – th/0008049
64. Shigetani, T., Suzuki, K., and Toki, H., *Phys. Lett. B* 308, 383 (1993); Davidson, R.M. and Ruiz Arriola, E., *Phys. Lett B*. 348, 163 (1995)
65. Best, G. et al. , *Phys. Rev. D 56*, 2743 (1997)
66. Conway, J.S.et al., Phys.Rev. D39, 39 (1989).
67. Pillar, G. and Weise, W., *Phys. Rept*. 330, 1 (2000)
68. Gribov, L.V., Levin, E.M., and Ryskin, M.G., *Phys. Rept*. 100, 1 (1983)
69. Mueller, A.H. and Qiu, J.*, Nucl. Phys. B* 268, 427 (1986); Mueller, A.H., *Nucl. Phys. B* 335, 115 (1990)
70. McLerran, L. and Venugopalan, R., *Phys. Rev. D* 49, 2233 (1994); ibid., 3352; *D* 50 2225 (1994); Kovchegov, Y.V., *Phys. Rev. D* 54, 5463 (1996); Jalilian-Marian, J., Kovner, A., McLerran, L. and Weigert, H., *Phys. Rev D* 55, 5414 (1997)
71. Frankfurt, L., and Strikman, M.*, Eur. Phys. J. A* 5, 293 (1999) [arXiv:hep-ph/9812322]
72. Collins, J.C., [arXiv:hep-ph/0107252].
73. Abramowicz, H. and Caldwell, S., *Rev. Mod. Phys*. 71, 1275 (1999)
74. Gribov, V.N., *Sov. Phys*. 29, 483 (1969)
75. Frankfurt, L., Guzey, V. and Strikman, M., *J. Phys. G* 27, R23 (2001)
76. Sloan, T., "Yale-eRHIC Workshop Proceedings", BNL Report 52592 (2000)
77. Arneodo, M. et al. New Muon Collaboration, *Nucl. Phys. B* 481, 3, (1996)
78. Alvero, L., Collins, J.S., Terron, J. and Whitmore, J.J., *Phys. Rev. D* 59, 074022 (1999)
79. Melnitchouk, W., Sargsian, M. and. Strikman, M.I., *Z. Phys. A* 359, 99 (1997) [arXiv:nucl-th/9609048]
80. Pirner, H. J. and. Vary, J. P., *Phys. Rev. Lett*. 46, 1376 (1981); Carlson, C. E. and Havens, T.J., *Phys. Rev. Lett*. 51, 261 (1983); Horlacher, G., and Arenhovel, H., *Nucl. Phys. II* 300, 348 (1978).
81. Strikman, M.I. and Frankfurt, L.L., "Proceedings of Les Houches School on Nuclear Physics", p.305-321, February 1990, eds. Desplanques, B. and Goutte, D., Les Houches Publishers, NY (1991).
82. Suzuki, K., *Phys. Lett. B* 368, 1 (1996).
83. Brown, G.E. and Rho, M., *Phys. Rev. Lett. 66*, 2720 (1991)
84. Holt, R J. and Reimer, P.E., "Proceedings of the Second International Workshop on the Electron-Polarized Ion Collider", MIT, 2000

85. Frankfurt, L., Pillar, G., Sargasian, M. and Strikman, M., *Eur. Phys. J. A* 2, 301 (1998) [arXiv:nucl-th/9801041]
86. Aitala. E.M et al., E791 Collaboration, *Phys. Rev. Lett.* 86, 4773 (2001) [arXiv:hep- ex/0010044]
87. Guo, X.F. and Wang, X.N., *Phys. Rev. Lett*. 85, 3591 (2000) [arXiv:hep-ph/0005044]; Wang, X.N. and Guo, X.F., *Nucl. Phys. A* 696, 788 (2001) [arXiv:hep-ph/1002230]
88. Airapetian A. et al., HERMES Collaboration, *Eur. Phys. J. C* 20, 479 (2001) [arXiv:hep-ex/0012049]
89. Naples, D. et al., E683 Collaboration, *Phys. Rev. Lett*. 72, 2341 (1994)
90. Nikolaev, N.N., *Sov. Phys. Usp*. 24, 531 (1981) [*Usp. Fiz. Nauk* 134, 369 (1981)]
91. Frankfurt, L. and Strikman, M., *Phys. Rev. Lett. B* 382, 6 (1996)
92. Golec-Biernat, K. and Wusthoff, M., *Phys. Rev. D* 59, 014017 (1999); ibid. 60, 114023 (1999); Caldwell, A.C., and Soares, M. S.[hep-ph/0101085]
93. Iancu, E., Leonidov, A. and McLerran, L., *Nucl. Phys. A* 692, 583 (2001); *Phys. Lett. B* 510, 133 (2001); ibid. 145 (2001)
94. Jalilian-Marian, J., Kovner, A., McLerran, L. and Weigert, H., *Phys. Rev. D* 55, 5414 (1997); Jalilian-Marian, J., Kovner, A., Leonidov, A. and Weigert, H., *Nucl. Phys. B* 504, 415 (1997); Jalilian-Marian, J., Kovner, A. and Weigert, H., *Phys. Rev. D* 59, 014015 (1999)
95. Figure Courtesy Kovchegov, Y.
96. Balitsky, I. *Nucl. Phys. B* 463, 99 (1996); *Phys. Rev. D* 60, 014020 (1999); Kovchegov, Y., *Phys. Rev. D* 60, 034008 (1999); *Phys. Rev. D* 61, 074018 (2000); Weigert, H. [hep-ph/0004044]; Ferrerio, E., et al., [hep-ph/0109115]; Levin, E. and Tuchin, K., *Nucl. Phys. B* 573, 833 (2000); Braun, M., [hep-ph/0101070]; Mueller, A.H., *Nucl. Phys. B* 558, 285 (1999)
97. Gotsman, E., Levin, E., Maor, U., McLerran, L. and Tuchin, K. [hep-ph/0008280]; [hep-ph/0007258]; Goncalves, V.P., *Phys. Lett. B* 495, 303 (2000)
98. Jalilian-Marian J. and Wang, X.N., *Phys. Rev. D* 60, 054016 (1999)
99. Capella, A. et.al., *Eur. Phys. J. C* 5, 111 (1998)
100. Kovchegov, Y. and McLerran, L. *Phys. Rev. D* 60, 054025 (1999); ibid., *D* 62, 0019901 (2000); Buchmuller, W., Gehrmann, T. and Hebecker, A., *Nucl. Phys. B* 537, 477 (1999)
101. Wang, X. N., Gyulassy, M. and Plumer, M., *Phys, Rev, D* 51, 3436 (1995)
102. Gyulassy, M., Levai P. and Vitev, I., *Phys, Rev, Lett*. 85, 5535 (2000); Wiedemann, U., *Nucl. Phys. A* 690, 731 (2001); Baier, R., Schiff, D. and Zakharov, B., *Ann. Rev. Nucl. Part. Sci.* 50, 37 (2000)
103. Adcox, K. et al. PHENIX Collaboration, *Phys. Rev, Lett*. 88, 022301 (2002)
104. Kovner, A., McLerran L.D and Weigert, H., *Phys, Rev. D* 52, 3809 (1995); *ibid.* 6231 (1995)
105. Kharzeev, D. and Nardi, M., *Phys. Lett. B* 507, 121 (2001)
106. Adler, C. et al., STAR, Collaboration, *Phys. Rev. Lett. 87*, 112303 (2001); Milov, A., PHENIX Collaboration, *Nucl. Phys. A* 698, 171 (2002)
107. Kharzeev, D. and Levin, E., [arXiv:nucl-th/0108006]
108. Back B.B. et al., PHOBOS Collaboration, *Phys. Rev. Lett*. 88, 022302 (2002)
109. Bearden G. et al., BRAHMS Collaboration, [arXiv:nucl-ex/0112001]

110. Schaffner-Bielich, J., Kharzeev, D., McLerran, L.D. and Venugopalan, R. [arXiv:nucl-th/0108048]
111. Krasnitz, A., Nara, Y. and Venugopalan, R. to be published
112. Krasnitz A. and Venugopalan, R., Plenary talk at "15th International Conference on Ultra relativistic Nucleus-Nucleus Collisions (QM2001)", Stony Brook, New York, 15-20 Jan. 2001, [arXiv:hcp-ph/0104168]; Krasnitz, A., and Venugopalan, R., *Phys. Rev. Lett.* 84, 4309 (2000); Krasnitz, A., Nara, Y. and Venugopalan, R., *Phys. Rev. Lett.* 87, 192302 (2001)
113. Baier, R., Mueller, A.H., Schiff, D. and. Son, D. T., *Phys, Lett. B* 502, 51 (2001)
114. Matsui, T. and Satz, H., *Phys. Lett. B* 178, 416 (1986)
115. Gelis F. and Peshier, A., [arXiv:hep-ph/0107142]
116. "Proceeings of the p - A Workshop at BNL", eds. Aronson, S. and Peng, J.C., BNL, October 2000
117. Kovchegov, Y. V. and Mueller, A. H., *Nucl. Phys. B* 529, 451 (1998)
118. Dumitru, A. and McLerran, L. D. [arXiv:hep-ph/0105268]

4.0 Accelerator Design

4.1 Overview

In this Section, we describe electron-proton/ion colliders with center-of-mass energies between 14 GeV and 100 GeV (protons) or 63 GeV/A (ions), luminosities at 10^{33} cm^{-2} s^{-1} and polarized electron and proton beams.

Achieving the luminosity goal of 10^{33} cm^{-2} s^{-1} is technically challenging but attainable with improvements in current accelerator technology and additional R&D in some areas, principally in the development of high-energy electron cooling of ion beams. Electron cooling is the key technology for reaching the luminosity goal at low proton energies (< 50 GeV).

Two collider configurations are considered: a conventional electron ring/proton ring option and several electron linac/ion ring options. The ring-ring concept, presented in Section 4.2, involves well-proven technology with machine and beam parameters achieved at other storage rings. The linac-ring concept is presented in Section 4.3. This concept was first proposed for the B-factory but was not competitive with a ring-ring design without linac energy recovery. With the recent demonstration and continuing development of energy recovery in recirculating linacs, the electron linac-ion ring scenario is viable and offers some potential advantages over the ring-ring scenario, particularly for high-energy schemes such as eRHIC.

The machine designs presented here are preliminary proposals, and the brief outlines of the machine concepts are condensations of more detailed conceptual design reports prepared by the respective design groups.

Both collider concepts still need to address a number of outstanding accelerator physics and technology issues before such facilities are designed and built. These issues are identified in the respective machine concept Sections 4.2 and 4.3. For the ion ring, essentially common to both collider scenarios, the foremost technical R&D task is to develop and demonstrate a high-energy electron cooling system. This is discussed in detail in Section 4.4. For the electron linac scheme, the principal technological challenge requiring significant R&D is the construction of a high average current polarized electron source at high electron polarization. It is essential that the required resources (facilities, manpower, funding) for these major R&D efforts be made available early in the collider project schedule.

Some preliminary thoughts on concepts and problems of the interaction region design are presented in Section 4.5. Much more interactive discussion of this important topic between machine designers and experimenters/detector designers needs to continue in order to make further progress especially in the machine design.

Finally, the accelerator designers need answers to a number of crucial questions. The answers will fundamentally influence the accelerator design:

- Is the center-of-mass energy of approximately 15-30 GeV the right magnitude for a "Greenfield" collider not based on RHIC?
- Is the center-of-mass energy ratio of about 2 sufficient?
- Is the proton/electron energy ratio of ~5-10 appropriate? Does this ratio need to change in the course of an experiment?
- Is the 150-200 MHz bunch collision frequency (5-6 ns bunch spacing) acceptable for the detectors, since lower frequency means lower luminosity?

4.2 Electron Ring On Proton Ring Colliders

4.2.1 The Low Energy Green Field Option

The following design goals were chosen for an electron-proton collider:

- Center of mass energy: 15-30 GeV
- Proton - electron energy ratio: 4-5
- Luminosity: $\geq 10^{33}$ cm^{-2} s^{-1}
- Head-on collision at two Intersecting Points (IP)
- Longitudinal electron and proton polarizations at IP.

Collaborators at the Budker Institute of Nuclear Physics in Novosibirsk in conjunction with the MIT/Bates Laboratory [1] worked out a concept for a ring-ring collider that fulfills the stated design goals. The following is a brief summary of this study and focuses primarily on achieving a high luminosity and a high degree of polarization for both colliding beams. Many conventional technical aspects of the collider have been worked out conceptually but are beyond the scope of this report.

4.2.1.1 Beam Parameters and Luminosity

The beam energies in the present design were chosen to vary simultaneously between 3.5 and 7 GeV for the electrons and between 16 and 32 GeV for the protons, maintaining an energy ratio of about 4.6. An alternative 5 GeV on 50 GeV (nominally) electron-proton collider would differ from the present 7-on-32 GeV design primarily in technical details.

The following well-known relation can describe the luminosity for electron-proton collision in terms of the most important limiting beam parameters for round Gaussian beams.

$$L = f_{coll}\frac{N_e N_p}{4\pi\sigma^2} = \frac{4\pi}{r_e r_p}\times\gamma_e\left(\gamma_p\beta_p\right)\times f_{coll}\times\frac{\varepsilon}{\beta}\times\xi_e\times\xi_p$$

In this expression

f_{coll} = bunch collision frequency = orbital frequency x number of bunches

N_e, N_p = number of particles (electrons, e, and protons, p) per bunch

σ = root-mean-square beam radius at the Interaction Point (IP)

$\beta = \beta -$ function at IP

ε = beam emittance (This is the same for electron and proton beam.)

ξ_e, ξ_p = space charge parameters (beam-beam tune shifts)

r_e, r_p = classical electron and proton radius

γ_e, γ_p = relativistic (-factors

β_p = proton beam velocity /c

Limits on N_e and N_p are given by bunch instabilities. For electrons, the most severe intensity threshold is set by the head-tail transverse mode-coupling instability. Experience at LEP and the B-factories have shown achievable values of $N_e = 3\times10^{10}$. For protons, experimental results from BNL and FNAL show attainable values of $N_p = 10^{11}$. Practically obtainable beam-beam parameter values of

$$\xi_e = N_p r_e/(4\pi\gamma_e\ \varepsilon)\ \bullet\ 0.04$$

$$\xi_p = N_e r_p/(4\pi\gamma_p\ \beta_p\varepsilon)\bullet\ 0.003,$$

were demonstrated in $e^+ e^-$ colliders (B-factories) and e - p colliders. These were limited by beam-beam instabilities. At such values for ξ_p, computer simulations showed that for the VEPP-2M collider, round beams symmetric in x and y, are more stable against beam blow-up and eliminate x-y betatron coupling in the arcs. From these considerations, the transverse beam parameters were chosen equal in x and y with values of σ = 65 :m, ε = 5 x 10^{-8} m, and β = 0.1 m. To reach a luminosity of $L = 10^{33}\text{cm}^{-2}\text{s}^{-1}$ requires a collision frequency of f_{coll} = 200MHz, resulting in beam currents of I_e=*1*A, I_p = 3.2A.

4.2.1.2 Ring - Ring Collider Layout

The machine layout in Figure 4.1 shows two racetrack-shaped rings of 1387 m in circumference. There are two long straight sections (LS) providing for two interaction points (IP) on opposite sides of the racetrack and containing spin rotators, two short straight sections (SS) for injection, RF, etc, and four arcs. The electron-proton energy ratio results in a convenient ratio of magnetic guide fields for same-size rings in a single tunnel.

In the electron-ring, arcs and SS lie above the proton-ring plane. They carry a vertically polarized beam. In the LS, the electron beam merges with the proton ring at one IP in each LS. The polarization is made longitudinal at the IP by solenoidal spin rotators and horizontal-bend dipoles that go into the interaction region, and restored to vertical by a mirror-symmetric insertion coming out of the interaction region.

In the proton-ring, the polarization stays in the ring plane. Siberian snakes in one of the LS maintain longitudinal polarization in the opposite LS. At the IP in the first LS, the polarization is also longitudinal between the two half-snakes at "magic" proton energies occurring at intervals of 0.523 GeV (where the spin rotation is an integral multiple of the momentum rotation). Thus, at these magic proton energies, both electron and proton polarizations are longitudinal in both IP's.

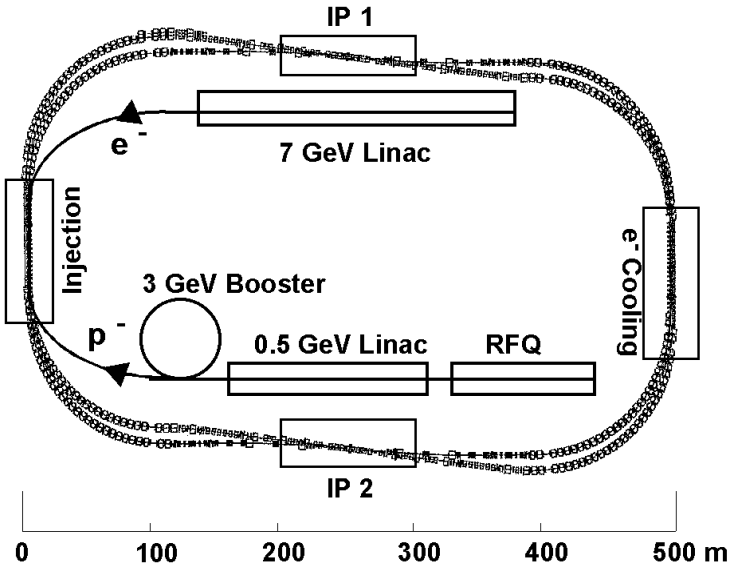

Figure 4.1: Layout of the e - p Collider Rings.

4.2.1.3 Beam Polarization Maintenance

Electron polarization is stable in the arcs and SS since the equilibrium spin axis is vertical. The LS and IP regions where the polarization is not vertical were carefully designed for optimal spin transparency to minimize depolarization. In Section 4.2.1.5 we discuss ways of establishing the polarization of the stored electron beam.

In the proton ring, full Siberian snakes avoid all integer and intrinsic resonances by maintaining a spin tune of ½. Therefore, minimal depolarization is expected when the proton-ring is ramped up in energy after injecting polarized protons at low energy. Helical-dipole snake designs to minimize orbit excursions of the proton beam within the snake at injection energy are under consideration.

4.2.1.4 Beam Cooling

While the electron beam cools by synchrotron radiation, the proton emittance grows by intra-beam scattering. Calculated diffusion times, τ_{δ} for the momentum spread and τ_{x} for the transverse emittance, are given below.

$$\tau_{\delta} \cong 1500\, s$$
$$\tau_{x} \cong 8000\, s$$

Without cooling, τ_{δ} is too short for a meaningful storage time. The proposed (but as yet technically unproven) solution is electron cooling of the proton beam using a recirculating-linac-type cooler (8-16 MeV electrons for 16-32 GeV protons) described in Section 4.4. The collider luminosity is likely to be limited to ~1/10 of the design goal of 10^{33} cm^{-2} s^{-1} without cooling of the stored proton beam

4.2.1.5 Collider Beam Injection

Polarized protons from a state-of-the-art optically-pumped polarized H^- source, providing 10mA pulses of 150 μs duration, would be accelerated by a 0.3 GeV linac and a 4 GeV booster ring delivering $6\times10^{12}\,\vec{p}$ in 60 bunches for $10^{11}\,\vec{p}$ / bunch to the collider proton ring per booster cycle [2]. Operating the booster at 2Hz it takes 8 seconds to fill the proton-ring, which is then ramped up to 16-32 GeV using Siberian snakes to maintain polarization. The choice of a 4 GeV Booster energy minimizes the number of intrinsic depolarization resonances encountered in the Booster while keeping the orbit excursions within the main-ring snakes at acceptable values during injection.

Polarized electrons can be provided in one of two ways:

- A Bates-type polarized electron source can feed 10 mA pulses of 4.5 μs duration into a 3.5 to 7 GeV linac. Stacking this full-energy beam into the electron-ring at 10 Hz requires a 10-second fill time to obtain 3×10^{10} electrons per bunch. Technically, this scheme is straightforward but requires an expensive linac (which could provide beam to other users between ring fills).
- Alternatively, unpolarized electrons from a 0.5 - 1 GeV linac could be stacked in the electron ring and then accelerated to 3.5 - 7 GeV by ramping the electron-ring. At the final energy, spontaneous Sokolav-Ternov Polarization (STP) would polarize the beam. Polarization time and equilibrium polarization, calculated with the ASPIRRIN code, are shown in Figure 4.2. While the polarization time at 7 GeV is an acceptable 2000 seconds, it is 10^5 seconds at 3.5 GeV for an unmodified electron-ring. In an elegant scheme, "dog-legs", i.e. three-magnet chicanes in the electron-ring arcs, could be introduced to act as "wigglers" to reduce the 3.5 GeV polarization time by a factor of 40. At the same time, these "dog-legs" would increase the electron orbit length to maintain synchronization with the slower proton beam at lower energies, something that would be needed in any scheme. The corresponding increase in RF power by a factor of 9 to maintain beam life time at 3.5 GeV would still be less than the RF

power required for 7 GeV without the wigglers. Therefore it appears feasible to achieve an equilibrium STP of about 80% and polarization times of half an hour for the entire energy range of the electron-ring.

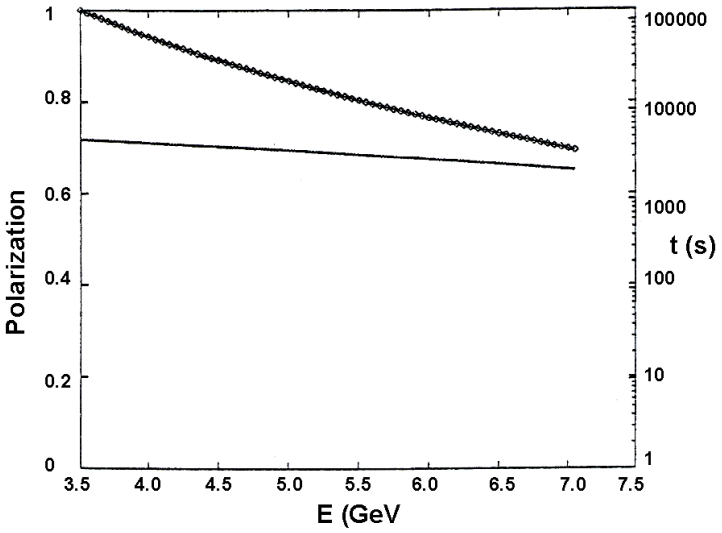

Figure 4.2: Self–polarization of Electrons

Numerical results of STP times (top curve) and equilibrium polarization (bottom curve) for the e-ring without wigglers.

4.2.1.6 Required Research and Development

Two main areas require substantial R&D work; the linac-type electron cooler and the layout of the IP region integrated into the detector systems. Both of these issues are addressed in separate Sections (4.4 and 4.5) of this document.

Less crucial but nevertheless important would be a test of STP at 3.5 GeV using wigglers. This would have to be proven if one wants to avoid the high cost of a full-energy electron injection linac. The Bates South Hall Ring, upgraded to ramp the beam-energy to 3.5 GeV, could be a very cost-effective test bed for STP. As a first step, ramping to 1.5 GeV requiring little RF boosting is possible using a Siberian Snake. This keeps the polarization axis in the horizontal plane. Measurement with the snake turned on or off would provide a detailed test of the STP theory.

4.2.1.7 Conclusions

Based on a conceptual design by the Budker Institute and their extensive experience, a ring-ring e - p collider varying from 3.5 on 16 GeV to 7 on 32 GeV (15 - 30 GeV center-of-mass energy) with a luminosity of 10^{33} $cm^{-2}s^{-1}$ seems feasible using existing and demonstrated technologies, with the exception of high-energy electron cooling. Higher luminosities approaching 10^{34} $cm^{-2}s^{-1}$ can be achieved with vigorous R&D efforts and future machine upgrades.

4.2.2 The High Energy eRHIC Ring-Ring Option

RHIC accelerates and stores bunches of heavy or light ions, typically gold or protons, in two horizontally separated superconducting rings. Head-on collisions occur at six interaction points (IPs). Collisions between like species are the normal mode of operation, but RHIC can store and collide two beams with very different rigidities. However, it is not practical to store electrons in one of the two superconducting rings because of the unacceptable cryogenic heat load incurred when even a small electron current is present. If electrons are stored in the RHIC tunnel, then a third ring must be constructed [3, 4].

In the ring-ring collisions scenario, 10 GeV electrons circulate in a third storage ring in the RHIC tunnel. This is illustrated in Figure 4.3. Pre-polarized electrons are injected at full energy in the counterclockwise direction at IP4. Collisions are possible with the clockwise rotating ions at the other five interaction points. The natural place to install the electron ring magnets is just above the floor of the tunnel; between the magnet stands of the two ion rings. Table 4.1 summarizes the primary parameters for the eRHIC concept.

Table 4.1: The Primary eRHIC Parameters

Gold at energy per nucleon	100 GeV/u
Proton top energy	250 GeV
Electron energy	10 GeV
Electron-Gold CM energy per nucleon	63 GeV/u
Electron-proton CM energy	100 GeV
Circumference	3833 m
Revolution frequency f_{rev}	78.3 KHz
Arc dipole bend radius	243 m

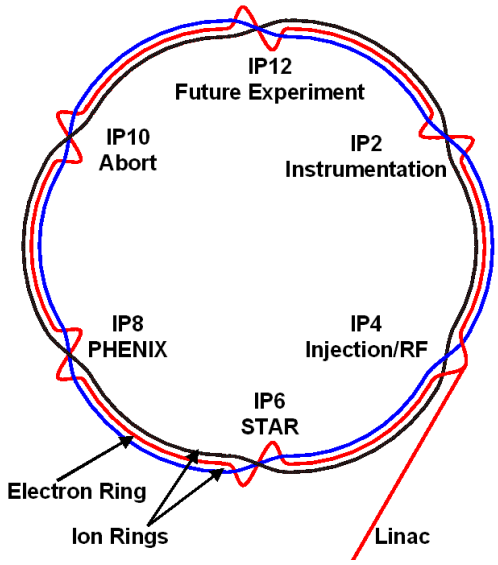

Figure 4.3: Ring - Ring Collision Scenario

Schematic layout of the injection linac, electron ring and the two ion rings.

4.2.2.1 Luminosity Performance at the Beam-Beam Limit

The luminosity may be written in a parameterization that is useful when the luminosity performance is simultaneously limited, or nearly limited, by beam-beam effects and by interaction region optics, since then the values of ξ and σ'^{*} are well known.

$$L = f_{eoll}\xi_{\varepsilon}\xi_{i}\sigma'^{*}_{\varepsilon}\sigma'^{*}_{i}\frac{(4\pi\gamma_{e}\gamma_{i})}{r_{e}r_{i}}.$$

The interaction region optics constrain the maximum angular beam size at the interaction point:

$$\sigma'^{*} = \frac{\sigma^{*}}{\beta^{*}} \leq \frac{1}{n}\frac{a}{d}.$$

In this expression n ($\approx$ 6 for ions and $\approx$12 for electrons) is the number of beam sigmas which must fit in a, the aperture of the interaction region quads. The "effective" aperture distance, d, is almost independent of the value of β^{*} in the interaction region optics.

Number of Bunches: If the beam-beam parameters and the angular beam sizes are already at their limits, the only way to raise the luminosity is to increase the collisions frequency f_{coll}, by increasing the number of bunches. Table 4.2 shows the ultimate performance of an eRHIC ring-ring collider, when the number of bunches is either 360 or 2520 [3,4]. One constraint on the number of bunches is the maximum average beam current. Another is the need for minimum bunch spacing – perhaps due to the electron cloud effect, or due to a minimum reset time for detector electronics. In an electron ring the average current may be limited by the total synchrotron radiation load, or by the heat load per meter. In a superconducting ion ring the beam image current, which flows in the vacuum chamber walls, is a resistive heat load at cryogenic temperatures. A maximum average cryogenic heat load of about 1 W/m can be tolerated, to stay within the capacity of typical cryogenic systems. Beam Position Monitor signal cables may suffer unacceptably large cold-to-warm heat loads, due to resistive heating by the signal current when the number of bunches becomes large and the bunches are too short [3].

Long Range Beam-Beam: It is relatively easy to protect the Electron Ion Collider against parasitic long-range beam-beam interactions by arranging the early separation of the two beams with very unequal rigidities. In standard RHIC optics the beams are magnetically separated at only 9.8 meters from the interaction point, before entry into the first quadrupole, and after only one parasitic interaction when 360 bunches are stored.

4.2.2.1.1 Ion Storage Ring Issues

Electron Cloud Effect: Electrons produced by ionization of the residual gas are accelerated by the electrical field of the next passing ion bunch, and eventually hit the vacuum chamber wall, emitting secondary electrons. This process can "runaway" if the bunches are spaced too closely, driving a large cryogenic heat load in a superconducting ion ring, and perhaps causing instabilities. The effect was studied extensively for the LHC, where the nominal bunch spacing is 25 ns and there are nominally about 10^{11} protons per bunch [5,6,7]. In fixed target mode the Tevatron routinely operates with 1008 bunches of approximately 2 x 10^{10} protons spaced by about 18.9 ns (53 MHz), without undue cryogenic difficulty. Bunch gaps, such as the 1 μs abort gap in the Tevatron, act to clear the electron clouds. Unfortunately there is very little hard experimental data from existing cryogenic accelerators with closely spaced bunches. Preliminary indications from the 2001 RHIC collider run suggest that the electron cloud effect currently prevents RHIC from operating with 120 bunches at design intensities of

10^9 gold ions per bunch. There is good reason to expect that this limit can be overcome with additional clearing gaps, with modest solenoidal fields in the warm vacuum sections, or even with warm vacuum pipe coatings. This problem needs more investigation, especially by making careful measurements on cryogenic storage rings, not only RHIC, but also HERA and the Tevatron.

Table 4.2: Electron-Gold and Polarized Electron-Proton Collisions.
(The maximum practical number of bunches is in the range from 360 to 2520. Electron cooling is assumed)

Ion Specie	**Protons**	**Protons**	**Gold**	**Gold**
Number of bunches, N_b	**360**	**2520**	**360**	**2520**
Luminosity L [10^{32}cm^{-2}s^{-1}]	3.5	24.3	0.086	0.61
Bunch spacing [ns]	35.5	5.1	35.5	5.1
RMS beam size, σ^* μm	40	40	50	50
Ion Parameters				
Ion emittance, norm. RMS mm mrad	0.8	0.8	1.0	1.0
Ions per bunch, N_i [10^{11}]	0.94	0.94	0.012	0.012
Ion average current, [A]	0.42	2.97	0.42	2.97
Ion IP beta, β_e^* [m]	0.53	0.53	0.27	0.27
Ion angular beam size, $\sigma_i'^*$ μr	75	75	186	186
Ion bunch Length, [m]	0.1	0.1	0.2	0.2
Ion beam-beam parameter, ξ_i	0.004	0.004	0.004	0.004
Laslett space charge tune shift ΔQ	0.003	0.003	0.003	0.003
Electron Parameters				
Electron emittance, [mm μrad]	18	18	18	18
Electrons per bunch, N_e [10^{11}]	.26	.26	.81	.81
Electron average current, [A]	.12	.83	.37	2.56
Electron IP beta, β_e^* [m]	0.089	0.089	0.139	0.139
Electron angular beam size, $\sigma_e'^*$ μr	450	450	360	360
Electron bunch length, [mm]	9	9	9	9
Electron beam-beam parameter, ξ_e	0.6	0.6	0.6	0.6
Electron average power, [GW]	1.2	8.3	3.7	25.6
Synchrotron radiation power, [MW]	0.43	3.04	1.3	9.3
Linear synchrotron power, [kW/m]	.28	1.99	.87	6.1

Intra-Beam Scattering (IBS) and Electron Cooling: Intra-Beam Scattering diffusion can be very strong for heavy ions such as gold. The normalized root-mean-square emittance is expected to grow from about 2 mm mrad to about 7 mm mrad in a nominal uncooled 10 hour RHIC store. As a rule, the effect is stronger at lower energies. Electron coolers can fight IBS, even reducing the emittance below its injection value. For example, the RHIC gold emittance is predicted to shrink to about 1 mm mrad after 1 hour in a proposed e-cooling upgrade scheme [8,9].

Laslett Space Charge Tune Shift: The space charge tune shift of the ion beam is given by

$$\Delta Q_{SC} \approx -\frac{N_i}{\varepsilon_i}\frac{C}{\sigma_L \beta\gamma^2}\left(\frac{r_i}{2(2\pi)^{3/2}}\right).$$

Although its dependence on N/ε is reminiscent of the beam-beam parameter, in contrast it is strongly dependent on ring circumference *C*, root-mean-square bunch length σ_L, and the Lorentz factors β and γ. Because the space charge interaction is "smoothly" spread over the circumference of the ring, resonances tend to be weakly driven, and so values as large as $\Delta Q_{SC} \approx 0.1$ can be reasonably supported. At constant bunch length, space charge is much more of a problem at injection when $\beta\gamma^2$ is smallest. However, it is possible to make the bunch much longer at injection. For example, RHIC injects and accelerates with a 28 MHz rf system, but stores beam for collisions with a 197 MHz rf system. In collision, the bunch length cannot be increased beyond about $\sigma_L \approx \beta^*$ without the loss of luminosity to the "hourglass" effect.

4.2.2.1.2 Electron Storage Ring Issues

Synchrotron Radiation: The total synchrotron radiation power in a ring with dipoles of bending radius ρ is

$$P[MW] = 0.0885\frac{E^4[GeV^4]I[A]}{\rho[m]}.$$

A related constraint is the need to keep the linear heat load per meter of dipole, given by $P_{\lim} = \frac{P}{2\pi\rho}$, to less than about 15 kW/m [10]. Table 4.2 shows that, even with 2520 bunch in electron-gold collisions, the linear power in the arcs only reaches 6.1 kW/m. However, in the constrained geometry of the existing RHIC tunnel it may be necessary to include some dipoles with a tighter bending radius, and an increased linear heat load.

Polarization: The natural Sokolov-Ternov polarization time, $T_{pol}[s] = 15.8\frac{C\rho^2[m^3]}{E_e^5[GeV^5]}$, is 9.9 hours in a full circumference eRHIC electron ring. All polarization will be lost if the electrons are accelerated (or decelerated) through any one of the intrinsic spin resonances that are spaced in energy by 0.441 GeV. Therefore, the full energy electrons must be pre-polarized when injected into an electron ring in the RHIC tunnel. One way to do this is to use a full energy linac equipped with a polarized source. Another is to use a conventional booster ring. The above equation shows that an eRHIC booster with 1 T diploes (ρ = 33.4 m) and a packing fraction of 0.5 (C = 420 m) has a polarization time of only T_{pol} = 74 s. Such a booster would accelerate electron bunches from say a 1 GeV injection energy to a 10 GeV flat-top, and then hold them there for a couple of minutes before injection into the electron storage ring.

Interaction Region Optics – Spin Rotators: Polarized electron experiments require spin rotators in the interaction region optics, to rotate the spin vector from vertical in the arc to longitudinal at the interaction point. Figure 4.4 show a straw man eRHIC interaction region layout including spin rotators [3].

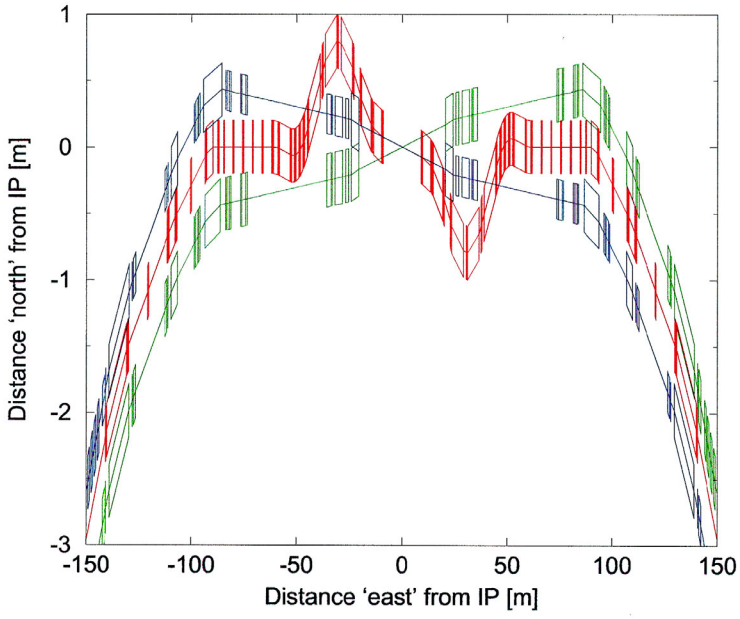

Figure 4.4: Plan View of an eRHIC Interaction Region with Spin Rotators

Not shown in the plan view is a vertical drop of almost 1 m, which puts the electron ring near the floor of the tunnel in the arcs. The spin rotator dipoles may have much higher fields than in the arcs, as high as B = 0.43 T in the straw man eRHIC optics. These few dipoles have much higher linear heat loads than the common arc dipoles.

4.2.2.1.3 Conclusions

The accelerator physics issues associated with adding electron-gold and polarized electron-proton collisions to the RHIC facility have been considered. Constraining the electron ring to lie within the existing RHIC tunnel is attractive but inevitably leads to non-optimal performance in a couple of instances. First, the natural polarization time of the large circumference electron ring is so long that pre-polarized electrons must be injected at the full storage energy of up to 10 GeV, either from a linac or from a polarizing booster. Second, the spin rotators included in the straw man electron ring optics suffer from geometric constraints that lead to increased synchrotron radiation heat loads.

The ultimate luminosity performance was, suggesting polarized electron-proton luminosities as high as 2.4 x 10^{33} $cm^{-2}s^{-1}$ and electron-gold luminosities as high as $6.1x10^{31}cm^{-2}s^{-1}$, depending on how many bunches can be stored. Preliminary experience with RHIC suggests that the electron cloud effect could be the most severe limitation to

the number of ion bunches. Engineering and financial factors associated with synchrotron radiation limit the number of electron bunches. Electron cooling of the ion beam is assumed in all cases.

4.3 Electron Linac On Proton Ring Colliders

This section discusses the proposed electron-proton/ion colliders with center-of-mass energies between 14 GeV and 100 GeV (protons) or 63 GeV/A (ions) based on the recirculating linac-on-ring concept. Although the linac-on-ring scenario is not as well developed as the ring-ring scenario, comparable luminosities appear feasible. The linac-on-ring option has the advantage of easy spin reversal. At higher energies, such as for eRHIC, the small linac beam emittance provides for a number of design simplifications.

We present luminosity projections for the linac-ring scenario are based on fundamental limitations. Four conceptual point designs are considered corresponding to electron to proton energies of 3 GeV on 15 GeV, 5 GeV on 50 GeV and 10 GeV on 250 GeV, and for gold ions with 100 GeV/A. The last two designs assume that the protons or ions are stored in the existing RHIC accelerator. The advantages of electron linacs over electron rings as well as some remaining accelerator physics issues with energy recovering linacs are discussed, and a list of required R&D for the realization of such a design is presented.

Energy recovery is a crucial requirement to achieve manageable power costs for a collider linac with a beam power of a Giga-Watt or more. Energy recovery is the process by which the energy invested in accelerating a beam is returned to the RF cavities by decelerating the beam. To date, energy recovery has been realized in a number of different ways [11,12,13,14]. Reference 12 describes same-cell energy recovery in the Thomas Jefferson Laboratory IR FEL with continuous wave currents up to 5 mA (limited by the gun power supply) and energy up to 50 MeV.

The benefits of energy recovery are:

- The required rf power becomes nearly independent of beam current.
- The electron beam power disposed of at the beam dumps is reduced by the ratio of the final to injected energy.
- The induced radioactivity (and therefore the shielding) is reduced if the beam is dumped below the neutron production threshold.

4.3.1 Luminosity

The luminosity of an electron linac-on-proton ring collider, assuming both beams are round Gaussians at the interaction point (IP), is given by the same expression as for a ring-ring collider, (Section 4.2)

$$L = N_e N_p f_c /(4\pi\sigma^{*2}) .$$

4.3.1.1 Luminosity at the Laslett and Beam - Beam Tune Shift Limits

The Laslett tune shift, $\Delta\nu_L$, of the proton beam imposes a fundamental limit on the ratio of N_p/σ_p^{*2}, while the beam-beam tune shift, ξ_p, of the proton beam imposes a fundamental limit on N_e/σ_e^{*2}. One can write an expression for the luminosity in the limit of Laslett and beam-beam tune shifts:

$$L = \left(\frac{4\pi\sqrt{2\pi}}{r_p^2} \right) \xi_p \Delta\nu_L \frac{\gamma_p^4}{C} \frac{\sigma^{*2}}{\beta^*} f_c$$

As an example, we can assume a beta function at the IP of β^*=10 cm, a root-mean-square beam size at the IP of σ^* = 40 μm and collision frequency of f_c = 150 MHz. Figure 4.5 is a plot of luminosity vs. proton beam energy, E_p.

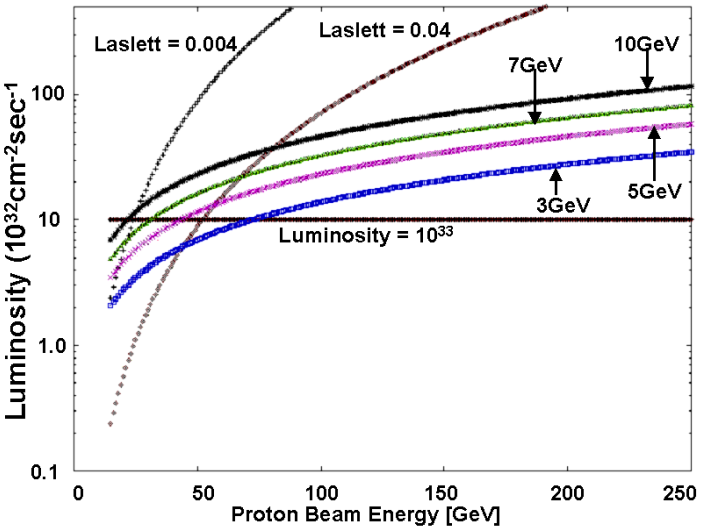

Figure 4.5: Luminosity vs. Proton Beam Energy

This figure shows the luminosity at Laslett and Beam-Beam tune shift limit of 0.004 and 0.04, and at the stability limit of the beam induced head-tail effect for beam energies of 3, 5, 7, *and* 10 GeV *(linear approximation). The straight line marks a luminosity of* 10^{33} $cm^{-2}s^{-1}$.

The highest curves are given by the equation for the luminosity in the limit of Laslett and beam-beam tune shifts. The ring circumference, *C*, was minimized subject to the engineering constraint of maximum magnetic field (in this case B = 4 Tesla). The two curves correspond to: (a) $\Delta\nu_L$ = 0.004, which is a safe and generally accepted value for the Laslett tune shift, and (b) $\Delta\nu_L$ =0.04, which is a more aggressive value, yet consistent with the value assumed in the ring-ring scenario in Section 4.2. In both cases ξ_p =0.004, is consistent with the value assumed in the ring-ring scenario. Of course, in practice N_p and N_e are further limited by a number of other effects such as collective instabilities. The horizontal line in Figure 4.5 corresponds to luminosity equal to 1.0 x 10^{33} cm^{-2} sec^{-1}.

4.3.1.2 Luminosity at the Beam - Beam Induced Head - Tail Instability Limit

The beam-beam induced head-tail instability is an additional effect, which could potentially impose a limit on the luminosity of linac-ring colliders. Presently this instability is the subject of focused investigation at Thomas Jefferson Laboratory. Using a linearized model, the stability condition can be expressed as

$$\frac{N_p r_e \sigma_z^p}{\gamma_e \sigma_p^{*2}} \xi_p \le 4\nu_s$$

where ν_s is the synchrotron tune of the proton beam. One can re-write the luminosity in the limit of the head-tail instability, as

$$L = \left(\frac{4}{r_e r_p} \right) \gamma_e \gamma_p \nu_s \sigma'^{*2} f_c .$$

The remaining curves in Figure 4.5 display the luminosity in the limit of the head-tail instability as function of proton energy for four values of the electron beam energy: 3, 5, 7, 10 GeV. The synchrotron tune has been set equal to 1×10^{-3}, the root mean square angular divergence of the beam at the IP, $\sigma'^{*} = \sigma^{*} / \beta^{*}$ = 40μm/10cm = 0.4 mrad, and the collision frequency f_c=150 MHz. Figure 4.5 demonstrates that above a certain proton beam energy, increasing the Laslett tune shift beyond the generally accepted values does not benefit the luminosity. Assuming that the larger value of the Laslett tune shift is attainable, then the luminosity is limited by the head-tail instability over most of the energy range of protons and electrons. A more careful non-linear analysis of this effect will be required to determine if the instability threshold can be raised significantly.

4.3.2 Conceptual Point Design Parameters

We now turn our attention to specific point designs that span a proton energy range from 15 to 250 GeV and an electron energy range from 3 to 10 GeV. The condition for head-tail instability was derived using a linear approximation. This does not reflect the true complexity of the problem. In the absence of more rigorous results, we will present reasoning for the point designs without taking the head-tail instability into account and will defer the more complete study to a later document.

Four sets of input parameters are considered:

- Proton beam energy of 15 GeV colliding with electron beam energy of 3 GeV,
- Proton beam energy of 50 GeV and electron beam energy of 5 GeV,
- Proton beam energy of 250 GeV and electron beam energy of 10 GeV and,
- Gold ion beam of 100 GeV/A and electron beam energy of 10 GeV.

The two high-energy designs are based on the existing RHIC storage ring.

The technology of the electron linac is well established. Thomas Jefferson Laboratory has significant expertise in superconducting rf linacs, and the superconducting rf accelerating structures are commercially available from a number of manufacturers.

We assume that the linac structures will be identical to the well-known TESLA style cavities. These cavities and the ancillary equipment (cryostats, couplers, tuners, HOM loads etc.) have been optimized for cost and performance. Using demonstrated performance from a number of manufacturers, we assume, conservatively, a Q_0 of 1.5×10^{10} at 2K and an accelerating gradient of 20MV/m. At these values, the refrigeration power is 26 W/structure. Thus a 10 GeV linac, for example, will require 500 cavities with a dissipation (excluding standing losses) of 13 kW. TESLA optimization was driven towards high gradient, not low Q. We can expect further improvement in Q [15].

4.3.2.1 3 GeV Electrons on 15 GeV Protons: $\Delta\nu_L \leq 0.004$

In this case, we assume that both the Laslett and beam-beam tune shifts cannot exceed 0.004. To arrive at a self-consistent set of parameters and a luminosity estimate, we first set the electron beam size at the IP based on projected electron source performance. Then the proton beam parameters are set at the Laslett tune shift limit. The maximum number of electrons per bunch is determined at the beam-beam tune shift limit of the protons. Finally, effects that influence the choice of the bunch collision frequency are discussed.

We assume a root-mean-square normalized emittance of 60 mm mrad for electrons at a bunch charge of approximately 1 nC, yielding a geometric emittance of 10 nm at the IP (3 GeV). For a beta function of 12 cm (discussed later), the root-mean-square electron beam size at the IP is 35 μm. Round beams are assumed for electrons and protons.

In order to prevent degradation of the luminosity by the hourglass effect, the beta function for the proton beam at the IP is typically set approximately equal to the root-mean-square proton bunch length. In this case, the Laslett tune shift can be written as

$$\Delta\nu_L = \frac{N_p}{\sigma_p^{*2}} \frac{r_p}{4\pi\gamma_p^3} \frac{C}{\sqrt{2\pi}}.$$

Clearly, the tune shift sets a limit on the ratio of N_p/σ_p^{*2}. Assuming a proton beam root-mean-square normalized emittance of 3 mm mrad (consistent with LHC and RHIC experience) and $\Delta\nu_L$ = 0.004, the root-mean-square beam size for protons at the IP is 107 μrad for a beta function of 6 cm. Then the number of protons per bunch at the Laslett tune shift limit is 3×10^{10} for a ring circumference, C, of 128m.

The number of electrons per bunch can be limited either by the beam-beam tune shift of the proton beam or by single-bunch transverse beam breakup in the linac [16]. We assume that the beam-beam tune shift of the protons cannot exceed 0.004, which sets the

number of electrons per bunch equal to 1.1×10^{10}. One can obtain a simple estimate for the emittance growth due to single-bunch beam breakup in the linac by using the following expression [16],

$$\eta = \frac{L r_e N_e W_0}{k_0(\gamma_f - \gamma_0)} \ln \frac{\gamma_f}{\gamma_0}$$

where η is the emittance amplification, L is the length of the linac, k_0 is the betatron wave number, W_0 is the transverse wake function, r_e is the classical radius of the electron and γ_0 and γ_f the initial and final linac energies.

For a root-mean-square bunch length of 1 mm and betatron wavelength in the linac of 50 m, the amplification parameter η remains less than ~1 if the number of electron per bunch does not exceed 1.5×10^{11}. BNS damping can be used if this effect becomes a serious limit. Therefore, in this case the limit on N_e is set by the beam-beam tune shift, and not the single-bunch beam breakup.

The bunch collision frequency should be maximized subject to the constraints of parasitic collisions, user requirements, and possibly the electron cloud effect in the proton ring. We have assumed a bunch separation of 6.66 nsec or 150 MHz repetition rate. Note that the luminosity scales linearly with the frequency.

For the case of unequal electron-proton bunch sizes, the luminosity is given by the standard luminosity equation with $2\sigma^{*2}$ replaced by $(\sigma_e^{*2} + \sigma_p^{*2})$. For $N_e = 1.1 \times 10^{10}$, $N_p = 3.0 \times 10^{10}$, f_c =150 MHz, σ^*_e =35 μm and σ^*_p = 107 μm, the luminosity is equal to 6.2×10^{31} cm^{-2} sec^{-1}.

4.3.2.2 3 GeV Electrons on 15 GeV Protons: $\Delta\nu_L \leq 0.05$

We now consider a point design that assumes that the Laslett tune shift is as high as 0.05. In this case, the electron beam parameters remain the same and again the Laslett tune shift sets the ratio of N_p/σ_p^{*2}. However the optimization proceeds by first determining the limit on N_p and then setting the minimum spot size at the IP at the Laslett tune shift limit.

The number of protons per bunch can be limited by collective instabilities or by the emittance growth of the electron beam due to a single round-beam collision with the protons. We set $N_p = 1 \times 10^{11}$, as in the case with LHC and RHIC. (These limiting effects are discussed later). At the Laslett tune shift limit, the root-mean-square beam size of the protons is 58 μrad and for $\beta^* = 10$ cm and the normalized root-mean-square emittance is 0.54 mm mrad. Note that at $N_e = 1.1 \times 10^{10}$, the beam-beam tune shift is 0.0068. These parameters yield luminosity equal to 5.7×10^{32} cm^{-2} s^{-1}.

4.3.2.3 5 GeV Electrons on 50 GeV Protons

Following similar arguments for the case of 5 GeV electrons on 50 GeV protons, we arrive at the two sets of parameters outlined in Table 4.3. Note that luminosity of 10^{33} is attainable at these energies, for average current in the linac of 0.264 A and an average current in the ring of 2.4 A.

Table 4.3: Parameters for Point Designs 1 and 2.

Parameter	Units	Point Design 1A	Point Design 1B	Point Design 2A	Point Design 2B
E_e	GeV	3	3	5	5
E_p	GeV	15	15	50	50
N_e	ppb	1.1×10^{10}	1.1×10^{10}	1.1×10^{10}	1.1×10^{10}
N_p	ppb	3.0×10^{10}	1.0×10^{11}	1.0×10^{11}	1.0×10^{11}
f_c	MHz	150	150	150	150
σ^*_e	μm	35	35	25	25
σ^*_p	μm	107	58	60	25
ε^*_e	nm	10	10	6	6
ε^*_p	nm	200	33.6	36	6.25
β^*_e	cm	12	12	10	10
β^*_p	cm	6	10	10	10
σ^p_z	cm	6	10	10	10
σ^e_z	mm	1	1	1	1
ξ_p	–	.004	.0068	.004	.004
$\Delta\nu_L$	–	.004	.05	.004	.024
I_e	A	.264	.264	.264	.264
I_p	A	.720	2.4	2.4	2.4
L	$cm^{-2}\ sec^{-1}$	3.5×10^{31}	3.9×10^{32}	3.6×10^{32}	2.1×10^{33}

4.3.2.4 10 GeV Electrons on 250 GeV Protons: Parameters Based on the RHIC Storage Ring

The third and fourth point designs presented here are for 10 GeV electrons colliding with 250 GeV protons or 100 GeV/A ions using the existing RHIC storage ring [3]. The lower energy point designs may also be implemented in RHIC.

Since the design of the IP, in particular the size of the detector, depends on the energy, it is reasonable to assume that at least two detectors will be required. The RHIC machine has two independent ion rings and thus could support one (or more) IP per ring, with collisions taking place at two different energies. The electron linac also could be designed to simultaneously provide two energies, but the detailed description of this mode will not be addressed in this report.

The parameters presented are consistent with the RHIC layout. A schematic layout of the linac-ring collider is shown in Figure 4.6 and Table 4.4 summarizes the linac parameters, common to both protons and gold. As seen in Figure 4.6, all the acceleration is done virtually in a straight line to avoid emittance growth and synchrotron radiation loss in the accelerated beam. The recuperating beam is bent to return to the appropriate sections.

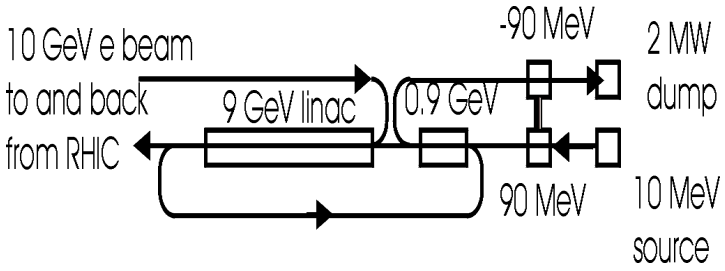

Figure 4.6: Schematic Layout of the RHIC - Based Linac-Ring Collision Scenario.

Table 4.4: Electron Linac Parameters Common for Gold and Protons.

Parameter	Units	Value
Electron energy	GeV	10
Electron average current	Amperes	0.27
Collision frequency	MHz	56
Electron bunch population N_e		$3x10^{10}$
Electron rms emittance, ε_e	μrad	0.003

The electron source has an injector linac that accelerates the beam to 10 MeV. The power invested (at 0.27 amperes) for this purpose is 2.7 MW. This section has no recuperation. Next is a low gradient 90 MeV energy gain pre-accelerator. Here energy recuperation may be done in a dedicated linac section, and the recovered energy would then be fed through waveguides to the accelerating section, shown schematically in Figure 4.6 as a connection between the accelerating and decelerating linacs. The 100 MeV beam from the pre-accelerator is fed into a 0.9 GeV (energy gain) intermediate linac with energy recovery accomplished in the same section. Last is the main linac with an energy gain of 9 GeV. The 10 GeV beam is taken to the collision area where the beam may be introduced into a ring-like transport for multiple IPs, a single IP or anything in-between.

The beam is returned at 10 GeV to the entrance of the main linac for deceleration and energy recovery. The beam is decelerated to 1 GeV, and then sent to the intermediate energy linac for deceleration to 100 MeV. By recovering the energy of the beam in the same linac structure, we conform to the conservative limit of the Douglas principle [17] of keeping the energy ratio of the two beams under 10. Deceleration to 10 MeV follows in a dedicated 90 MeV pre-dump linac. The 10 MeV beam is sent to the beam dump, rated at 2.0 MW assuming a synchrotron radiation loss of 0.7 MW. A power level of 2 MW was demonstrated in SLAC beam dumps. It is possible to decelerate the beam to a lower energy should the beam dump rating be below 2 MW, but this RF power will not

be used for acceleration. Note that any synchrotron radiation power loss anywhere in the high-energy transport will subtract from the power deposited in the beam dump.

Table 4.5 summarizes the electron-gold and electron-proton collision parameters. We take the 720-bunch case, which corresponds to a bunch collision frequency of 56 MHz, and assume minimal electron cooling of the ion beam. That results in a smaller ion beam emittance and allows for larger tune shifts in the electron beam. Other than this, the RHIC parameters are mostly the same as for the ring-ring case. In the case of gold, the limit is set by the beam-beam tune shift for the ions. We do not take advantage of the large possible increase in the beam-beam tune shift due to the cooling. That may account for a further increase in the luminosity.

Table 4.5: Electron-Ion Collision Parameters Assuming Electron Cooling of RHIC

Parameter	**Units**	**Gold**	**Proton**
Ion bunch population		1.9×10^{9}	0.93×10^{11}
Number of bunches		720	720
Ion rms normalized emittance	mm mrad	0.78	0.67
RMS beam size at the IP, σ^*	mm	0.05	0.03
Electron IP beta function	m	0.72	0.36
Electron beam-beam tune shift ξ_e		0.287	0.5
Ion beam-beam tune shift ξ_I		0.0046	0.0046
Ion Laslett tune shift, ξ_L		0.008	0.0046
Luminosity, L	$[cm^{-2}s^{-1}]$	1.0×10^{31}	1.4×10^{33}

The high-energy IP of RHIC is extremely generous in size, with free space (no accelerator component) for the detectors extending ±10 m from the IP center. A low energy IP, using the second storage ring, can be designed with accelerator components extending much closer to the IP center, thus boosting the luminosity at low energies.

The calculation for an electron energy of 10 GeV, shows that the performance would be unaffected by a much lower (or higher) electron energy. Thermal loading in magnet chambers is not a limitation for the relatively low electron beam current. In addition, larger radii of curvature in the IP optics are possible because the spin rotation optics are removed from that area, further reducing the thermal loads relative to a ring-ring case.

We conclude that good luminosities can be obtained using a linac-ring collider with modest electron cooling of the ions in the ring. Further increases in the luminosity are possible. In the gold case, the increase would come from pushing the Laslett tune shift to higher values, taking advantage of the cooling. In the proton case the luminosity can be improved by going to a higher current in the electron linac by pushing on the beam-beam tune shift in the ring, once again taking advantage of the cooling.

4.3.2.5 Electron Linacs: Advantages and Challenges

An electron linac has intrinsic advantage over an electron ring because the electron spin can be flipped more easily and rapidly without loss of polarization. A serious challenge, however, is the development of a polarized electron injector delivering average beam currents three orders of magnitude larger than those available today; this is addressed in Section 4.3.2.6. A second problem is electron beam delivery to more than one interaction point. This requires substantial additional high-current beam transport lines.

For high-energy schemes such as eRHIC, there are a number of additional advantages of an electron linac over an electron ring:

- A linac, in principle, avoids the limitation of the electron beam-beam tune shift inherent in a ring-ring scenario. This allows reduction of the beam size of the ion storage ring and increases the charge per bunch considerably. However, further study of the beam-beam head-tail instability is necessary to determine how large an advantage truly exists in the linac-ring collider scenarios.
- A linac has a very low emittance. This leads to a small collision point beam size with a relatively large beta function, increasing luminosity and simplifying the optics of the interaction point.
- The fact that the electrons are used only once means that complicated spin rotation conditions are relaxed and the IP optics of the linac can be simplified.

On the other hand, there are a number of unresolved accelerator physics issues associated with energy recovering linacs that need further examination, for example:

- Accelerator transport at high current: phase-space matching into the IP, dynamic energy range of linac for 2-beam confinement, control of beam loss.
- Coherent synchrotron radiation in re-circulation arcs that can cause emittance growth.
- Higher-Order-Mode power dissipation in superconducting rf cavities that may require cooled absorbers.
- Beam breakup: single-and multi-bunch phenomena can cause emittance growth and energy spread, excite transverse instabilities, and limit bunch charge and average beam currents; this may require feedback control.

4.3.2.6 Technological Issues: High Current Source of Polarized Electrons and Electron Cooling of Proton Beams

The generation of high average current, high polarization electron beams is a significant technological issue for a linac-based collider. Sinclair [18] reviewed the state-of-the art in polarized electron sources in the PAC99 article. The prospects for sources of high average current polarized electrons were presented in the Proceedings of the 2nd eRHIC Workshop [19]. Presently, polarized sources at Thomas Jefferson Laboratory have cathode operational lifetimes one order of magnitude greater than those reported by

Sinclair at PAC99 [3]. The cathode operational lifetime in these sources is limited only by ion back-bombardment, and now exceeds 100,000 Coulombs/cm^2. While construction of a high average current polarized source with modest polarization (~ 37%) is probably within reach, a source with a high polarization (~ 75%) faces a number of serious technological challenges. Significant R&D would be required before one could plan on a source delivering a high average current at high polarization.

Electron cooling of proton beams is an essential issue common to both collider scenarios. It is mentioned here only for completeness, and is thoroughly addressed in Section 4.4 of this report.

4.3.2.7 Conclusions

Preliminary results of a feasibility study of an energy recovering electron linac on a proton ring collider are presented. Luminosities at the 10^{33} level appear attainable. The linac-on-ring scenario has the advantage of easy electron spin control. At eRHIC energies, the lower electron beam emittance allows significant design simplifications.

R&D topics that need to be pursued before such a facility is designed and built have been identified and include:

- High current polarized electron source,
- High current (~200 mA) demonstration of energy recovery ,
- Theoretical and, if possible, experimental investigation of the beam-beam induced head-tail instability and feedback,
- Electron cooling and its ramifications on Laslett and beam-beam tune shifts, and
- Development of multi-pass beam-breakup feedback.

Recently, re-circulating, energy-recovering linacs have attracted much attention and are being considered for a number of applications, such as drivers for synchrotron radiation sources and high average power Free Electron Lasers. A number of the listed R&D topics, especially those related to the energy recovery of high average currents, are being pursued by these communities, so it is safe to assume that progress will be rapid in these directions.

4.4 The Electron Ion Collider Electron Cooling System

To attain the design luminosity the 50-100 GeV/nucleon ion beam in the EIC, the ion ring needs to be continuously cooled while colliding with electrons. To date, there is no fully developed cooling technology for such an energy range for bunched ion beams. A possible schematic design of a suitable electron cooling system for the EIC ion ring is outlined here, along with unresolved R&D issues that need to be addressed.

According to the well-proven concept of electron cooling [20], the electron beam needed to cool the ions must co-propagate with the ion beam in a straight section of the ring free of focusing magnets. The velocities of two co-propagating beams must precisely coincide. This requires an electron beam energy of up to 50 MeV for the EIC. The portion of the ring dedicated to the electron cooling system has to be as long as possible (cooling rate is proportional to this length), but typically comprise no more than a few percent of the ring's circumference. The use of low-energy electrons (<1 MeV) for cooling is a well-developed technology, but the required electron energy of 50 MeV coupled with a relatively high average beam current (about 100 mA or greater) poses a significant technological hurdle.

All electron cooling systems in operation today are *low energy* systems. These systems are characterized by the use of a conventional Cockcroft-Walton (C-W) high-voltage supply to bias the electron source with respect to the cooling region, and by a continuous longitudinal (solenoidal) magnetic field to confine (focus) the electron beam. Modern commercial C-W voltage generators are limited to about 0.6 - 1 MV, about a factor of 2 - 3 times higher than the electron systems in operation today. This is the principal technical limitation in the low energy regime.

For electron kinetic energies up to about 5-8 MeV (ion energies 10-15 GeV/nucleon), it is technically feasible to use a conventional dc electrostatic accelerator in a recirculation mode. INP Novosibirsk developed the technology for a 1 MeV, 1 A dc recirculation system operating in a continuous solenoidal magnetic field of 500 G [21]. The high-voltage power supply was based on an industrial high-power electron accelerator, developed at INP. This system requires many improvements to extend the range to a 5 - 8 MV. Because of the highly nonlinear behavior of high-voltage technology, such a large extrapolation is problematic, and this system is not currently in development. Fermilab is currently developing a 5 MeV dc electron cooling system to cool 8.9 GeV/c antiprotons [22]. To date, this is the only funded R&D project that would qualify (if successful) as a high-energy system.

For higher electron energies, up to hundreds of MeV, the most promising approach would appear to be rf acceleration of bunched electron beams in an energy-recovering linac system.

4.4.1 The Proposed Electron Ion Collider Electron Cooling System

A free-electron laser group at the Thomas Jefferson Laboratory [23] recently demonstrated successful operation of this type of accelerator at an energy of about 50 MeV and a current of up to 5mA. The proposed EIC electron cooling system discussed below is similar, but at much higher current.

Figure 4.7 shows schematically the proposed EIC electron cooling system. It consists of a cooling section solenoid, bunching and debunching optical inserts and cavities, an electron linac structure, an electron gun and a beam dump. Solenoidal transport of the

electron beam through an extended cooling section is needed to suppress space-charge divergence of the electron bunch and prevent electron-ion transverse instabilities.

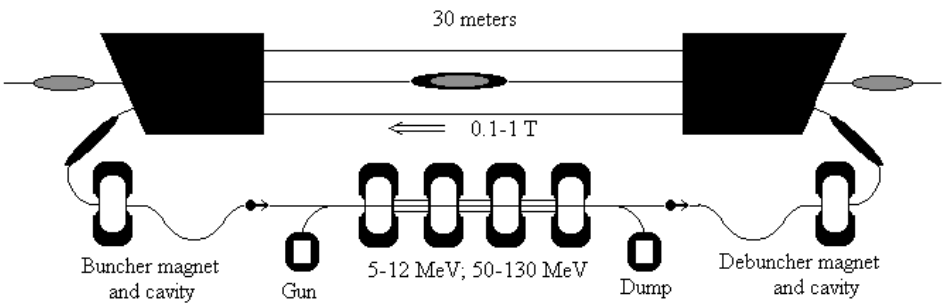

Figure 4.7: The Schematic Diagram of the Proposed EIC Electron Cooling System

The electron gun must be properly immersed in a solenoidal magnetic field in order to match the beam size and divergence to the magnetic field strength in the cooling section [24]. The debunching optical insert must match the electron bunch length to the ion bunch length, and the rf cavity must reduce the electron relative momentum spread to a value of about 10^{-4} for effective cooling. After deceleration and beam energy recovery, the electron beam of about 1 MeV is dumped in the absorber. The cooling section length of 30 m was chosen to be about 1-2% of the ion ring circumference.

The transverse emittance damping time, $\tau = \varepsilon_i / (\mathrm{d}\varepsilon_i / \mathrm{d}t)$, can be expressed as following

$$\tau = \frac{A}{Z^2} \frac{\gamma^2}{4\pi\eta\Lambda} \frac{1}{r_e r_p c n_e} \left(\beta\gamma \frac{\varepsilon_i}{\beta_i} \right)^{3/2} .$$

In this expression:

A and Z are the ion atomic and charge numbers, respectively,
β and γ are the usual relativistic parameters and β_i is the cooling section beta-function,
η is the length of the cooling region divided by the ring circumference,
Λ is the Coulomb logarithm (≈2-10 depending on the magnetic field strength),
r_e and r_p are the classical electron and proton radii,
c is the speed of light,
n_e is the laboratory frame electron beam density; and
ε_i is the normalized ion beam emittance.

This expression is very approximate; it does not take into account electron transverse temperature or ion beam energy spread, but it can give an order-of-magnitude estimate for the cooling time. For protons, one obtains $\tau \approx 30 - 150$ minutes under the following assumptions: $\gamma = 50$, $n_e = 1\times10^9$ cm^{-3}, $\eta = 0.02$, $\varepsilon_i = 2$ mm × mrad, $\beta_I = 60$ m. More accurate estimates of the cooling time need to include specific values of the magnetic field strength, the shape of the electron density distribution function, betatron and synchrotron ion motion, etc. This is beyond the scope of this conceptual outline.

4.4.2 Unresolved Technical Issues

To achieve an operating 100mA, 50MeV electron cooling system a number of R&D topics need to be addressed. These range from theoretical exploration of some fundamental questions and improved definition of system parameters (e.g., through simulation studies) to practical demonstrations of technical requirements. They include:

- Production, acceleration, and transport of high-quality rf-bunched electron beams in a magnetic field: What will be the highest average-current that can be stably accelerated and energy-recovered in a superconducting linac?
- Is the magnetic field in the cooling section beneficial? If yes, what is the required field strength?
- What portion of the rf accelerator needs to be immersed in a solenoidal magnetic field?
- How can solenoids and the acceleration cavities be combined?
- Magnetic field quality in the cooling section: What is the required field quality? In practical terms, how does one attain and measure this field quality in a 30 m long solenoid?
- What are the required electron and ion beam diagnostics in the cooling section, and how can they be made compatible with the solenoid design?
- Cooling times and evolution of the ion beam distribution function: What are the cooling times as a function of ion beam emittance? What is the optimal value of the beta-function in the cooling section? What is the optimal electron beam size? What is the optimal electron bunch length?
- How will feedback systems improve the multi-bunch multi-pass instability threshold current?

Experts in this field believe that the proposed high-energy electron cooling system is an achievable goal on a time scale consistent with that for the overall collider project if resources to carry out the required R&D effort are made available sufficiently early.

4.5 Interaction Region

The obvious questions about any final-focus IP regions on which machine designers, experimenters, and detector designers must all work together closely are:

- How close to the IP can the accelerator-lattice magnet structure intrude?
- How much of a reduction in useful detector solid-angle acceptance in forward and backward directions can be tolerated?

A mutually acceptable compromise must be found between the competing requirements for quick electron-proton (e - p) bunch transverse separation close to the IP to avoid

multiple parasitic collisions per bunch crossing, and minimum forward (backward) detector acceptance restrictions.

The concept for the IP regions in both e - p collider scenarios is still very preliminary. Strong bending magnets are required to separate the beams immediately after the intersection to minimize secondary collisions. Powerful quadrupoles with large apertures are needed to strongly focus the beams onto the IP with $* . 10cm. Such strong magnets close to the IP tend to have large transverse dimensions, interfering with detection of reaction products at small angels with respect to the beam direction at the IP.

Figure 4.8 shows one example of an e - p collider interaction region design for $* = 6 cm and only one parasitic (secondary) collision per bunch crossing.

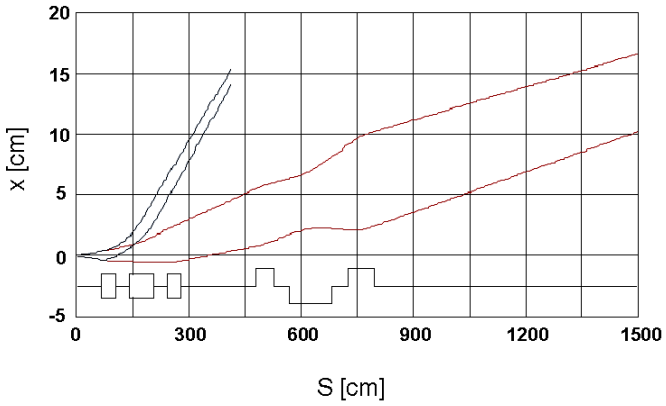

Figure 4.8: Example of the Interaction Region Design for β*= 6 cm.

The IP is located at s = 0. The upper pair of nearly parallel curves indicates the 5F envelopes of the electron beam (and the lower pair the 5F envelopes of the proton beam). Complete separation occurs at ~0.5m from the IP. The magnet triplet (boxes) closest to the IP is a combined dipole/quadrupole beam separator/lens system starting 0.6 m from the IP. The large-aperture final-focus lens system is located at 5 m < s <8 m.

To minimize the resulting restriction of the detector acceptance, new ideas may be needed, such as an open magnetic system made from thin, superconducting rods (suggested by I. Koop of BINP). It is very likely that the beam-optical components closest to the IP will have to be designed as an integral part of the detector system. Discussions of such detector-machine integration must be initiated soon in order for both detector and machine designs to proceed further and in timely fashion.

The interaction region design affects not only the detector capabilities but also the collider luminosity through $*. The minimum *useful* $* is determined by the root-mean-square bunch length F_z: $*$F_z$. The minimum *achievable* $* is limited by the maximum acceptable aperture of the final-focus quadrupoles (decreasing $* increases $$_{max}$ in the quadrupoles) and/or by the maximum tolerable interaction region chromaticity, <t %1/$* (total machine chromaticity can be compensated in the arcs, but chromaticity due to small $* cannot). For a given, maximum allowable machine tune shift,)<, the permissible momentum spread)p/p =)</<t may require beam longitudinal cooling or limitation of the minimum $*-value.

4.6 References

1. Koop, I.A. et al., "Bates Internal Report" B/EPIC #00-01
2. Schwandt, P., Private Communications
3. Ben-Zvi, I. et al., "RHIC Accelerator Physics Note" C-A/AP/14 April 2000, to be published in *NIMA.*
4. Peggs, S. et al., "Proceedings of PAC 2001", to be published
5. Zimmerman, F., "LHC Project Report" 95 (1997)
6. Gr`bner, O., *PAC* 1997
7. Brhning, O., "LHC Project Repor*t"* 102 (1997)
8. MacKay, W. et al., *PAC* 2001
9. Ben-Zvi, I. et al., *PAC* 2001
10. Seeman, J., PAC 1999 p.1, and *SLAC* 372, 1991
11. Smith, T. I. et al., *NIM* A 259, 1 (1987)
12. Feldman, D.W. et al., *NIM* A259, 26 (1987)
13. Sereno, N.R., University of Illinois, Ph.D. Thesis (1994)
14. Neil, G. R. et al., *Phy. Rev. Lett.* 84, 4 (2000)
15. Kneisel, P., "Proceedings of RF Superconductivity Workshop", Santa Fe, November 1999
16. Chao, A.W., Richter, B. and Yao, C.Y., *NIM* 178, 1 (1980)
17. Douglas, D., Jefferson Lab Technical Note, TN-98-040, 1998
18. Sinclair, C.K, *"*Proceedings of the 1999 Particle Accelerator Conference", New York
19. Hartmann, P. et al., "Proceedings of Yale eRHIC Workshop", BNL 52592 (2000)
20. Budker, G.I. et al., *Part. Accel*. 7, 295 (1976)
21. Veis, M., et al., *EPAC'98*, Rome, 1988
22. Nagaitsev, S., et al., *NIM A* 441, 241 (2000)
23. Neil, G.R. et al., *EPAC,* 764 (2000)
24. Burov, A. et al., *Phys. Rev. SP-AB* 3, 094002 (2000)

5.0 A Prototype Detector for the Electron Ion Collider

In this Section we outline some generic considerations for a suitable detector in the RHIC ring, as an example for the Electron Ion Collider detector.

The experience gained at HERA with the H1 and Zeus detectors provides some guidance for the conceptual design of a detector that will be able to measure complete events in the 4 π coverage produced in collisions of energetic electrons with protons and ions, tunable in energy and spin polarization. The detector design has direct impact on the projected electron accelerator design in the electron-ion interaction region. The selected energy of the electron beam impacts the design of the e - p/A interaction region, and vise versa. The choice of a top energy of 10 GeV allows a geometry that is relatively simple, in comparison to the HERA design at DESY, by decoupling the electron beam insertion optics from the heavy ion beam optics while maintaining the synchrotron radiation power at a tolerable level near the collision point. In addition it allows sufficient space for the detector elements to cover the entire phase space of particle production. While an advantageous geometry can be designed for the ring-ring concept (i.e., ion ring and electron ring option), the very low emittance of the electron beams obtained from a linac provides additional advantages. Electron beams from a linac produce a small collision spot with a relatively large beta function, which greatly simplifies the optics at the interaction point.

The e - p and e - A collisions produce a very asymmetric reaction topology. This is not a disadvantage, since the asymmetry of the electron and proton/ion beam momenta has several intrinsic good qualities. For example, this asymmetry allows a precise measurement of energy and color flow topology in collisions of large and small *x* partons. It also provides an optimal configuration for observing the interaction of electrons with photons that are coherently emitted by the relativistic heavy ions. The detector for the EIC experiment must detect the scattered electrons, the quark fragmentation products and centrally produced hadrons. It must cover the fragmentation region of the proton or nucleus, a domain that was not covered by HERA.

The details of the interaction region geometry impact the parameters of the collision, most crucially the luminosity since the luminosity depends largely on the distance of the last focusing element for the electron beam from the interaction point. This position could vary between 10 cm and 10 m. The design must allow for the high quality, complete reconstruction of e - p and e - A events in the fragmentation region and should have minimal interference with the beam optics of the other interaction regions. The IP geometry also should provide for a precise measurement of the luminosity and of radiative corrections. At this early stage, the detector design should be compatible with the choice of either ring-ring or ring-linac collisions.

5.1 A General Purpose Detector for the EIC

The basic geometry of a detector is depicted in Figure 5.1. It is symmetric around the collision axis (z-symmetric) with a central detector and two intrinsically symmetric arms along the z direction. For the e - p and e - A collisions, the instrumentation on the left, called the hadron side, and the right arm, the electron (lepton) side is different. It would be possible to upgrade such a detector for p - A collisions. This would involve adding the detector elements of the hadron side to the electron side. The following sections discuss each side in sequence.

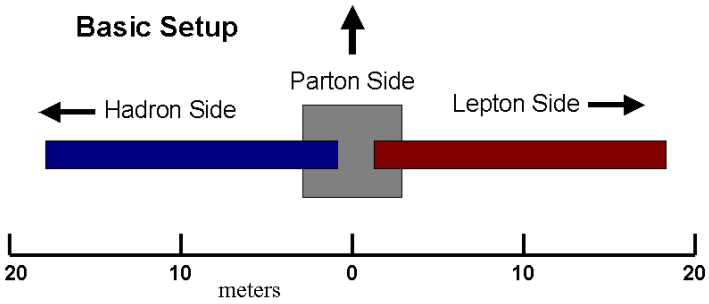

Figure 5.1: Basic Set Up of a General Purpose Detector for the Electron Ion Collider

5.1.1 The Parton Side

The detector measures partons from hard hadronic processes in the region around 90 degrees. These partons are identified as jets in a tracker and with an EM calorimeter backed by an instrumented iron yoke. Electrons from DIS also are emitted into this region and are measured by tracking and EM calorimetry. Electrons from photo-production and from DIS at intermediate momentum transfer are detected on the "lepton side" (section 5.1.3).

A Toy Model is shown in Figure 5.2. The barrel is a Time Projection Chamber (TPC) backed by a gas EM calorimeter inside a superconducting coil.

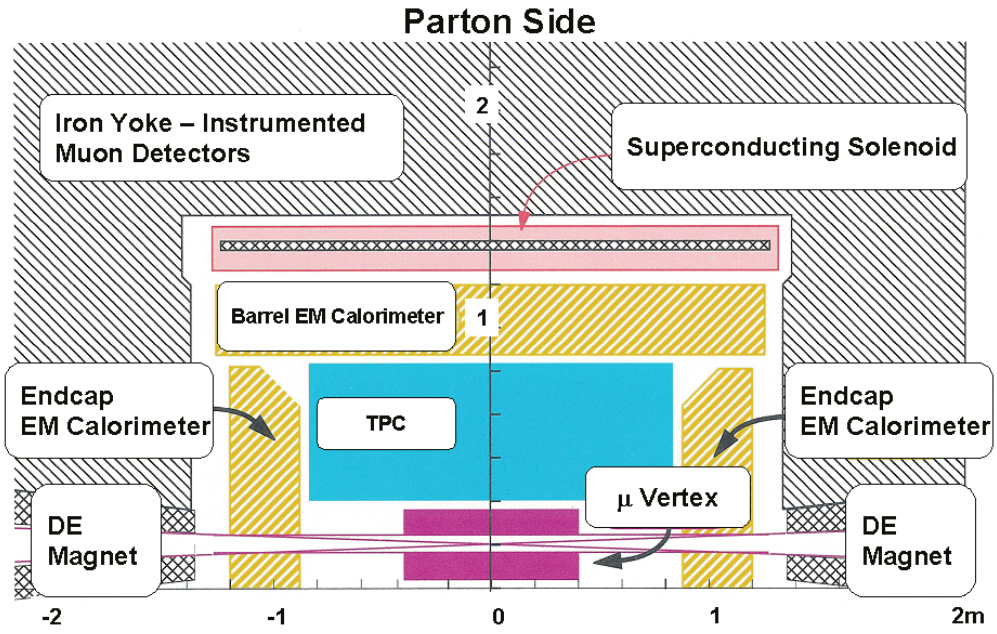

Figure 5.2: The Parton Side of the Generic EIC Detector

Both end caps are spaghetti calorimeters (SPACALs). The micro-vertex detector complements the tracking capacity of the TPC. This is a minimal setup for the central detector. Its size is significantly smaller than any of the RHIC detectors. It is worth noting that the design of the parton-side detector is rather standard. Any existing e^+ - e^- collider such as CLEO and ALEPH could provide the necessary function. If such a detector could be recycled, the costs of the EIC detector would be reduced.

5.1.2 The Hadron Side

The geometry of the hadron side is shown in Figure 5.3. It uses the existing DX magnets incorporated in the RHIC interaction region for a high-rigidity spectrometer. In normal A - A collider operation, the DX magnets bring the two ion beams together. Additional new magnets (DE) are needed to bring the electron beam into collision with the ion (proton) beam. Its magnetic field is used in the design of a medium-rigidity spectrometer. It is important to note that the minimum bending radius of the electron beam that can be tolerated is determined by the energy loss in the electron beam caused by synchrotron radiation.

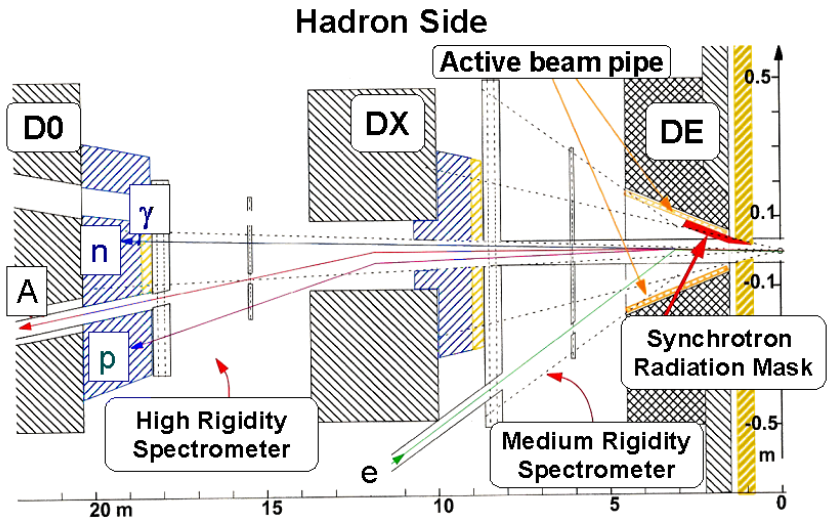

Figure 5.3: The Hadron Side of the EIC Detector.

A Toy Model has the following functional elements (from left to right):

- *Roman Pots* (far up the beam and not shown in the figure) detect coherent diffractive scattering of protons or light ions.
- *The High Rigidity Spectrometer* contains an EM calorimeter, measuring the energy of the photons emitted by excited ions. This is backed by a hadronic calorimeter for measuring the energy of evaporated and "wounded" (i.e., directly struck) neutrons. The hadronic calorimeter also identifies nuclear evaporation fragments. It also contains tracking capabilities for the measuring the momenta of evaporated and "wounded" protons, as well as, for measuring the momenta of evaporated nuclear fragments.

- *The Medium Rigidity Spectrometer* contains an EM calorimeter to measure the energy of neutral pions, a hadron calorimeter to measure the energy of charged pions, "wounded" and evaporated protons. It contains tracking stations for measuring momenta of charged pions and "wounded" and evaporated protons. Both spectrometers would use trackers that consist of multi-wire proportional chambers (MWPC) with drift chambers or silicon microstrip detectors at the center. The calorimeters in both spectrometers use scintillating fibers.
- *A Rapidity Gap Tagger* can be incorporated as an active beam pipe. It closes the acceptance for charged particles emitted in the DIS process and tags diffractive events. The Tagger would consist of a scintillating fiber tracker.

5.1.3 The Lepton Side

The DE magnet provides the symmetric exit for the electron beam. The geometry is shown in Figure 5.4. An electron tagger measures electrons up to 5 GeV in energy and tags on photo-production and DIS events. This limited momentum acceptance is sufficient if the electron beam can be tuned within 4 to 10 GeV.

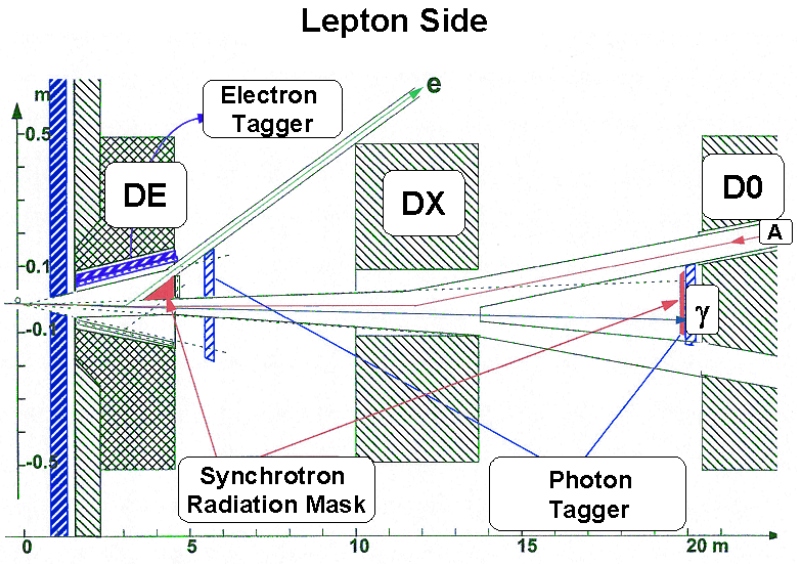

Figure 5.4: The Lepton Side of the Detector

The electron tagger also closes the acceptance for photo-produced charged pions. The gamma tagger measures the Bethe-Heitler photon spectrum to precisely monitor the luminosity and tag initial state Bremsstrahlung for DIS and photoproduction events. It closes the acceptance for the neutral pions. The Toy Model uses scintillating-fiber trackers ("active beam pipe") for the electron tagger and a quartz fiber calorimeter for the photon tagger.

5.1.4 Spectrometer Optics

It is instructive to consider the spectrometer optics of the DE magnets. Our model design is based on a bending power of 2.3 Tm distributed over 3 m, with a field of 0.76 T. This is 3 times higher than the inflection field at DESY. It produces a deflection angle of ~70 mrads for 10 GeV electrons and is designed to rotate the spin vector by 90 degrees. With this geometry the electron beam is separated from the ion or proton beam by about 50 cm at the beginning of the DX magnets. Thus, the electron beam bypasses the DX magnet entirely. This uncouples the electron beam optics from the ion beam optics. This simple beam geometry is possible because the electron beam energy is only 10 GeV. The uncoupling of the electron and the ion (proton) beam optics allows the use of the detector described above both for the electron-ion (proton) and proton-proton (ion) collisions for precision studies of QCD vacuum and hadronic media, if the electron accelerator is constructed at BNL and the electron beam is guided to one of the RHIC intersection points (e.g., the 12 o'clock Interaction Point). The proposed detector set-up provides the opportunity to realize just such a research program.

The synchrotron radiation produced by the electron beam in the DE magnet bend is given by the equation

$$P[kW] = 14 \text{ " } [rad]\, I\, [A]\, E^4\, [GeV^4] /R[m].$$

Alpha is the bending angle of the DE magnet. The electron energy enters with the fourth power. Therefore, it is reasonable to minimize the electron energy by using the highest possible ion beam energy, such as those at RHIC, to achieve high e - A collision energies with modest electron energies. For the same emitted synchrotron power, and the same center-of-mass energy, lowering the momentum of the electron beam allows the use of much **higher electron beam currents**. This increases the luminosity.

If the model geometry of the present conceptual design is compared with DESY geometry the advantage of the model geometry is given by the following:

$$P_{eRHIC} = 28 \text{ kW} \times (0.76/0.28)^2 \times (10/30)^4\, I(eRHIC)/(HERA).$$

With the same synchrotron radiation power, the eRHIC interaction region could tolerate 10 times as much electron current as HERA, i.e., 600 mA. This makes the linac option with its superior beam characteristics and currents of a few 100 mA a very viable option.

managed for the U.S. Department of Energy
by Brookhaven Science Associates, a company
founded by Stony Brook University and Battelle